2006

Transmission Lines For Ir Signal Routing

Tasneem Mandviwala
University of Central Florida

TRANSMISSION LINES FOR IR SIGNAL ROUTING

by

TASNEEM MANDVIWALA
B.S. Sardar Patel University, Vallabh Vidhyanagar, India, 1999
M.S. University of Central Florida, 2002

A dissertation submitted in partial fulfillment of the requirements
for the degree of Doctor of Philosophy
in the School of Electrical Engineering and Computer Science
in the College of Engineering and Computer Science
at the University of Central Florida
Orlando, Florida

Summer Term
2006

Major Professors: Glenn D Boreman and Brian A Lail

ABSTRACT

In this dissertation, the design, fabrication, and characterization of coplanar striplines, vias, and microstrip lines is investigated, from the point of view of developing interconnections for antenna-coupled infrared detectors operating in the 8- to 12-micron wavelength range. To our knowledge, no previous efforts have been made to study the performance of metallic-wire transmission lines at infrared frequencies. Both the design and fabrication of these structures present unique challenges. Because of attenuation and dispersion issues, the analytical formulas for transmission-line parameters that are valid below a few hundred GHz are not applicable in the infrared. Therefore, numerical modeling was performed to characterize the coplanar striplines and microstrip structures in terms of transmission-line parameters: characteristic impedance, attenuation constant and effective index of refraction. These parameters were extracted by fitting the computed impedance as a function of transmission-line length to the usual impedance transformation equation. The material properties used in the model are realistic, having been measured at the frequencies of interest by infrared ellipsometric techniques. The transmission-line parameters cannot be measured directly in the infrared, so experimental validation was carried out by measuring the response of a bolometer, which was connected to a dipole antenna by different lengths of both the coplanar and microstrip transmission lines. The modeled and measured responses for both types of transmission lines was in good agreement. A third type of signal-routing structure was also investigated, that of the vertical via, essentially a low-frequency connection that facilitates location of the bondpads away from the plane of the antenna. In the configuration studied, the vias pass vertically down through the SiO_2 isolation layer and a

groundplane, which provides electromagnetic isolation between the antenna and the structures that allow for signal-extraction from the bolometer. This type of interconnection will be useful for future detailed studies relating the angular antenna pattern to the spatial response of the antenna-coupled sensor.

To my mother, Sarrah

ACKNOWLEDGMENTS

I would like to thank my PhD advisor Dr. Glenn Boreman for his mentorship throughout the course of this thesis. I have yet to see the limits of his wisdom, his patience, and his selfless concern for his students.

I acknowledge Dr. Brian Lail for the valuable discussions and helpful insight to my research. I would also like to thank Dr. Donald Malocha, Dr. Eric Johnson and Dr. S. T. Wu for serving as my advisory committee.

All the members of Infrared Systems Laboratory have been very helpful and I thank them for their support. I am grateful for the relationships that I have built with them. I thank Dr. Ivan Divliansky for his technical assistance with e-beam lithography.

I acknowledge my family members for their encouragement and support. I would like to thank my parents, in particular, for teaching me the value of hard work and perseverance. I thank my husband Ammar and my daughter Batul for their support, patience and love.

This research is supported by Northrop Grumman Apopka, FL.

TABLE OF CONTENTS

LIST OF FIGURES x

LIST OF TABLES xiv

LIST OF ACRONYMS/ABBREVIATIONS xv

CHAPTER 1 INTRODUCTION 1

CHAPTER 2 BACKGROUND 5

2.1 Antenna-Coupled Infrared Detectors 5

2.2 Bolometers 7

2.3 Transmission line interconnections under study 9

2.3.1. Coplanar transmission lines 10

2.3.2 Microstrip lines 17

2.3.3 Via interconnect 20

2.4 Numerical Modeling 22

2.5 Lithographic Fabrication 24

2.5.1 Thin film deposition and characterization 24

2.5.1.1 Evaporation and Sputtering 24

2.5.1.2 Plasma enhanced chemical vapor deposition (PECVD) and reactive ion etching (RIE) 26

2.5.1.3 Infrared variable angle spectroscopic ellipsometry 27

2.5.2 Electron beam lithography 30

CHAPTER 3 COPLANAR STRIPLINES 34

3.1 Numerical characterization of CPS 34

3.1.1 Validation of computational approach at 10 GHz 37
3.1.2 Parameter extraction at IR 38
3.1.4 Response calculation 44
3.2 Fabrication of antenna connected to CPS 46
3.3 Experimental method and results 48
CHAPTER 4 MICROSTRIP LINES 55
4.1 Numerical characterization of MS 55
4.1.1 Validation of computational approach at 10 GHz 56
4.1.1.2 MS transmission-line parameters on different substrates 57
4.1.2. Response calculation 61
4.2 Fabrication and response measurements 62
4.2.1 Fabrication of MS on PECVD deposited SiO_2 standoff 63
4.2.2 Experimental results for MS on PECVD SiO_2 standoff layer 66
4.2.3 Fabrication of MS on ZrO_2 standoff layer 71
4.2.4 Fabrication of MS on BCB standoff layer 73
4.2.5 Response measurement of MS on BCB standoff layer 75
CHAPTER 5 VIA INTERCONNECTION 77
5.1 Effect of bondpads on antenna response 78
5.2 Modeling for via optimization 81
5.2.1 Cut-out size in the ground plane 82
5.2.2 Characterization of vias at infrared frequencies 84
5.4 Fabrication 87
CHAPTER 6 CONCLUSION 95

APPENDIX: 2D MAPS – RESPONSE DUE TO BONDPADS AND LEAD LINES 97

LIST OF REFERENCES 102

LIST OF FIGURES

Figure 1.1 Array of log-periodic antennas [1] 2

Figure 1.2 Illustration of application of transmission-lines at IR frequencies..... 3

Figure 2.1 Cross sectional view of coplanar stripline..... 10

Figure 2.2 Cross sectional view of coplanar waveguide..... 10

Figure 2.3 Measured and computed attenuation as a function of frequency [15]..... 14

Figure 2.4 Frequency-dependent attenuation from [22] 15

Figure 2.5 Phase velocity of CPS on different substrates [23] 16

Figure 2.6. Layout of (a) coaxial line, (b) stripline and (c) microstrip line 17

Figure 2.7. Frequency dependent refractive index [37] 19

Figure 2.8. Frequency dependent effective dielectric constant for varying *h* [36] 20

Figure 2.9 Ellipsometric thin-film analysis configuration 28

Figure 3.1 HFSS model for CPS characterization 35

Figure 3.2 Analytical and computed impedance as a function of CPS length at 10 GHz 38

Figure 3.3. Computed Z_o and α for CPS design having fixed w = 600 nm for SiO_2 on Si substrate 39

Figure 3.4. Computed effective index for CPS design with fixed w = 600 nm and fixed s = 400 nm for SiO_2 on Si substrate 40

Figure 3.5. Computed Z_o and α for CPS design, on SiO2 on Si substrate, for fixed s = 400 nm 41

Figure 3.6 Computed Z_o and α for CPS design, on high resistivity Si substrate, for fixed w = 200 nm 42

Figure 3.7 Computed effective index for CPS design on high resistivity Si with fixed w = 200 nm and s = 200 nm 43

Figure 3.8 Computed Z_o and α for CPS design, on high resistivity Si, having fixed s = 200 nm 44

Figure 3.9 HFSS model for response calculation 45

Figure 3.10 Normalized port current squared (response), computed as a function of CPS length 46

Figure 3.11 Fabricated CPS connected dipole 47

Figure 3.12 Test setup for response measurement 49

Figure 3.13 Device response measured using F/8 optics 50

Figure 3.14 Convolution between laser beam and detector response for (a) L= 0 μm (no CPS) (b) L = 1.5 μm 52

Figure 3.15 Deconvolution of 2D map and laser beam for CPS L = 3 μm 53

Figure .3.16 Comparison of modeled and measured response at F/1 54

Figure 4.1 HFSS model for MS characterization 56

Figure 4.2 Analytical and computed impedance as a function of MS length at 10 GHz .. 57

Figure 4.3 Computed characteristic impedance of MS as a function of w and h 59

Figure 4.4. Computed attenuation constant of MS as a function of w and h 60

Figure 4.5. Computed effective index of refraction of MS as a function of w and h 61

Figure 4.6 Model for response calculation 62

Figure 4.7 Normalized current-squared response, computed for w = 0.4 μm 62

Figure 4.8 Top view of the device to be fabricated 64

Figure 4.9 Fabricated dipole antenna connected to MS 66

Figure 4.10 Measured versus modeled response at F/8 68

Figure 4.11 2D map for L = 6 μm..... 69

Figure 4.12 Measured versus modeled response at F/1 70

Figure 4.13 Response map for the dipole antenna (MS *L* = 0 μm)..... 75

Figure 4.14 Normalized computed versus measured response..... 76

Figure 5.1 Device configuration (cross-sectional view)..... 78

Figure 5.2 Antenna designs used to study the effects of bondpads: (a) dipole antenna on grounded SiO_2, (b) dipole antenna from [16] 79

Figure 5.4 Computed normalized response for the three cases 81

Figure 5.5 Cross-sectional view of model to study the effect of size of cut-out in ground plane..... 82

Figure 5.6 Top view of model for optimizing cut-out size..... 83

Figure 5.7 Computed power dissipated as a function of size of the cut-out in ground plane 84

Figure 5.8 Cross-sectional view of model for optimizing bolometer location 85

Figure 5.9 Computed power dissipated in bolometer as a function of bolometer location *D* μm 86

Figure 5.10 Cross-sectional view of device with vias through one isolation layer 87

Figure 5.11 Fabricated dipole antenna with via through one isolation layer (top view) .. 90

Figure 5.12 Fabricated ground plane and cutout aligned to vias (1^{st} layer)..... 91

Figure.5.13 Fabricated 2^{nd} layer vias aligned to cutout and ground plane 92

Figure 5.14 Details of fabrication process..... 92

Figure 5.15 FIB cross-section of the device 93

Figure 5.16 Measured 2D map of fabricated device..... 94

LIST OF TABLES

Table 2.1 Optical Constants measured from IR-VASE 30

Table 4.1 standoff layer height variation for T-line parameter extraction..... 58

Table 4.2 BCB thickness for 3000 rpm spin speed..... 73

LIST OF ACRONYMS/ABBREVIATIONS

BCB	benzocyclobutene
CPS	coplanar stripline
DC	direct current
DXRL	deep X-ray lithography
FEM	finite element method
FFT	fast Fourier transform
FPA	focal plane array
HFSS	high frequency structure simulator
Hi-NP	high-aspect-ratio nanoprint
LIGA	lithographie, galvanoformung and abformung
LSE	longitudinal-section electric
LWIR	long wave infrared
MEMS	micro-electro-mechanical systems
MIBK	methyl-isobutyl-ketone
MMIC	monolithic microwave integrated circuit
MOM	metal-oxide-metal
MS	microstrip
IPA	isopropanol
IR	infrared
IR-VASE	infrared variable angle spectroscopic ellipsometry
PECVD	plasma enhanced chemical vapor deposition
PMGI	polymethyl glutarimide
PMMA	polymethyl methacrylate
RF	radio frequency
RIE	reactive ion etch
RPM	revolutions per minute
SCCM	standard cubic centimeters
SEM	scanning electron microscope
TCR	temperature co-efficient of resistance
TE	transverse electric
TEM	transverse electro-magnetic
TM	transverse magnetic
TMAH	tetramethyl ammonium hydroxide
TWMV	through-wafer micro-vias
UV	ultraviolet
YBCO	yttrium barium copper oxide

CHAPTER 1 INTRODUCTION

Infrared antennas are used to collect incident power and apply it as an alternating signal at THz frequencies to a detector with dimensions much smaller than the wavelength. The separation of the power collection and sensing functions of the detector permits optimization of both functions independently. This concept leads to numerous possible combinations of shapes and materials for both the sensor and antenna. Many planar-antenna designs are feasible and can be tailored according to the application: dipole, bow-tie, spiral, log-periodic, slot antenna and microstrip patches. The types of sensors include microbolometers, metal-oxide-metal (MOM) diodes, Schottky diodes, etc. The design of infrared detectors requires taking into account effects that can be neglected at microwave frequencies. Resonance features are altered because the propagation of THz frequency antenna current-waves is affected by the large high-frequency complex surface impedance of the material.

In this dissertation, we demonstrate the first LWIR transmission-line design and fabrication in conjunction with infrared detectors. No previous efforts have been made to study the performance of any metallic-wire transmission lines in this frequency range. We have characterized two different types of transmission lines, namely, coplanar striplines (CPS) and microstrip (MS) lines, at IR frequencies in terms of characteristic impedance, attenuation constant and phase constant. We also studied vertical vias as another type of interconnect for IR antennas.

Among wide applications of transmission lines, one is the fabrication of a phased-array antenna. Advantages of a phased array antenna are that the angular pattern narrows as the array gets larger, and the antenna beam can be steered electronically by controlling

the relative phase between elements. Infrared focal plane array (IR FPA) pixels have been fabricated (Figure 1.1) wherein each antenna is connected to a single bolometric detector, and the detectors are connected in series by low frequency connections. Hence, the signals from individual bolometers add up incoherently, and the phase information across the array is not preserved because the current waves on each antenna are dissipated before any summation takes place. Thus, these IR antennas would not work as a phased array. In order to achieve phase coherence it is desired to use waveguides suitable for the IR-frequency current waves in order to interconnect the antennas, such that each antenna's current combines with preservation of phase information. The resulting aggregate current would then be sensed by a single bolometer. Figure 1.2 shows two IR dipole antennas connected through a CPS interconnection to a single bolometric sensor.

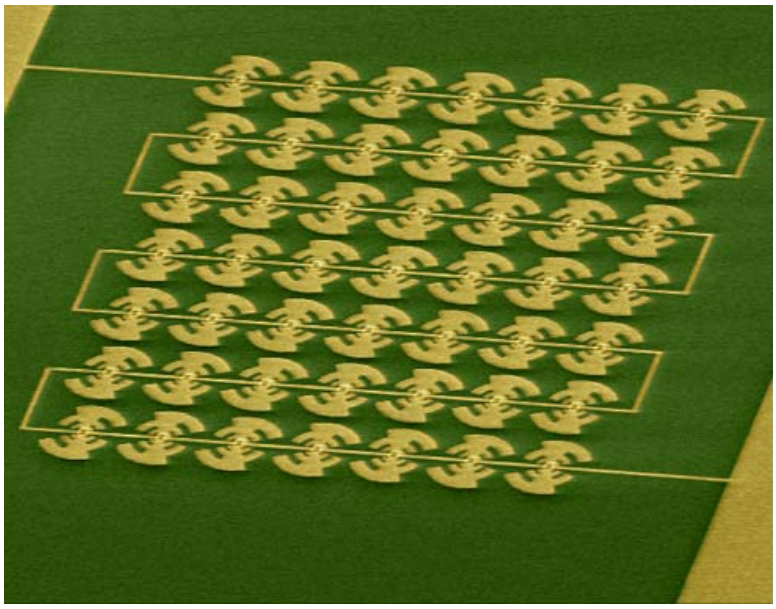

Figure 1.1 Array of log-periodic antennas [1]

Since the infrared range of frequencies exceeds the range of validity of the quasi-static approximations, transmission-line parameters such as characteristic impedance, phase constant and attenuation constant cannot be calculated directly from the standard analytical formulas, which are only valid at microwave and millimeter-wave frequencies. Numerical modeling is required to extract these transmission-line parameters and to study the propagation of electrical signals along the transmission lines in the THz range of frequencies.

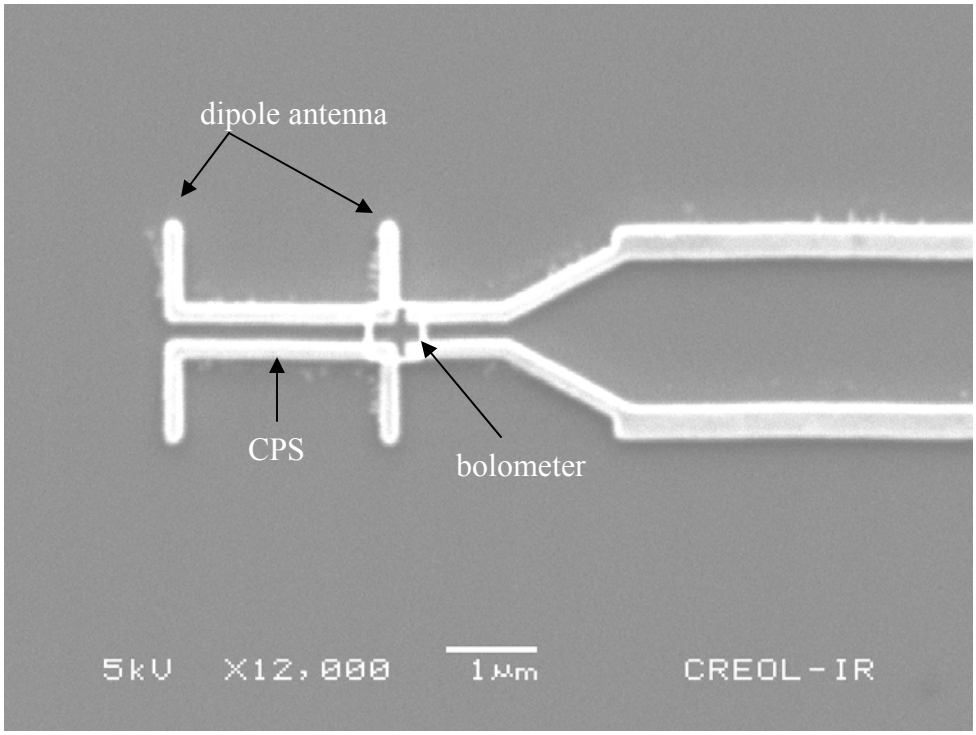

Figure 1.2 Illustration of application of transmission-lines at IR frequencies

Each of the three transmission lines considered have their own significance. *CPS* is the baseline design of interconnections for planar focal plane arrays that have been fabricated in the IR Systems laboratory. The *Vias* on the other hand help to avoid long dc (direct current) lead lines and electrically large bondpads on antenna plane and hence reduce the electromagnetic impact on antenna. In this configuration, the vias runs

vertically down through the substrate connecting the antenna to the bondpads. Vias also provide access to feed-point geometries in designs such as spirals where the design geometry prohibits coplanar interconnects. We take advantage of electrically isolating the bondpads by inserting a ground plane between antenna and bondpads. In addition, the presence of ground plane in case of vias provides us an opportunity to use *microstrip lines* which serve to better contain the propagating fields between the trace and ground plane.

CHAPTER 2 BACKGROUND

2.1 Antenna-Coupled Infrared Detectors

The sensors that are used to detect optical radiation are typically either photodetectors or thermal detectors. Photon detectors are devices or materials that detect light by a direct interaction of the radiation with the free electrons or holes of the material. This interaction of light and matter produces parameter changes that are detected by associated circuitry. Physical parameters that can change in a photon detector because of optical radiation are resistance, inductance, voltage and current. On the other hand, thermal detectors respond to the heating effects of the absorbed energy of the optical radiation by changing the temperature of the sensor. This process requires two steps: the radiation must change the temperature of the detector, and then this temperature change causes some measurable parameter change. The physical parameter change is then detected by associated instrumentation. Because thermal detection processes require the absorbed radiation to change the temperature of the detector element, the time response is slower than in the corresponding photodetectors, for which the absorption of photon to generate a hole-electron pair occurs virtually instantaneously [2].

A variety of infrared spectroscopic and imaging applications require fast sensors. Since the detector response time is proportional to its volume it seems reasonable to reduce the detector volume until the desired time constant is attained. However, as the sensor gets smaller it loses its ability to collect radiation, adversely affecting its responsivity. One way of maintaining a reasonable responsivity, while obtaining a fast response is to integrate the sensor with an antenna. This antenna-coupled detector

architecture separates the function of collecting radiation from the detection function. The antenna collects the radiation and supplies an electrical signal at its terminals. This electric signal is fed into, and processed by, the sensor. The sensor must be impedance matched to the antenna to ensure efficient energy transfer.

The first successful antenna-coupled IR detector was reported in 1968 by Hocker *et al.* [3]. It consisted of a thin, long tungsten wire in contact with a metallic (silver or steel) base plate. By pressing the sharp tip against the metal plate, a non-linear diode contact was created. The tungsten wire acted like a long wire antenna for 10.6-μm laser radiation. The non-linear contact rectified the electrical currents induced along the wire. From a practical point of view, these structures had several drawbacks: 1) the thin, long, unsupported wires were mechanically unstable and reproducible results were very difficult to achieve, 2) the cylindrically symmetric radiation pattern of the long wire did not allow for good antenna directivity, 3) it was impossible to arrange these "cat whiskers" in an array to form a large-area detector.

Significant detector improvements were achieved by using lithographic fabrication techniques. It also opened the possibility of large-area detectors based on arrays. These lithographic IR sensors used MOM diodes as detectors. MOM diodes integrated with wire-like printed antennas were reported during mid-1970s [4], [5], [6]. The detection mechanism was based on rectification of induced antenna currents by the MOM diodes.

Until the early 1990s lithographic antennas found applications mainly in the microwave and millimeter-wave spectral domains. In 1991 Grossman *et al.* [7] reported on an integrated detector operating at 9.5-μm wavelength. The detector consisted of a

niobium microbolometer integrated with a printed gold spiral antenna. In the following years, integrated infrared detectors using lithographic dipole [8], log-periodic [9], bow-tie [10] and spiral [11] antennas were reported.

With the advent of advanced electron-beam lithography techniques, significant progress has been achieved in improving the device performance of antenna-coupled detectors. Infrared focal-plane arrays have been fabricated to improve responsivity for commercial infrared imaging applications [12], [13]. A shared-aperture imaging system employing a common focal-plane array (FPA) that responds to both IR and millimeter-wave radiation has been demonstrated [14].

In this dissertation, we investigate the feasibility of coplanar striplines, vias and microstrip line interconnections in conjunction with the IR detectors. The dipole antenna, being the simplest of all antenna types, is used in this study so we can better understand the performance of different transmission lines that we connect to the antenna. Incident IR radiation is received by the dipole, propagated along the length of the transmission line, and sensed by a microbolometer.

2.2 Bolometers

Bolometers operate on the principle that temperature change produced by the absorbed radiation produces a change in resistance of the material. The temperature coefficient of a bolometer depends on its material and the amount of change in resistance produced by a corresponding temperature change. Bolometer material should have high temperature coefficient of resistance (TCR) so that their resistance change with temperature is high. The linear equation relating resistance and temperature change is

$$R = R_0(1 + \alpha \Delta T_d) \qquad \textbf{2.1}$$

$$\alpha = \frac{1}{R_0}\frac{dR}{dT} \qquad \textbf{2.2}$$

where α is the TCR, R_0 is the resistance at the base temperature and ΔT_d is the change in detector temperature. The three types of bolometers are metal, semiconductor, and superconductor. Metal bolometers have a linear dependence on temperature. Typically the temperature coefficient of resistance (α) is 0.5%/^{o}C. The temperature coefficient of a semiconductor is negative, and has an exponential dependence on temperature. Because of this exponential dependence, the relative resistance change is larger, approximately 3%/^{o}C for semiconductors. The superconducting bolometer operates on transition edge of being a superconductor, that is, having no resistance. IR detectors have been produced using all three types of bolometer materials; including vanadium oxide, semiconducting yttrium barium copper oxide (YBCO) and nickel.

The responsivity of the bolometer is given by

$$\Re_\upsilon = \frac{i_{bias} R \alpha \eta}{G[1+\omega^2 \tau_{th}^2]^{1/2}} \qquad \textbf{2.3}$$

i_{bias} is the bias current, R = bolometer resistance, α is the TCR, η is the optical absorption coefficient, G is the thermal conductance, ω is modulation frequency, τ_{th} is the thermal time constant = C/G and C is the heat capacity.

Equation (2.2) shows that, if the thermal conductance increases (more heat flow through the wires), the responsivity decreases, the time constant decreases and frequency response is higher. Conversely, if the thermal conductance decreases, the responsivity increases, the time constant increases, and frequency response is lower. One cannot achieve both high responsivity and fast response in a bolometer. Also, high resistance and high temperature coefficient of resistance are desired for a bolometric material.

The bolometric materials used in this dissertation are nickel and gold, with TCR 0.6%/^{o}C and 0.4%/^{o}C, respectively. Nickel bolometers are used in the study of coplanar stripline transmission lines while gold bolometers are used in conjunction with vias and microstrip lines.

2.3 Transmission line interconnections under study

The usual analytical formulas for computing transmission-line parameters: characteristic impedance (Z_o), attenuation constant (α) and effective index of refraction (n_{eff}) are only valid for frequencies below few hundred GHz [15]. These analytical formulas are based on the quasi-static approximation which considers a pure TEM mode of signal propagation. The quasi-static assumption can be safely applied for frequencies below X-band; above this frequency range the errors thus encountered are non-negligible. Other than that, the design of transmission lines at IR frequencies requires taking into account effects that can be neglected at RF and microwave frequencies. For example, metals and dielectrics have different material properties at IR compared to RF; at IR they tend to be lossier and the propagation of THz-frequency current-waves is affected by the large complex permittivity of the metal [16], [17]. The signal distortion is high and the attenuation is expected to be dominated by radiative losses at these frequencies [18], [19]. Thus, the transmission lines at IR have unique attenuation and dispersion issues. Therefore, we study the performance and extend the design characterization of CPS and MS to IR.

Apart from the application of transmission lines in the development of phased array antennas, the measurements of the transmission-line propagation properties can be

applied to more fundamental studies such as the extraction of material parameters for high temperature superconducting films in sub terahertz frequency regions [20].

2.3.1. Coplanar transmission lines

In a CPS, the electric-field lines from the strip conductors of width w extend across the slot of width s. The CPS is supported on a thin dielectric substrate of relative permittivity ε_r and thickness d, as shown in Figure. 2.1. Figure 2.2 shows the configuration of coplanar waveguide, which is the dual of coplanar stripline.

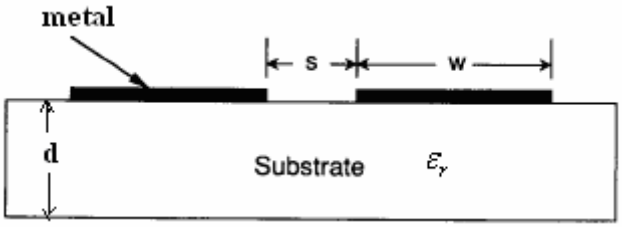

Figure 2.1 Cross sectional view of coplanar stripline

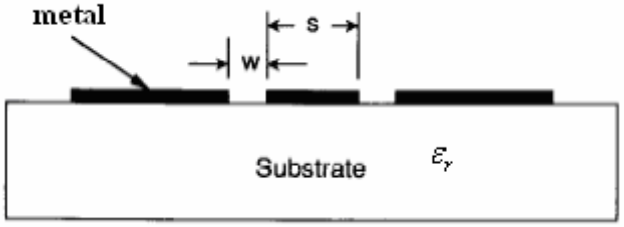

Figure 2.2 Cross sectional view of coplanar waveguide

The propagation factor of a transmission line, in general, is given by

$$\gamma(f) = \alpha(f) + j\beta(f) \qquad \textbf{2.4}$$

where α and β are attenuation constant and phase constant, respectively. The former mainly arises from the radiation, conductor, and dielectric losses, where the dielectric loss dominates if the substrate is highly conductive. The latter term, which determines the

degree of dispersion a signal waveform experiences, is affected primarily by the geometry of the transmission line, its dimensions and the substrate permittivity. The phase constant β is given by

$$\beta(f) = 2\pi \frac{f}{c} \sqrt{\varepsilon_{eff}(f)} \qquad \textbf{2.5}$$

The effective permittivity ε_{eff} is defined in this context as the permittivity of a uniform dielectric material such that a transmission line is immersed in that dielectric would have identical electrical characteristics, particularly propagation constant, as the actual transmission-line of Figures 2.1 and 2.2.

Experiments have been conducted in past to study the attenuation and dispersion characteristics of high frequency coplanar transmission lines. Hasnain et al. [21] proposed an analytical formula, fitted to full-wave analysis results, to model the dispersion characteristics of coplanar transmission lines valid at frequencies below 1 THz. They analytically approximated ε_{eff} from a numerical simulation as,

$$\sqrt{\varepsilon_{eff}(f)} = \sqrt{\varepsilon_q} + \frac{(\sqrt{\varepsilon_r} - \sqrt{\varepsilon_q})}{\left(1 + a\left(\frac{f}{f_{te}}\right)^b\right)} \qquad \textbf{2.6}$$

Equation (2.6) is semi-empirical and makes no quasi-static assumptions. The parameter ε_q is the quasi-static effective permittivity,

$$\varepsilon_q = \frac{\varepsilon_r + 1}{2} \qquad \textbf{2.7}$$

f_{te} is the surface wave TE_1 mode (lowest-order mode) cut-off frequency,

$$f_{te} = \frac{c}{4d\sqrt{\varepsilon_r - 1}} \qquad \textbf{2.8}$$

b (~ 1.8) is an empirical constant independent of geometry, and c is speed of light in vacuum. The parameter a is related to transmission line geometry as

$$\log(a) \sim u \log(s/w) + v \quad \textbf{2.9}$$

$$u \sim 0.54 - 0.64q + 0.015q^2 \quad \textbf{2.10}$$

$$v \sim 0.43 - 0.86q + 0.54q^2 \quad \textbf{2.11}$$

$$q = \log(s/d) \quad \textbf{2.12}$$

The characteristic impedance can then be obtained using effective permittivity from eq. (2.5) and is expressed as

$$Z_{CPS} = \frac{120\pi}{\sqrt{\varepsilon_{eff}}} \frac{K(k)}{K'(k)} \quad \textbf{2.13}$$

$$Z_{CPW} = \frac{120\pi}{\sqrt{\varepsilon_{eff}}} \frac{K(k)}{4K'(k)} \quad \textbf{2.14}$$

where $k = s/(s+2w)$, $K(k)$ is complete elliptical integral of the first kind, and $K'(k) = K(\sqrt{1-k^2})$.

In addition to dispersion characteristics, the attenuation becomes important at high frequencies. Grischkowsky *et al.* [18] have experimentally demonstrated that the radiative losses are dominant at frequencies over ~ 200 GHz for coplanar transmission line dimensions of the order of few tens of microns. Rutledge *et al.* [19] have derived analytical formulas to model radiative attenuation of coplanar transmission lines in frequency domain under quasi-static approximations, predicting cubic frequency dependence. For example, for a coplanar waveguide, the radiative attenuation is given as

$$\alpha_{CPW} = \left(\frac{\pi}{2}\right)^5 \frac{1}{\sqrt{2}} \frac{(1-1/\varepsilon_r)^2}{\sqrt{1+1/\varepsilon_r}} \frac{(s+2w)^2 \varepsilon_r^{3/2}}{c^3 K'(k) K(k)} f^3 \quad \textbf{2.15}$$

The experimental data from Frankel *et al.* [15] indicate that this formula is not valid up to THz frequencies. Figure 2.3 shows the measured attenuation and equation (2.15) on log-log scale, where the slope of measured attenuation is significantly below 3, the behavior predicted by equation (2.15). This discrepancy is due to inaccuracies introduced by the quasi-static approximation at high frequencies.

Frankel *et al.* [15] made modifications to radiative attenuation of equation (2.15) which resulted in excellent agreement between the functional frequency dependence of the measured and computed attenuation up to high GHz frequencies (< 1 THz), for low-loss substrates, as

$$\alpha_{CPW} = \left(\frac{\pi}{2}\right)^5 2 \frac{\left(1-\frac{\varepsilon_{eff}(f)}{\varepsilon_r}\right)^2}{\sqrt{\frac{\varepsilon_{eff}(f)}{\varepsilon_r}}} \frac{(s+2w)^2 \varepsilon_r^{3/2}}{c^3 K'(k) K(k)} f^3 \qquad \textbf{2.16}$$

$$\alpha_{CPS} = \pi^5 \left(\frac{3-\sqrt{8}}{2}\right) \sqrt{\frac{\varepsilon_{eff}(f)}{\varepsilon_r}} \left(1-\frac{\varepsilon_{eff}(f)}{\varepsilon_r}\right)^2 \frac{(s+2w)^2 \varepsilon_r^{3/2}}{c^3 K'(k) K(k)} f^3 \qquad \textbf{2.17}$$

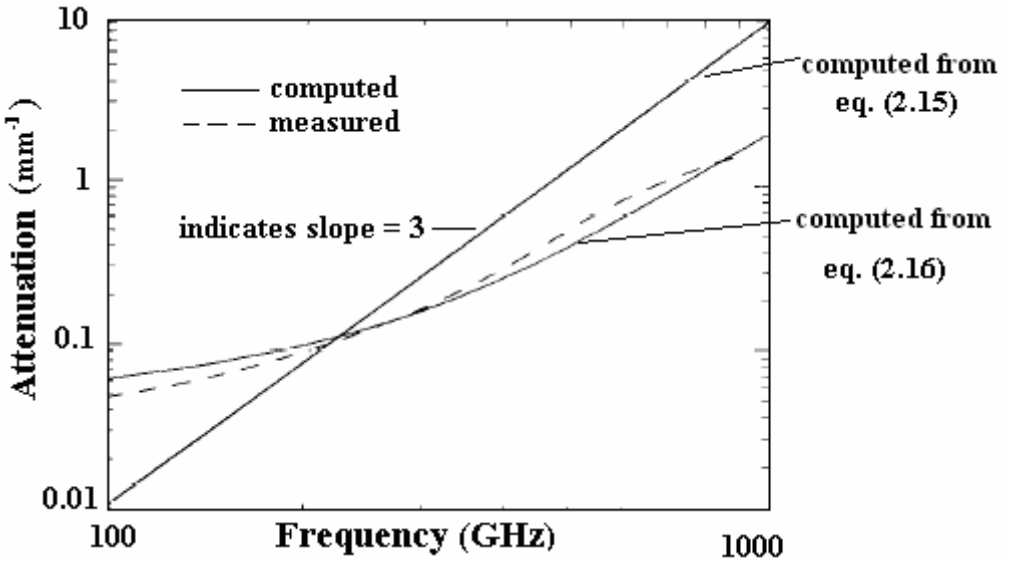

Figure 2.3 Measured and computed attenuation as a function of frequency [15]

Equation (2.16) has frequency-dependent effective permittivity term due to which it shows a quadratic dependence on frequency, as presented in Figure 2.3. This equation is only valid when, $\lambda >> (s + 2w)$, otherwise radiation loss will decrease with increasing frequency in a non-physical fashion.

Son *et al.* [22] studied the propagation of high-frequency signals on coplanar striplines with lossy semiconductor substrates and found very strong attenuation and dispersion due to the substrate. They also studied CPS on modulation doped layer consisting of AlGaAs/GaAs multiple-quantum-wells (MQWs). For this case, they found that the attenuation had a linear frequency dependence up to 1 THz, in contrast to cubic dependence under quasi-static approximations [19] or quadratic dependence for CPS on low-loss substrate [15]. Figure 2.4 shows the measured attenuation and its linear fit [22].

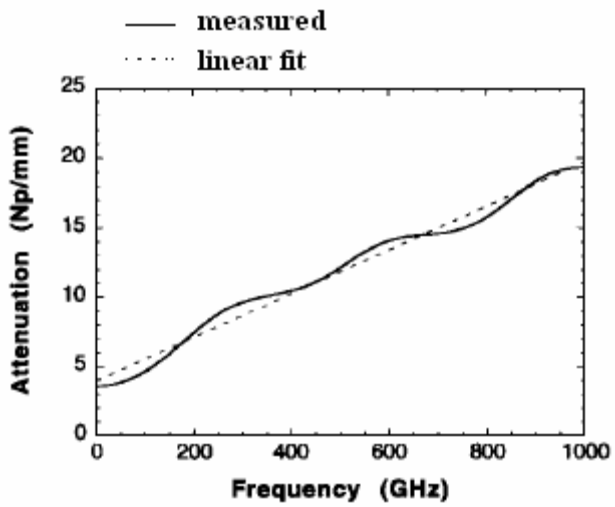

Figure 2.4 Frequency-dependent attenuation from [22]

The main reason for excessive high-frequency signal distortion found in planar transmission lines is the permittivity mismatch between substrate and air [18]. The dispersion occurs when the phase velocity of the propagating signal becomes slower than the speed of light. The dispersion effect is prominent at higher frequencies because the electric fields tend to concentrate more at higher frequencies and so the phase velocity is decreased [23], [24]. Cheng *et al*. [23] have investigated coplanar transmission lines fabricated on both low-permittivity composite dielectric membrane substrates and UV-grade fused silica ($\varepsilon_r = 3.6$). Virtually no radiation loss was observed for a CPS on a thin membrane in near 1 THz (where the attenuation would be expected to be proportional to f^n, where $1 < n < 3$ was observed by previous authors). Furthermore, the skin-effect loss for the membrane CPS at 1 THz is comparable to that of GaAs CPS at 150 GHz. The reason for such small skin-effect losses is the increase in impedance that occurs when the substrate permittivity is lowered. A higher impedance leads to a higher electric-to-magnetic field ratio, and thus more energy is stored in the electric rather than the magnetic field for a given energy density. Since the current flow in the metal is

proportional to magnetic field surrounding the transmission line, the smaller magnetic-to-electric field ratio means less current flow in the metal and thus lower skin-effect loss.

The dispersion, as well, was found to be much lower for CPS structures on thin membranes. The frequency-dependent phase velocity of CPS on a thin membrane and on fused silica from [23] are shown in Figure 2.5. For the CPS on a membrane, a phase velocity of approximately 90% of speed of light was found. For the CPS on a fused silica substrate, the dispersion is small for frequencies below 500 GHz. Above that, with the electric field tending to concentrate in the higher-permittivity substrate, the phase velocity decreased.

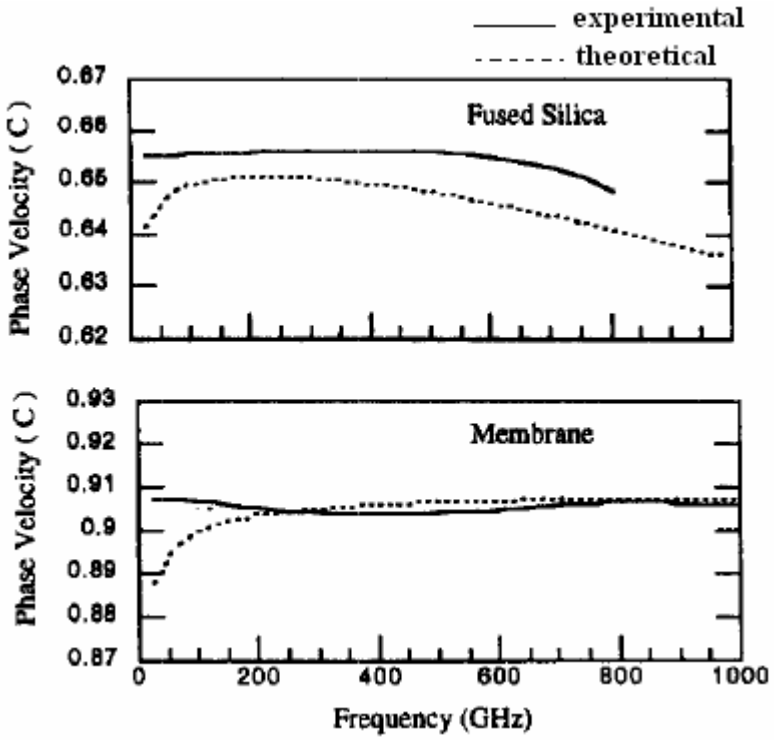

Figure 2.5 Phase velocity of CPS on different substrates [23]

In this work, we investigate the behavior of coplanar striplines at 28.3 THz.

2.3.2 Microstrip lines

Microstrip is a two-conductor transmission-line which can be considered to have evolved conceptually to a two-wire line. The layout of a typical microstrip line is shown in Figure 2.6, along with those of coaxial line and stripline. As an electrical signal travels along the line, it becomes distorted due to dispersion and attenuation characteristics of the line. While the electric and magnetic fields are confined to one material in waveguides, coaxial lines and striplines, the microstrip is open so that the fields are partially in the dielectric. The air-dielectric interface prevents propagation of pure TEM mode [25]. Therefore, the phase constant is not linear function of frequency, resulting in dispersion (non-TEM).

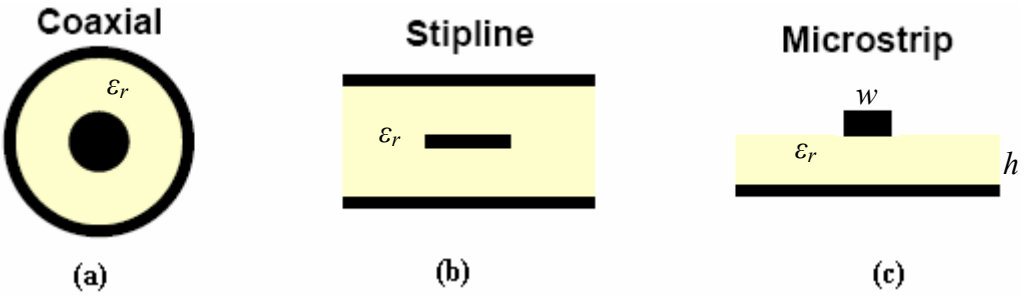

Figure 2.6. Layout of (a) coaxial line, (b) stripline and (c) microstrip line

The quasi-static methods of microstrip analysis do not take into account the non-TEM nature of microstrip mode. The non-TEM behavior causes the effective dielectric constant and impedance of microstrip to be functions of frequency. Of these two, the variation of the effective dielectric constant is more significant. An exact evaluation of these variations involves a full-wave analysis of the microstrip configuration [26]. However, there are several semi-empirical techniques available that lead to a closed form

solution for the dependence of effective dielectric constant and impedance on frequency. These dispersion models may be listed as below:

- Model based on coupling between TEM and TM_0 surface wave mode [27]
- An empirical relation for frequency dependent phase velocity [28]
- Longitudinal-section electric (LSE) mode using a dielectric-loaded ridged waveguide [29]
- Model based on coupling between a TEM and TE mode transmission lines [30]
- Planar waveguide model [31]
- Modification of Getsinger's formula [32]

In addition to semi-empirical techniques, more rigorous analysis of the dispersion characteristics of microstrip lines has been performed at microwave frequencies, such as, Integral Equation Method [33], [34] and Galerkin's Method [35]. Another analytical approach developed by Homentocovschi *et al.* [36] uses dual integral equations, in which a dispersion relation is obtained in terms of a double infinite system of linear equations with good convergence properties.

For computer analysis, a simple approximate formula to express the dispersion properties has been worked out by Yamashita *et al*. [37]. The dispersion effect shown in Figure 2.7 was calculated using fast Fourier Transform (FFT) from the study of picosecond pulse propagation [37], where $\varepsilon(0)$ and $\varepsilon(\infty)$ are the limiting values of effective dielectric constants at low and high frequencies, respectively.

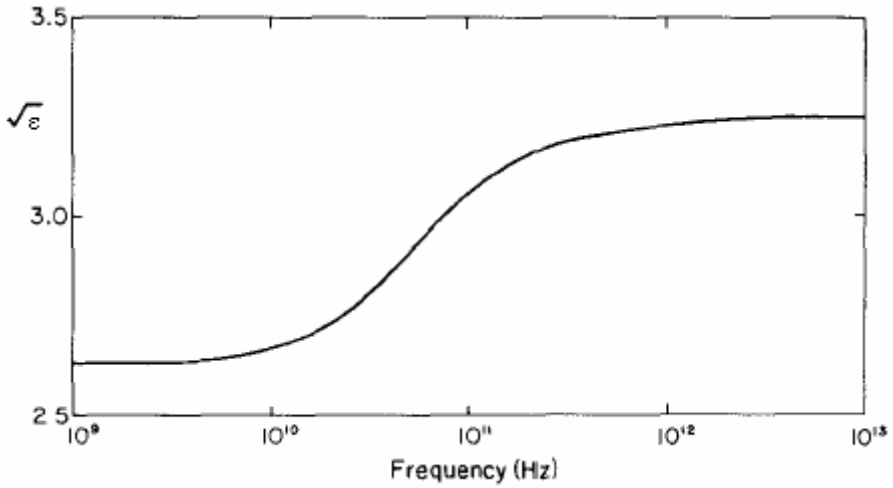

Figure 2.7. Frequency dependent refractive index [37]

During the past few years, extensive efforts have been made in zero-dispersion low-loss transmission lines for high frequencies. Roskos *et al.* [38] have shown that a microstrip line with buried silicide ground plane has significantly lower dispersion than conventional microstrips for electrical pulses of roughly 100 GHz bandwidth. Another technique reported by Heiliger *et al.* [39] consists of thin-film microstrip lines fabricated on low-resistivity Si with polymerized cyclotene as the dielectric between signal and ground conductor, which reveals negligible modal dispersion and low attenuation up to the highest frequencies of 1 THz. The onset of geometric dispersion can be shifted to higher frequencies by reducing the separation h of the signal conductor and the ground plane (Figure 2.8, [39]).

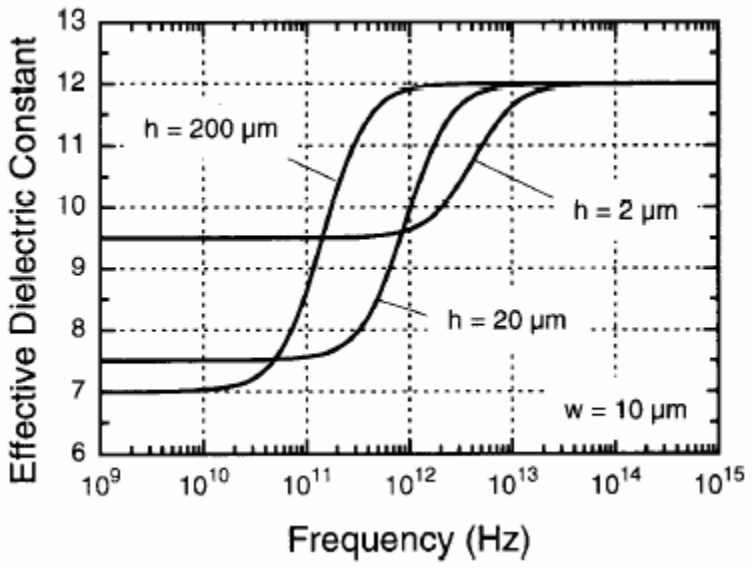

Figure 2.8. Frequency dependent effective dielectric constant for varying *h* [36]

The dispersion and attenuation characteristics of microstrip lines at high THz (infrared) range of frequencies are still not known and we study those in this work.

2.3.3 Via interconnect

In this work the main purpose of vias is to extract dc signal from the sensor element (e.g. bolometer). Hence the THz signals do not propagate through vias. In this section we focus on the fabrication techniques previously applied at microwave and optical frequencies for fabricating vias.

Fabrication of the multilevel structures in printed circuit boards and their interconnections began in early 1960s. The introduction of high resolution lithographic techniques started the electronic device integration age [40]. In the late 1960s the techniques of diode sputtering and ion milling were in very early stages of development. The conductor and device patterning necessary to achieve device integration was accomplished using lithographic techniques and chemical etching. In early 1960's,

metallization of vias in printed circuit boards was done by electroplating, and the initial metallization to start the electroplating process, particularly in through holes, was done using electroless copper. It was not until the late 1970's that the semi-additive and full-additive processes were introduced in printed circuit boards. These processes introduced their own version of through-mask-plating technology using electroless copper in mid 1970's. In early 1970s, through-mask-plating technology was used to fabricate Bubble Memory structures using optical lithography [41] and subsequently using e-beam and X-ray lithography [42]. In 1974 the first demonstration of deep etch patterns generated in PMMA using synchrotron radiation with 60:1 aspect ratio was produced [43]. In early 1980s, another technique called LIGA (Lithographie, Galvanoformung and Abformung) was developed and used particularly in building micro-electro-mechanical systems (MEMS) [44]. In 1990, Guckel *et al.* [45] have reported on the use of deep X-ray and UV lithographies in connection with electroplating for micromechanics.

With large aspect ratio structures, there are problems associated with their collapse. Goldfarb *et al.* [46] have developed drying process using supercritical carbon dioxide, organic solvents and surfactants to eliminate capillary forces naturally present during normal drying of photoresist material, and hence to prevent the collapse of high-aspect-ratio structures fabricated from aqueous-based photoresist.

Nanotechnology is now encouraging many researchers to derive innovative and superior properties from extremely small structures. There are several fields of study in nanotechnology, but the fabrication of these small structures, nanoscale patterning, is the key study among them. Photolithography is presently a powerful method for fabricating finely patterned structures with the resolution of few microns, while electron beam

lithography is capable of producing the finest patterns, nearly to the nanometer scale. However, to continue to reduce the patterning size, further investment is required, which is the conventional road map for nanoscale fabrication. Soft lithography is an attractive solution to overcome this problem [47]. There are several methods of soft lithography. Among them, nanoprinting, or nanoimprinting was first suggested several years ago [48] and is drawing attention as a low-cost nanoscale fabrication method. Kuwabara *et al.* [49] have fabricated high-aspect-ratio structures (nanopillars) with diameters of 80–1000 nm and heights of 1–3 μm using high-aspect-ratio nanoprint (Hi-NP) technology [50], [51]. The LIGA process is a micromachining method that applies deep X-ray lithography (DXRL), electroforming and micro molding techniques to fabricate microstructures of various materials, including polymers and metals. DXRL has been shown to provide microstructures with high aspect ratio and well-controlled dimension [52]. Finkbeiner *et al.* [53] developed ultra-low impedance through-wafer micro-vias (TWMV) as electrical interconnects for superconducting circuits.

The vias for this work are fabricated using e-beam lithography in the nano-cleanroom facility at CREOL.

2.4 Numerical Modeling

We have used Ansoft HFSS (High Frequency Structure Simulator) for characterizing the transmission lines and vias. HFSS is a high performance full wave electromagnetic (EM) field simulator. It integrates simulation, visualization and solid modeling in an environment where solutions to 3D EM problems are quickly and accurately obtained. Ansoft HFSS employs the Finite Element Method (FEM), adaptive meshing, and advanced graphics to give insight to EM problems.

The materials used in the model are realistic; they use actual material parameters measured at IR frequencies, obtained from Infrared variable-angle spectroscopic ellipsometry (IR-VASE). The ellipsometer measures the change in polarization of light reflected from a sample. This information allows determination of optical properties of the metals and dielectrics used in the study. The operating principle of IR-VASE is discussed in detail in section 2.5.1.3. The optical constants of different materials measured at 10.6 μm wavelength are shown in Table 2.1. Knowing *n* and *k*, permittivity and conductivity are calculated using

$$N = n + ik \tag{2.18}$$

$$\mathrm{Re}(\varepsilon_r) = n^2 - k^2 \tag{2.19}$$

$$\mathrm{Im}(\varepsilon_r) = 2nk \tag{2.20}$$

$$\sigma = \omega\varepsilon_0 \,\mathrm{Im}(\varepsilon_r) \tag{2.21}$$

$$\tan(\delta) = \frac{\mathrm{Im}(\varepsilon_r)}{\mathrm{Re}(\varepsilon_r)} \tag{2.22}$$

At terahertz frequencies, metals have complex permittivities which HFSS is capable of handling. The loss term is accounted for by either conductivity or loss tangent, so using either one of these suffices in the model. Other than that, permittivity of the material is required for material definition. The type of port used in our CPS model is called waveport, while a lumped port is used in the MS and via models. The outermost box in the model is assigned "radiation" boundary condition to simulate an open problem that allows waves to radiate infinitely far into space. HFSS absorbs the wave at the

radiation boundary, essentially expanding the boundary infinitely far away from the structure.

The load impedance used in the models for characterizing transmission lines was assigned from "Lumped RLC" boundary condition. Running a "parametric sweep" was the most convenient method for characterizing different designs of transmission-lines.

2.5 Lithographic Fabrication

2.5.1 Thin film deposition and characterization

The thin films of metal and dielectric were deposited using three different processes. Two of them used physical vapor deposition method and one used chemical vapor deposition process. The physical vapor deposition processes include evaporation and sputtering which were used to deposit metal films while SiO_2 dielectric film was deposited using plasma enhanced chemical vapor deposition (PECVD). We used reactive ion etching (RIE) for etching SiO_2 and benzocyclobutene (BCB, also called cyclotene) for the fabrication of microstrip lines.

2.5.1.1 Evaporation and Sputtering

In electron-beam (e-beam) evaporation systems, a high-intensity beam of electrons, with energy up to 15 keV, is focused on a source target containing the material to be evaporated. The energy from the electron beam melts a region of the target. Material evaporates from the source and covers the wafer with a thin layer. The source material sits in a water-cooled crucible, and its surface only comes in contact with electron beam during the evaporation process. Purity is controlled by the purity of original source material. The deposition rate is easily controlled by changing the current

and energy of the electron beam. The deposition rate is monitored by quartz crystal, which is covered by the evaporating material during the deposition. The resonant frequency of the crystal shifts in proportion to the thickness of the deposited film. By monitoring the resonant frequency of the crystal, the deposition rates may be measured with an accuracy of better than 0.1 nm/sec. Because of the large mean free paths of gas molecules at low pressure, evaporation techniques tend to be directional in nature, and shadowing of patterns and poor step coverage can occur during deposition. These effects can be minimized by rotating the substrate holder continuously during the film deposition.

Sputtering is another technique for depositing thin films in the fabrication process. Sputtering involves bombarding a target with energetic ions, typically Ar^+. Atoms at the surface of the target are knocked loose and transported to the substrate, where deposition occurs. Electrically conductive materials such as aluminum, tungsten, gold, titanium can use a dc power source, in which the target acts as a cathode in a diode system. Sputtering of dielectrics requires an RF power source to supply energy to argon atoms. Sputtering provides excellent coverage of sharp topologies.

Most of our devices were made out of e-beam evaporated gold (Au) films deposited using BOC Edward evaporation system. We used titanium or chromium adhesion layers to ensure adhesion of Au films on SiO_2 substrate. The bolometer for our devices for CPS study was magnetron sputtered nickel (Ni) which was deposited using the MRC 8667 sputtering system.

2.5.1.2 Plasma enhanced chemical vapor deposition (PECVD) and reactive ion etching (RIE)

Chemical vapor deposition (CVD) is a chemical process for depositing thin films of various materials by thermal decomposition or reaction of gaseous compounds. The desired material is deposited directly from the gas phase onto the surface of the substrate. A number of forms of CVD are in wide use one of which is plasma enhanced CVD (PECVD). In this process a plasma is utilized to enhance chemical reaction rates of the precursors. PECVD processing allows deposition at lower temperatures ($250^{o}C$ – $350^{o}C$), which is often critical in the manufacture of semiconductors. In a parallel plate system, the wafers lie on a grounded aluminum plate, which serves as the bottom electrode for establishing plasma. The top electrode is a second aluminum plate placed in close proximity to the wafer surface. An radio frequency (RF) signal is applied to the top plate to establish the plasma. Gases are introduced along the outside of the system, which flow radially across the wafers and are pumped out through an exhaust in the center. The types and amount of gas used are determined by the deposition process.

Another technology using plasma to etch material deposited on wafers is called Reactive ion etching (RIE). A typical (parallel plate) RIE system is similar to the PECVD system in terms of electrode configuration, gas inlet/outlet and the process of initiating a plasma through application of RF power. In one RF cycle, the electrons are accelerated up and down in the chamber, sometimes striking both the upper wall of the chamber and the wafer platter. At the same time, the much more massive ions move relatively little in response to the RF electric field. The electrons absorbed onto the wafer platter cause the platter to build up charge due to its dc isolation. This charge build up develops a large

negative voltage on the platter, typically around a few hundred volts. The plasma itself develops a slightly positive charge due to the higher concentration of positive ions compared to free electrons. Because of the large voltage difference, positive ions tend to drift toward the wafer platter where they collide with the samples to be etched. The ions react chemically with the materials on the surface of the samples, but can also physically etch some material due to their high kinetic energy.

Silicon dioxide film was used as a standoff layer for microstrip line and vertical via interconnectors and was deposited using Plasma Therm 790-series-PECVD system. This system is two-chamber unit for PECVD and reactive ion etching (RIE). The gases used in SiO_2 deposition process are silane (SiH_4) and nitrogen dioxide (NO_2) with the following process parameters giving the deposition rate of 50nm/min: 250^{o}C chamber temperature, 1050 mTorr chamber pressure, 400 standard cubic centimeters per minute (sccm) SiH_4, 827 sccm NO_2, and 25 W RF power. Later this film was etched for creating vias using the RIE chamber of the same system. The process parameters used for etching 200 nm thick, 300 nm × 300 nm SiO2 are: 75 mTorr pressure, 5 sccm O_2, 45 sccm CF_4, 175 W RF power, 280 V dc bias, giving an etch rate of 50nm/min. Benzocyclobutene (BCB, also called cyclotene) was used as a standoff layer for MS and was etched using RIE process also [54], [55]. The process parameters for BCB etching are: 50 mTorr chamber pressure, 10 sccm O_2, 5 sccm CF_4, 100W RF power and 280 V dc bias giving an etch rate of 150 nm/min.

2.5.1.3 Infrared variable angle spectroscopic ellipsometry

After depositing the thin films they need to be characterized in terms of thickness and optical constants. Ellipsometry is a powerful tool for the characterization of thin

films and multi-layer semiconductor structures. It measures the change in polarization of light when it reflects from a surface. Linearly polarized incident light, when reflected, becomes elliptically polarized, and the degree of ellipticity is determined by the optical properties of the surface. The configuration for ellipsometric thin-film analysis is shown in Figure 2.9.

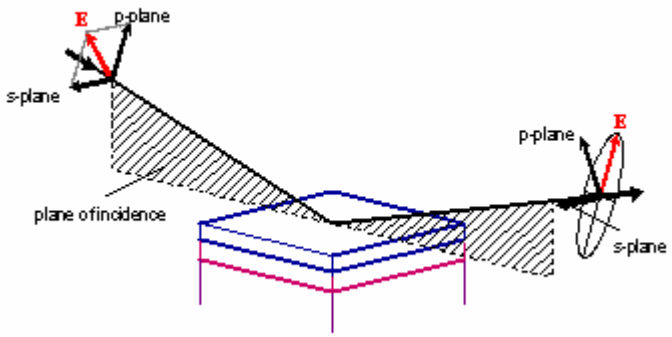

Figure 2.9 Ellipsometric thin-film analysis configuration

There are two special polarization directions for which the reflected light is plane polarized. Light polarized parallel (p-polarized light) and perpendicular (s-polarized light) to this plane remains plane polarized on reflection. The ellipsometer measures the ratio of the reflected p- and s-components and the phase difference between these two components. These two parameters are related to the fundamental physical properties of the reflecting surface such as the optical constants and the thickness of the material.

Since the ellipsometer measures the ratio of the reflected intensities of two mutually-perpendicularly polarized light beams, it does not need a reference beam. This makes ellipsometry highly accurate and reproducible. Ellipsometry can determine thin film thickness, optical constants for bulk and thin film materials, and often both thickness and optical constants of the film simultaneously. It can measure other parameters such as

surface roughness, degree of crystallinity, void fractions, anisotropy, interfacial mixing, uniformity and film composition. A model is constructed, based on the assumed values of these physical parameters. The actual value of these parameters are determined through the use of an iterative regression fitting computer algorithm which minimizes the error between the measured data and the model-generated data by adjusting the physical parameters of the model.

In this dissertation, we have analyzed all metal and dielectric thin films using the ellipsometer manufactured by J.A. Woollam Co. The unique property of this instrument is that it not only measures the optical constants of thin films but does so at a variable angle over the broad spectral range of 2 μm to 45 μm. The optical properties of thin films used in this dissertation and measured using IR-VASE are listed in Table 2.1.

The ellipsometric measurements of Table 2.1 show that the optical constants of a material vary slightly with film thickness. We find that *n* decreases with the increase in film thickness, while *k* increases with thickness indicating higher absorption for thicker films.

Table 2.1 Optical Constants measured from IR-VASE

Material	Thickness *h*	*n*	*k*
Au	150 nm	12.6	65.28
PECVD SiO_2	150 nm	2.3496	0.12307
	200 nm	2.0535	0.41285
	300 nm	2.2824	0.293
Thermal SiO_2	1.19 μm	2.035	0.0326
Low resistivity Si	380 μm	3.393	0.00866
High resistivity Si	380 μm	3.373	0.0032
BCB	200 nm	1.547	0.0054
	260 nm	1.542	0.0066
	330 nm	1.528	0.022
ZrO_2	60 nm	1.5795	0.02531
	80 nm	1.530	0.0334
	470 nm	1.4245	0.1058
Ni	200 nm	9.5	38.92

2.5.2 Electron beam lithography

We perform electron beam lithography to fabricate our devices. Electron beam lithography (EBL) refers to a lithographic process that uses a focused beam of electron to form patterns needed for material deposition on or removal from a wafer. An EBL system does not need masks to perform its task, rather, it simply draws the pattern over the resist wafer using the electron beam. Thus, EBL systems produce the resist pattern in a serial manner, making it slow compared to optical lithography processes.

A typical EBL system consists of the following parts: 1) an electron gun or electron source that supplies the electrons; 2) an electron column that shapes and focuses the electron beam; 3) a mechanical stage that positions the wafer under the electron beam; 4) a wafer handling system that automatically feeds wafers to the system and unloads them after processing; and 5) a computer system that controls the equipment.

We use the Leica EBPG 5000+ electron beam lithography tool. It uses a 25 MHz intelligent pattern generator. The high energy Gaussian beam gives nanometer scale resolution (25 nm) with vector scanning to create the pattern on the substrate.

Electron beam lithography uses e-beam-sensitive materials referred to as e-beam resists that are used to cover the wafer according to the defined pattern. They can be either positive or negative resists. Positive resists produce an image that is the same as the pattern drawn by the e-beam (positive image), while negative ones produce the reverse image of the pattern drawn (negative image). Positive resists undergo bond breaking when exposed to electron bombardment, while negative resists form bonds or cross-links between polymer chains in the same situation. As a result, areas of the positive resist that are exposed to electrons become more soluble in the developer solution, while the exposed areas of the negative resist become less soluble.

The resolution achievable with any resist is limited by two major factors: 1) the tendency of the resist to swell in the developer solution and 2) electron scattering within the resist. Resist swelling occurs as the developer penetrates the resist material. The resulting increase in volume can distort the pattern, to the point that some adjacent lines that are not supposed to touch become in contact with each other. Electron scattering occurs as the electron beam interacts with the resist and substrate atoms. This electron

scattering has two major effects: 1) it broadens the diameter of the incident electron beam as it penetrates the resist and substrate; and 2) it gives the resist unintended extra doses of electron exposure as back-scattered electrons from the substrate bounce back to the resist. Thus, scattering effects during e-beam lithography result in wider images than what can be ideally produced from the e-beam diameter, degrading the resolution of the EBL system. In fact, closely-spaced adjacent lines can add electron exposure to each other leading to a phenomenon known as proximity effect.

Types of resists used in this dissertation include polymethyl methacrylate (PMMA), copolymer methyl methacrylate / methacrylic acid (MMA (8.5) MAA), ZEP 520A and polymethyl glutarimide (PMGI) SF5 and SF7. PMMA positive resists are based on special grades of polymethyl methacrylate designed to provide high contrast, high resolution for e-beam, deep UV (220-250 nm) and X-ray lithographic processes. Copolymer resists are based on a mixture of PMMA and ~8.5% methacrylic acid. Copolymer MMA (8.5) MAA is commonly used in combination with PMMA in bi-layer lift-off resist processes where independent control of size and shape of each resist layer is required. The developer used for PMMA is methyl-isobutyl-ketone (MIBK). Because it removes some of unexposed resist, we use a 3:1 solution of isopropanol (IPA): MIBK.

The ZEP520A is positive, chain scission type electron beam resist for wet and dry etching with high resolution and excellent dry-etching resistance for device fabrication. It is ideally suited for the creation of photomasks and X-ray masks as well as ultra-fine processing. We used xylene (ZEP RD) as a developer for ZEP520A. PMGI is a positive tone resist derived from PMMA. It is ideally suited for multilayer applications such as lift-off processing and T-gate and air bridge fabrication. PMGI resists will not intermix

when used in combination with imaging resists, which eliminates the need for a plasma descum step. In addition the dissolution properties can be very carefully controlled, which makes them well suited for critical level lift-off processes where precise undercut control is required. The developer used for PMGI SF7 is tetramethyl ammonium hydroxide (TMAH). We use methylene chloride to remove ZEP and EBR-PG (which consists mainly of 1,3 dioxolane and propylene glycol monomethyl ether) to remove PMGI.

CHAPTER 3 COPLANAR STRIPLINES

Coplanar striplines (CPS) consists of two metal strips supported on a dielectric (Fig. 2.1). In a CPS, the electric-field lines from the strip conductors extend across the slot, meaning, the fields are in air and substrate. Hence the field confinement is not strong and thus they tend to have higher losses. Their planar structure makes them relatively simple to fabricate and so we have considered them as baseline design for our study of transmission lines. In order to study the characteristics and behavior of coplanar striplines at IR frequencies, we perform modeling, fabrication and testing of a dipole antenna resonant at 28.3 THz, connected to CPS of different lengths.

3.1 Numerical characterization of CPS

We have done the numerical characterization of CPS using Ansoft HFSS which is based on finite element analysis. Our procedure is based on parametric analysis of the transmission line as a function of its length. From full-wave field solutions, we compute the impedance at a defined port which is based on the reflected and transmitted fields at the port. This approach does not involve the use of analytical equations for computing transmission-line parameters, and hence, is a valid approach at LWIR. Our analysis is performed at 28.3 THz (10.6 μm), and yields results in terms of the transmission-line parameters of characteristic impedance (Z_o), attenuation constant (α) and effective index of refraction (n_{eff}).

We characterize these transmission lines using the procedure as follows: 1) extract transmission-line parameters: Z_o, α and n_{eff} through numerical modeling, 2) compute the response of the antenna connected to the sensor through the transmission

line as a function of transmission-line length, 3) fabricate the same antenna connected to transmission lines of several lengths and measure the sensor response as a function of transmission-line length, 4) compare the measured and modeled response. The response depends on the transformation of antenna impedance along the transmission-line length according to the transmission-line parameters (Z_o, α and n_{eff}) of the line. Hence verifying the measured response by comparison to the computed one indicates validation of extracted transmission-line parameters.

Figure 3.1 shows the HFSS model of a given CPS structure. We have modeled two different substrates for CPS: a 1.19-μm thick SiO_2 layer on top of 380-μm thick low resistivity Si wafer and 380-μm thick high resistivity Si wafer. Material parameters for Au, SiO_2 and Si were calculated from equations (2.18) – (2.22) using optical constants shown in Table 2.1 and were used in the HFSS models. The load resistor was formed using lumped a RLC boundary condition which can be used to represent a lumped resistor, an inductor or a capacitor, or a combination of these.

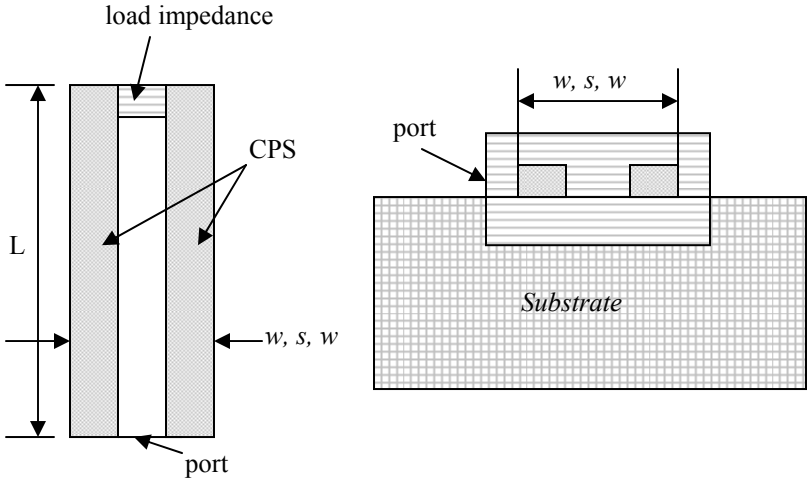

Figure 3.1 HFSS model for CPS characterization

In the model used for CPS characterization, one end of CPS is connected to a load impedance Z_L, which represents the antenna, while the other end is connected to the wave-port excitation. In HFSS, by default, the interface between all 3D objects and the background is a perfect E boundary through which no energy enters or exits. Waveports are typically placed on this interface to provide a window that couples the model device to the external world. HFSS assumes that each waveport defined in the model is connected to a semi-infinitely long waveguide that has the same cross-section and material properties as the port. When solving for the S-parameters, HFSS assumes that the structure is excited by the natural field patterns (modes) associated with these cross-sections. The 2D field solutions generated for each waveport serve as boundary conditions at those ports for the entire model.

We estimate the CPS parameters in two steps as follows: (1) compute the input impedance at the port as a function of CPS length *L*, keeping the strip width "*w*" and separation "*s*" constant, and, (2) fit the impedance versus CPS length curve thus obtained to the impedance transformation equation (3.1):

$$Z_{in} = Z_o\left(\frac{Z_L \cosh(\gamma.L) + Z_o \sinh(\gamma.L)}{Z_o \cosh(\gamma.L) + Z_L \sinh(\gamma.L)}\right) \quad \textbf{3.1}$$

$$\gamma = \alpha + j\beta \quad \textbf{3.2}$$

$$\beta = \frac{2\pi}{\lambda_{eff}} \quad \textbf{3.3}$$

$$\lambda_{eff} = \frac{\lambda_o}{n_{eff}} \quad \textbf{3.4}$$

where, Z_o is characteristic impedance of CPS, Z_{in} is input impedance at port, λ_0 is freespace wavelength, λ_{eff} and n_{eff} are the effective wavelength and refractive index,

respectively, in the substrate Z_o, n_{eff} and α are found by fitting the impedance transformation equation to the data obtained from HFSS by simultaneously varying these three unknowns. Each unknown has a particular effect on the Z_{in} versus CPS length curve; e.g., the value of Z_o defines the peak of the curve, n_{eff} defines the spacing between peaks, while α defines the damping. We extract the transmission-line parameters for different CPS designs using this approach [56], [57]. We validated this approach at 10 GHz as discussed in the following section.

3.1.1 Validation of computational approach at 10 GHz

In order to validate our approach, we begin with a transmission-line design with known parameters at 10 GHz. For the CPS design consisting of s = 272 μm, w = 317.5 μm on 635 μm-thick SiO_2, the analytical transmission-line parameters are: Z_o = 149 Ohm, n_{eff} = 1.548, and α = 0 Np/cm [23]. We compute the input impedance, Z_{in}, as a function of transmission-line length, L, obtained using these parameters in the usual impedance-transformation equation (3.1). We compare this data with the impedance at the port as a function of transmission-line length, obtained from HFSS. The overlaid plots in Figure (3.2) show excellent agreement between analytical transmission-line parameters and parametrically analyzed HFSS models. This agreement validates our computational approach, and allows us to apply it at the LWIR frequencies of interest.

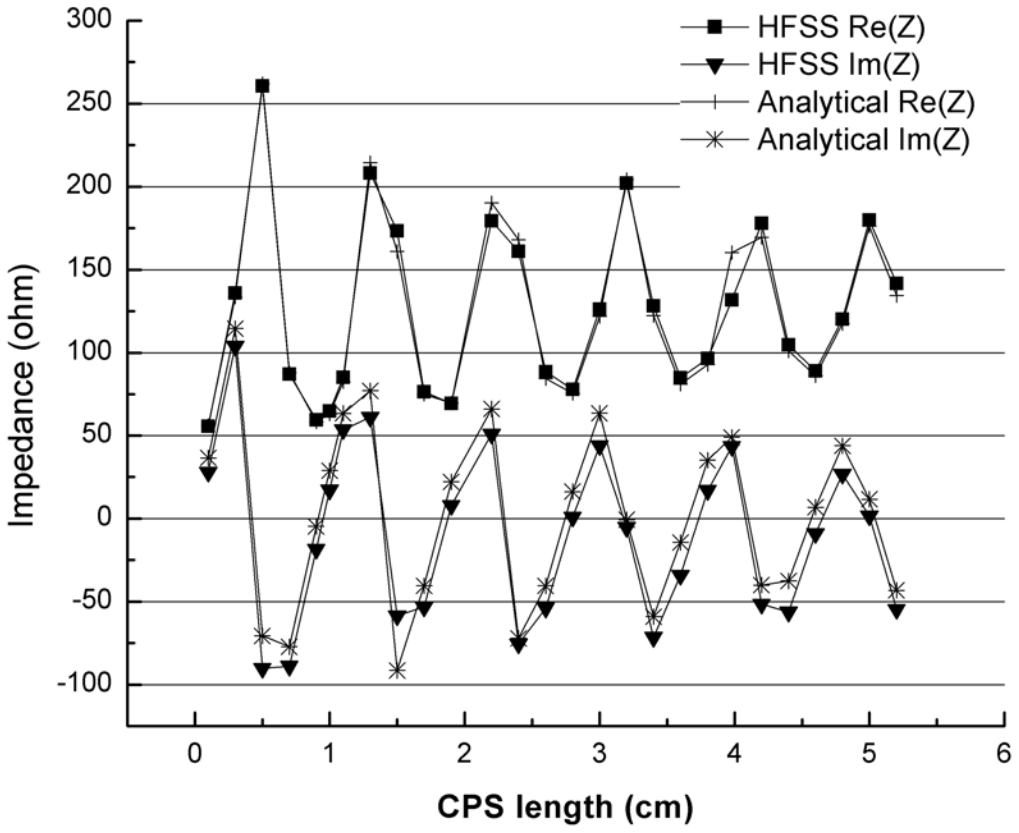

Figure 3.2 Analytical and computed impedance as a function of CPS length at 10 GHz

3.1.2 Parameter extraction at IR

We ran a number of models with different designs; in order to understand the effect of metal width *w* and strip separation *s*, we fixed one and varied the other. The transmission-line parameters for all designs using the SiO_2-on-Si substrate are shown in Figures (3.3) – (3.6). Figures (3.3) and (3.4) show the transmission-line parameters for fixed metal strip width *w* and as a function of strip separation *s*. Both the characteristic

impedance and attenuation constant increase with separation s. The n_{eff} increases with strip separation as well.

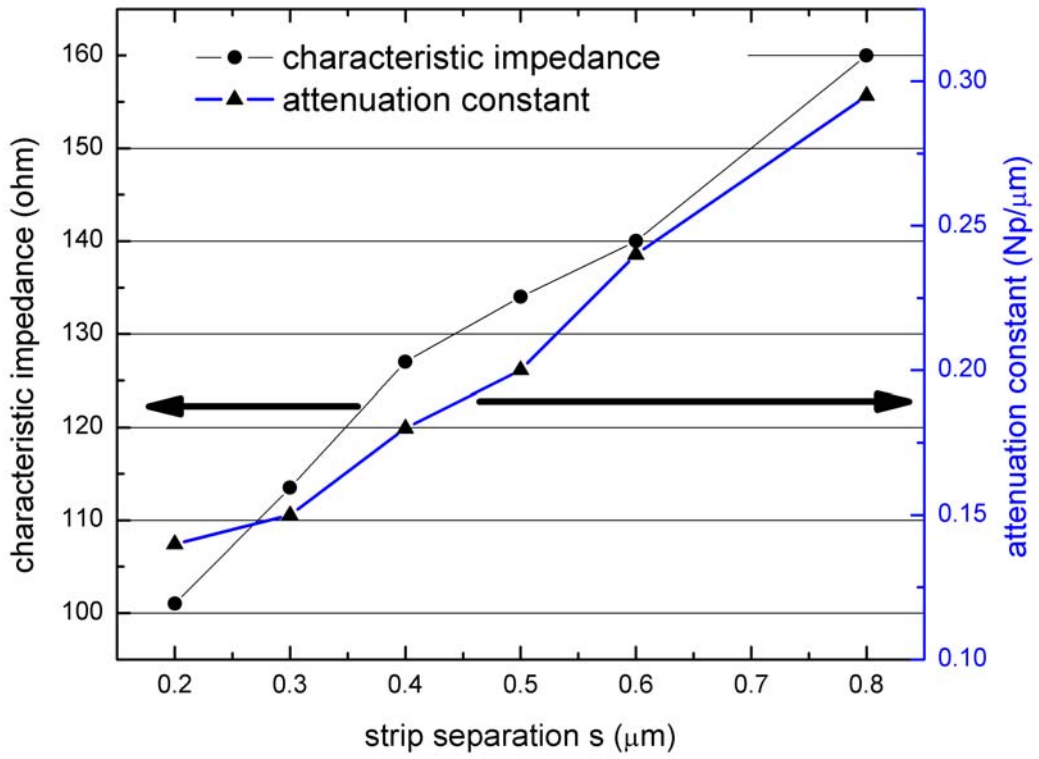

Figure 3.3. Computed Z_o and α for CPS design having fixed w = 600 nm for SiO_2 on Si substrate

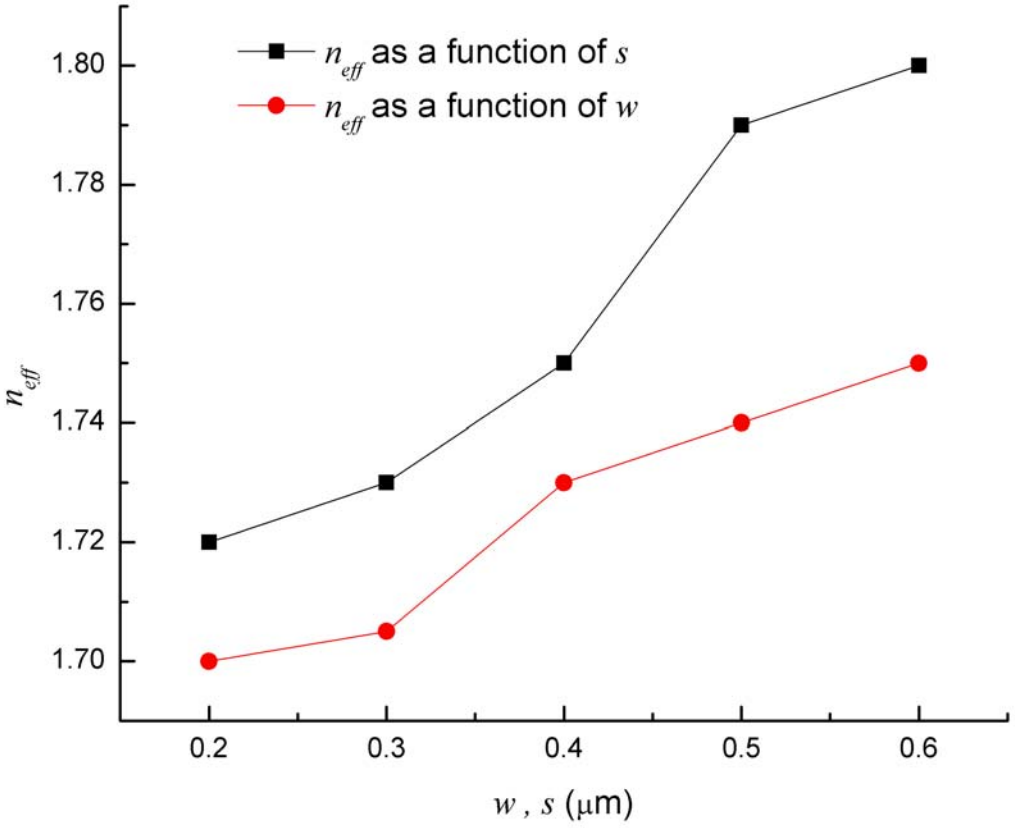

Figure 3.4. Computed effective index for CPS design with fixed w = 600 nm and fixed s = 400 nm for SiO_2 on Si substrate

When the strip separation s is kept constant, the characteristic impedance decreases with increasing w while the attenuation constant and the n_{eff} increases (Figure 3.5 and 3.7), increases also. Figure (3.7) further shows that the n_{eff} increases with CPS metal-strip width, when s is kept constant.

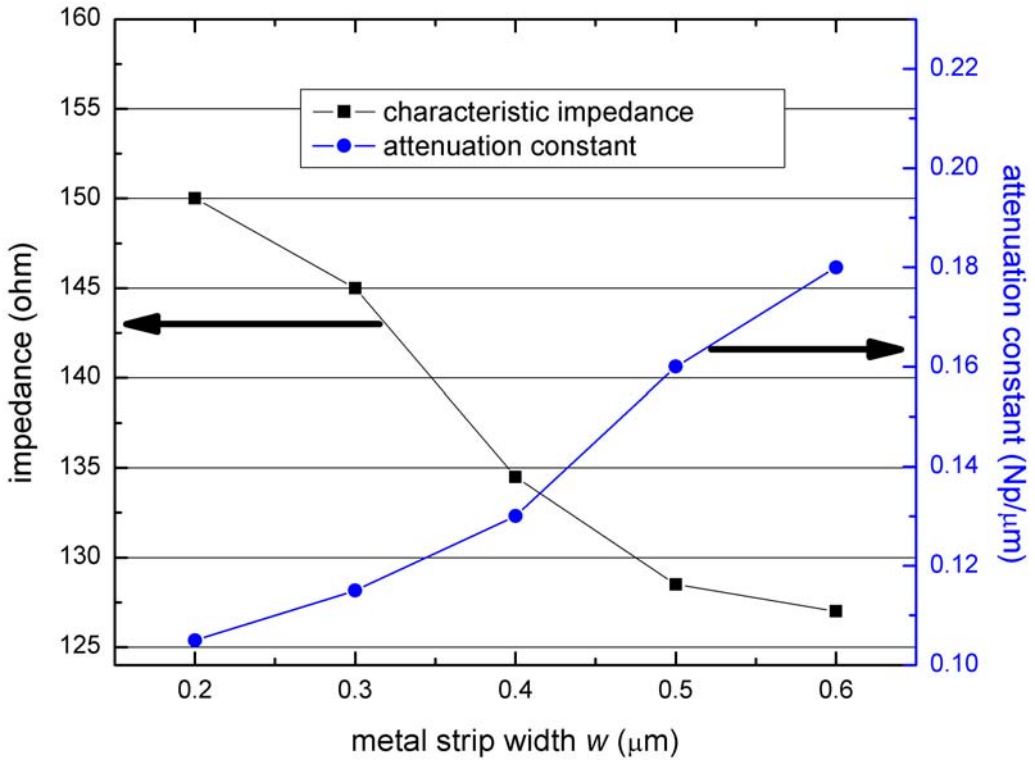

Figure 3.5. Computed Z_o and α for CPS design, on SiO2 on Si substrate, for fixed s = 400 nm

The transmission-line parameters for different designs on the high resistivity Si substrate are shown in Figures (3.6) – (3.9). We find that all the three transmission-line parameters increase, as a function of *s* and fixed *w*, as shown in Figures (3.6) - (3.8). When *s* is held constant, the characteristic impedance decreases as a function of *w*, but effective index and attenuation constant increase, as shown in Figures (3.7) and (3.8). This behavior is similar to the case of SiO_2 on Si substrate, as expected. The attenuation constant for the high resistivity Si substrate is lower compared to thermal SiO_2 on the low resistivity Si substrate.

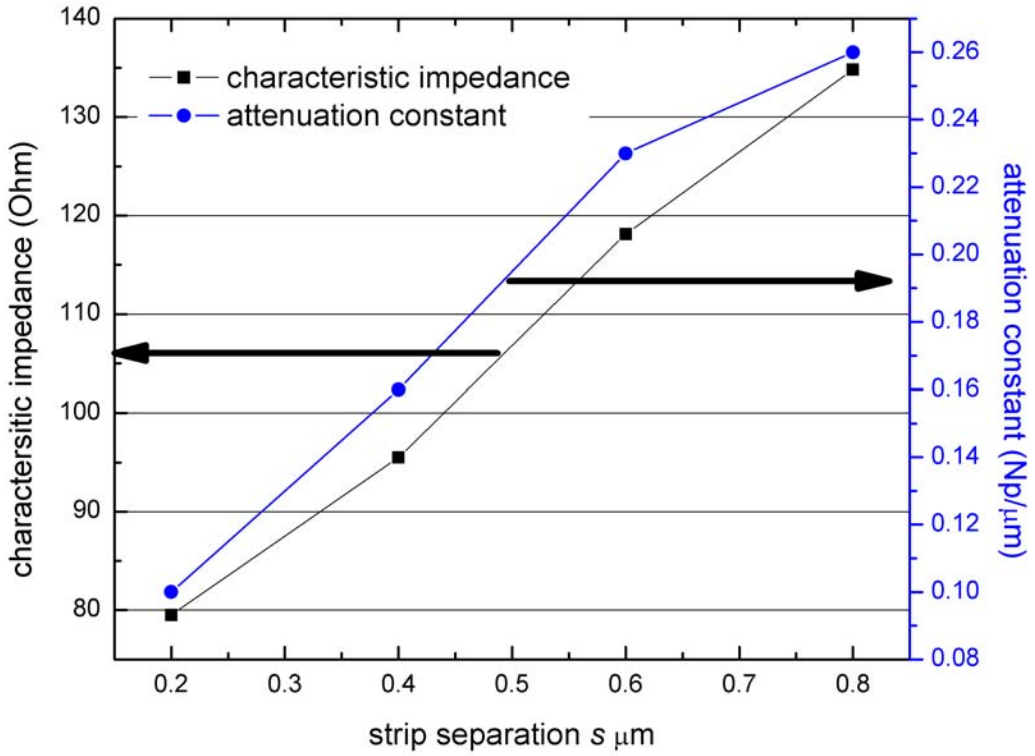

Figure 3.6 Computed Z_o and α for CPS design, on high resistivity Si substrate, for fixed w = 200 nm

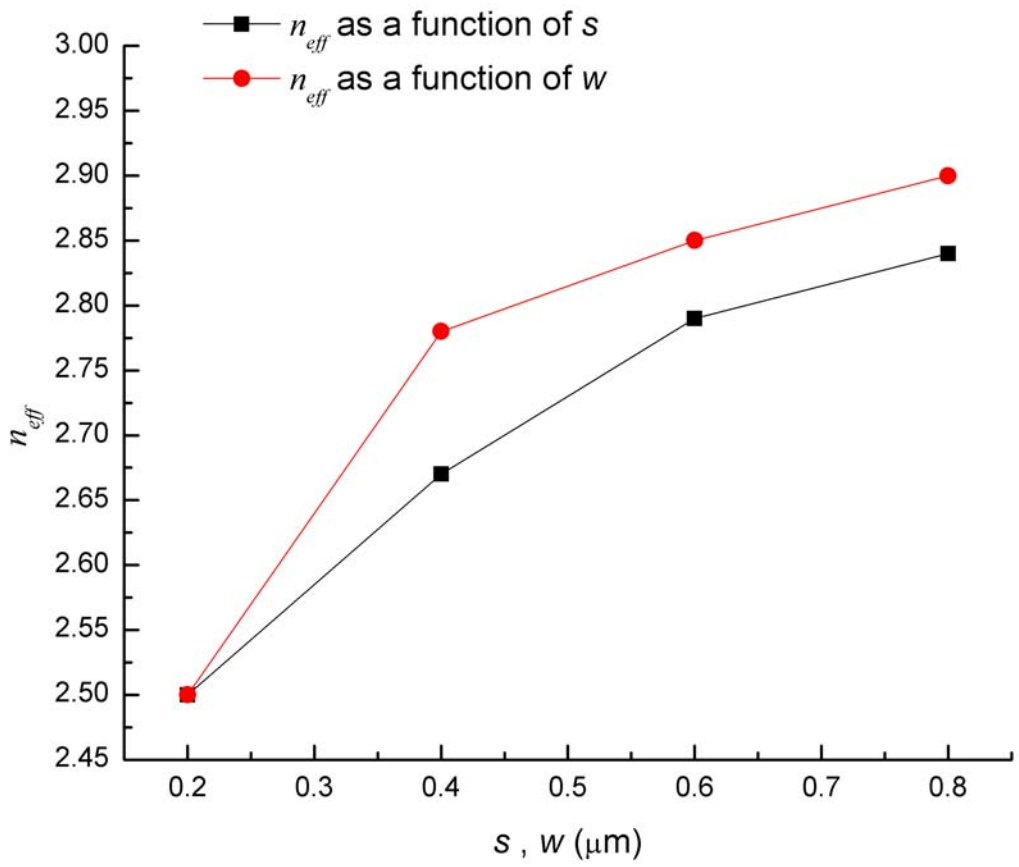

Figure 3.7 Computed effective index for CPS design on high resistivity Si with fixed w = 200 nm and s = 200 nm

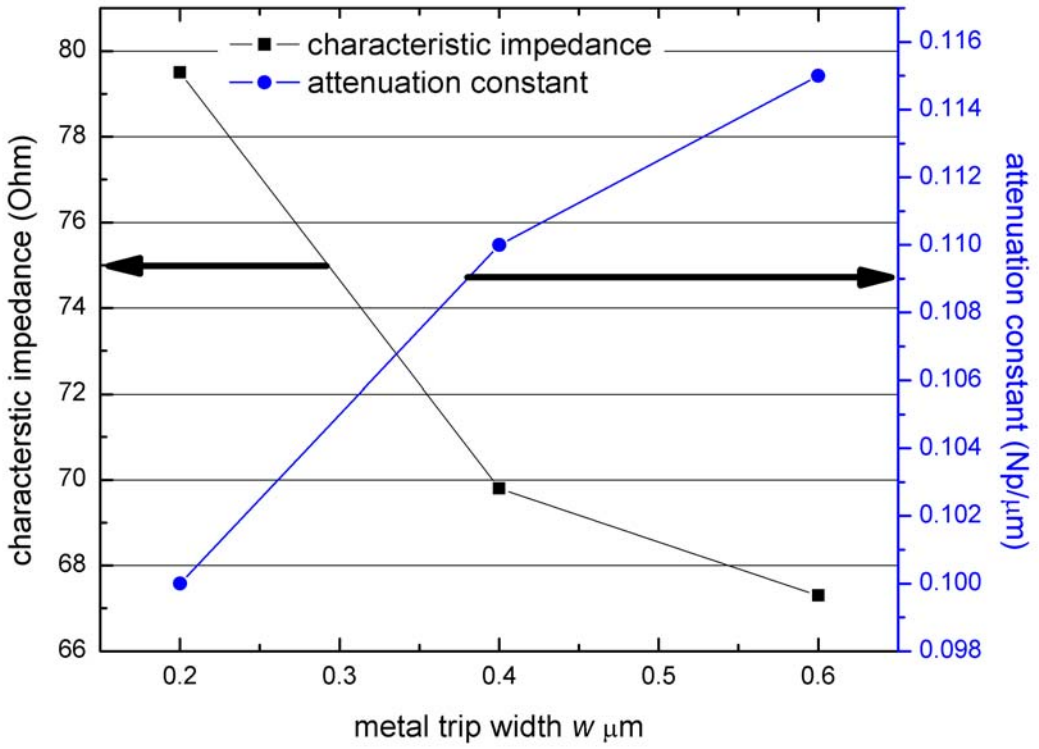

Figure 3.8 Computed Z_o and α for CPS design, on high resistivity Si, having fixed s = 200 nm

3.1.4 Response calculation

In the models for parameter extraction, we had one end of the transmission-line connected to the lumped load (Z_L) and the other to the port. For response calculation, we replace the lumped load by a dipole resonant at 28.3 THz (λ_0 = 10.6-μm) and calculate the square of current at the port (response) as a function of CPS length (Figure 3.9). This quantity is proportional to the I^2R power dissipated in the bolometer (where I is the current and R is the resistance of bolometer), and hence is directly comparable to the voltage response of the bolometer in the fabricated device. Calculated normalized

response for the design consisting of w = 600 nm, and s = 400 nm on SiO_2-on-Si substrate is shown in Figure 3.10.

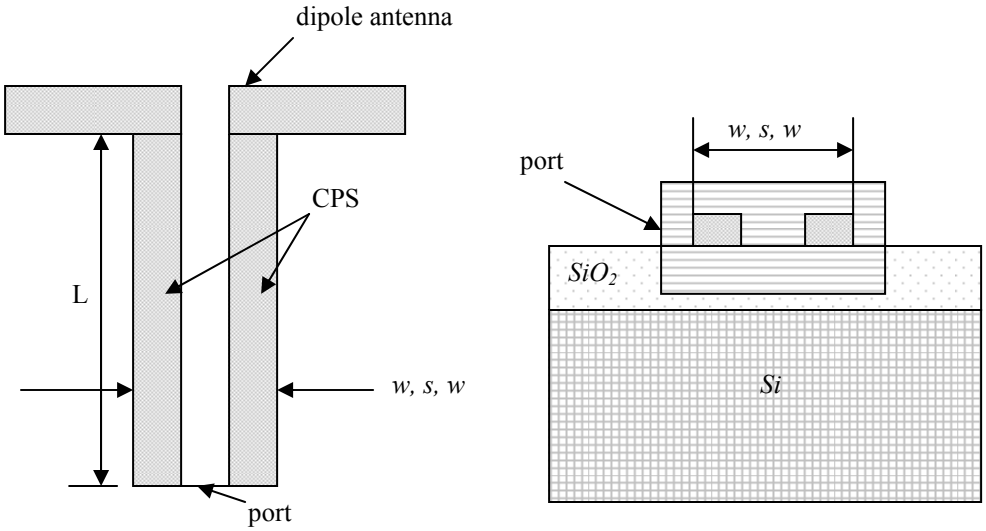

Figure 3.9 HFSS model for response calculation

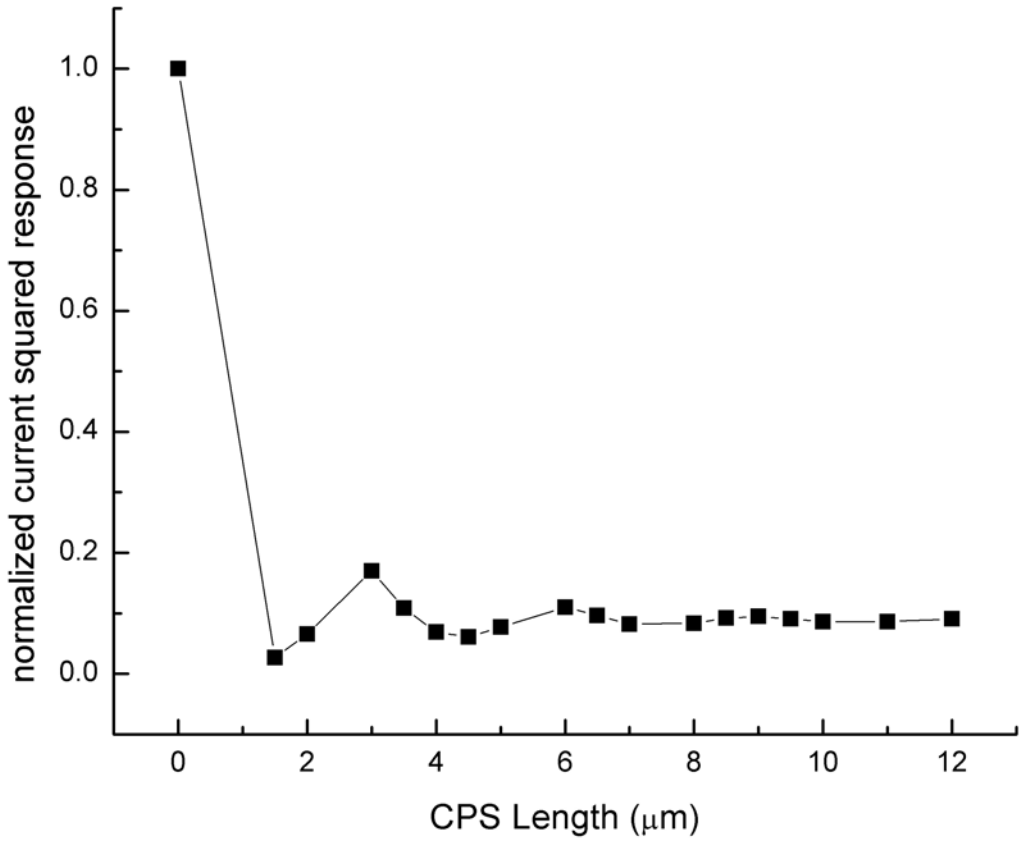

Figure 3.10 Normalized port current squared (response), computed as a function of CPS length

3.2 Fabrication of antenna connected to CPS

We fabricated dipole antennas, designed to resonate at 28.3 THz connected to CPS lines of different lengths ranging from 0 μm to 5.75 μm in steps of 0.25 μm (Figure 3.11). All the devices in the CPS study were patterned on 3-inch, 380-μm thick low resistivity silicon substrates, coated with 1.19-μm of SiO_2 for thermal and electrical isolation. The chosen standoff height is such that the cut-off frequency of lowest order

surface-wave mode (TE_1) is higher than our operating frequency, as calculated from eq. (2.8), hence avoiding any surface wave modes.

The dipole arms were 0.6-μm wide and each arm length is 1.5 μm, with the separation of 400 nm between the arms. The width of CPS was 0.6-μm and separation between them was 400-nm. A bolometric detector, 1.2 μm × 0.5 μm, was fabricated at the other end of CPS. Connecting the CPS to the bondpads, for dc biasing of bolometer were 20-nm wide and 25-μm long bias lines.

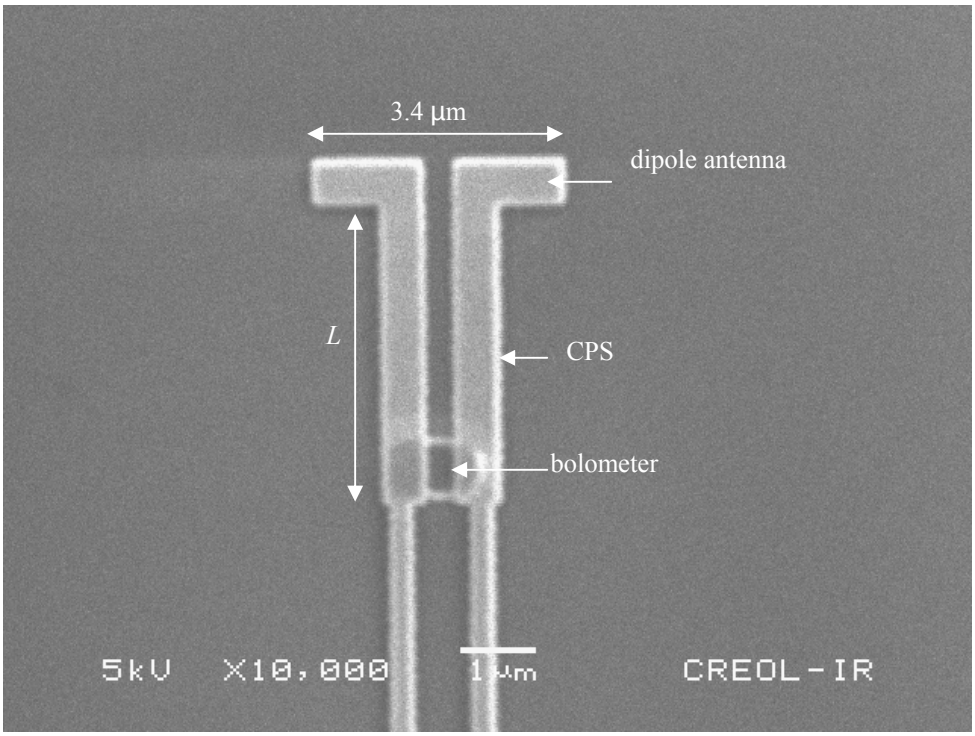

Figure 3.11 Fabricated CPS connected dipole

The substrates were spin-coated with a bilayer of copolymer methyl methacrylate/methacrylic acid (MMA(8.5)MAA) and A4 950k polymethyl methacrylate (PMMA). This PMMA is diluted to 4% in the solvent anisole and has a molecular weight of 950k. A 350-nm layer of copolymer was obtained by spin coating at 2000 revolutions

per minute (rpm) for 60 seconds and baking on a hotplate at 180 ^{o}C for 10 minutes. A second layer of 200 nm thick PMMA was spun onto the substrate at 3000 rpm for 1 minute and baked afterwards for 10 minutes on a 180 ^{o}C hotplate.

The antenna, bolometer, bond-pads and bias lines were patterned using a Leica EBPG5000+ electron beam lithography system. The first layer in the fabrication process consists of antennas, bias lines and bondpads which were exposed at a dose of 600 $\mu C/cm^2$ and with a beam current of 15 nA. After exposure, the devices were developed for 1 minute in a 3:1 solution of IPA: MIBK rinsed with IPA and blow-dried with a nitrogen gun. They were then metallized. Afterwards, the bolometers were written with an e-beam current of 5 nA at a dose of 700 $\mu C/cm^2$, and developed for 1 minute in a 3:1 solution of IPA: MIBK.

The antennas were made of 100 nm of e-beam evaporated gold (Au) over a 7 nm adhesion-layer of chromium (Cr). Lift off was done using methylene chloride. The bolometers were made of 120 nm of dc-sputtered nickel (Ni), and the lift off process also used methylene chloride.

3.3 Experimental method and results

We measured the voltage (response) at the bolometer as a function of CPS length. Other modeled parameters such as characteristic impedance, attenuation constant and effective index cannot be measured directly in the laboratory. However the only directly measurable quantity is the antenna response. So we compute, measure and compare the response of the dipole antenna connected to these transmission lines as a function of transmission-line length. The measured response is proportional to the I^2R power dissipated in the bolometer (where I is the current and R is the resistance of bolometer)

and we compare this quantity with the current squared at the bolometer (port) computed from our model. This current depends on the impedance at bolometer (port) location which in turn is the impedance of the dipole antenna transformed along the CPS length based on transmission-line parameters and hence directly related to the computed Z_o, n_{eff} and α of that particular CPS design. Thus our response measurement can be related to the modeled transmission-line parameters and their validity can be confirmed.

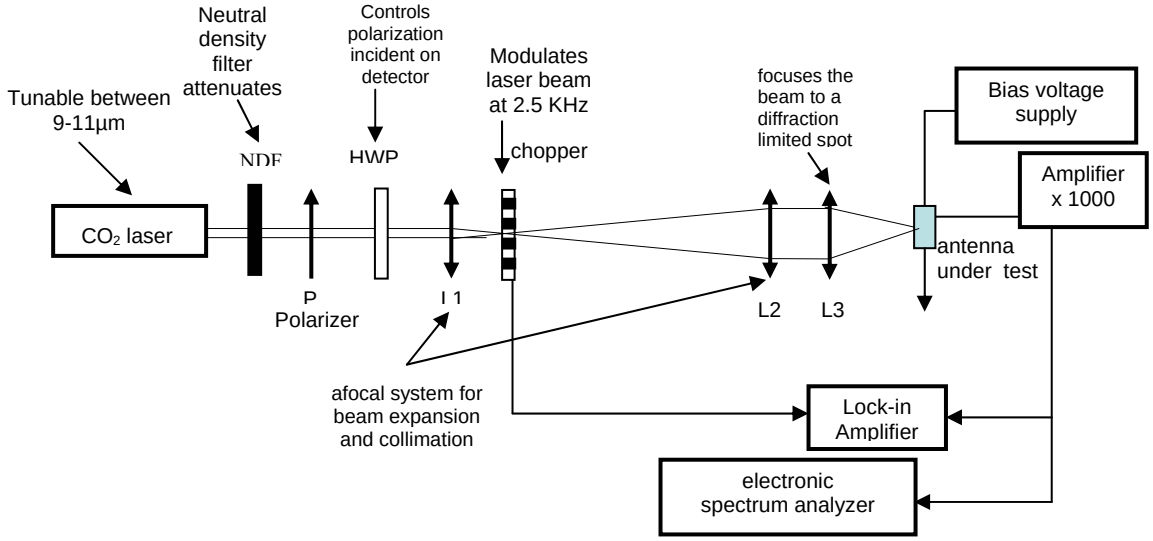

Figure 3.12 Test setup for response measurement

The device measurement was carried out using test setup shown in Figure 3.12. Two sets of measurements were performed; one with the CO_2-laser beam at 10.6 µm focused by an F/8 optical train and the other set of measurements with the same laser focused by an F/1 optical train. The polarization was linear and was rotated by means of a half-wave plate (HWP) to test the polarization sensitivity and to confirm the orientation of dipole. The bolometer under test was biased at 100 mV and placed at the focus of the laser beam using motorized stages with submicron accuracy. The laser beam was

modulated with a chopper at a frequency of 2.5 kHz and the modulated signal produced by the bolometer was read with a lock-in amplifier after a 1000 × preamplification.

For the set of measurements carried out using F/8 optics, we measured at normal incidence the response to radiation polarized along the dipole arm. The data from this measurement are overlaid with the computed current-squared response as shown in Figure 3.13.

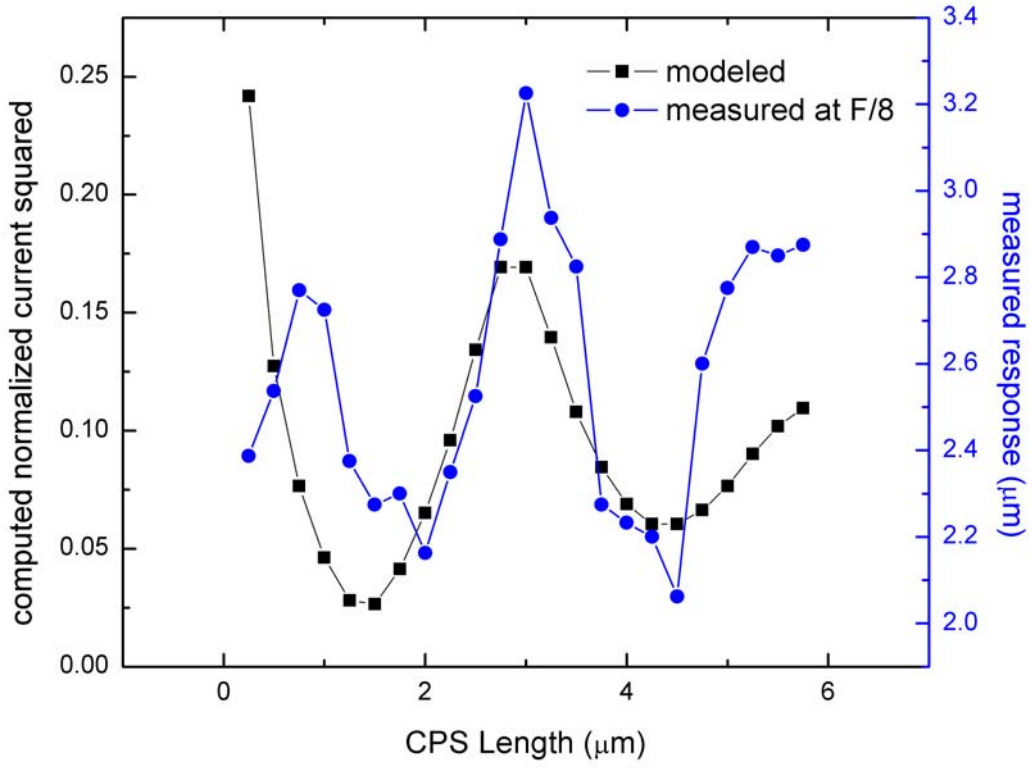

Figure 3.13 Device response measured using F/8 optics

To better understand the signal propagation along the transmission line, we extended the CPS length study up to 12 μm, fabricating dipole antenna connected to CPS lines in length increaments of 0.5 μm. The testing of these devices was carried out using

an F/1 beam producing the laser spot diameter of about 30 μm. We obtained antenna response map for each device with a scan step size of 1 μm. As a result a 2D map of the response of the antenna was obtained which represents the convolution between the detector's spatial response and the laser beam shape [58]. The 2D map was recorded using the linear polarization state that produced both the strongest signal and the weakest signal. Figure 3.14 shows this convolution for the device with CPS length of 1.5 μm for the polarization that produced the strongest signal. The 2D maps were recorded for each device to accurately obtain the response due to antenna and to distinguish between the bondpad response and antenna response. We find that as the length of CPS increases, the antenna response decreases because of the increasing attenuation along the transmission line. Figure 3.15 shows a deconvolved 2D antenna response overlaid on the device for the case where L = 3 μm. There are 10 contours that represent 95% of the total response.

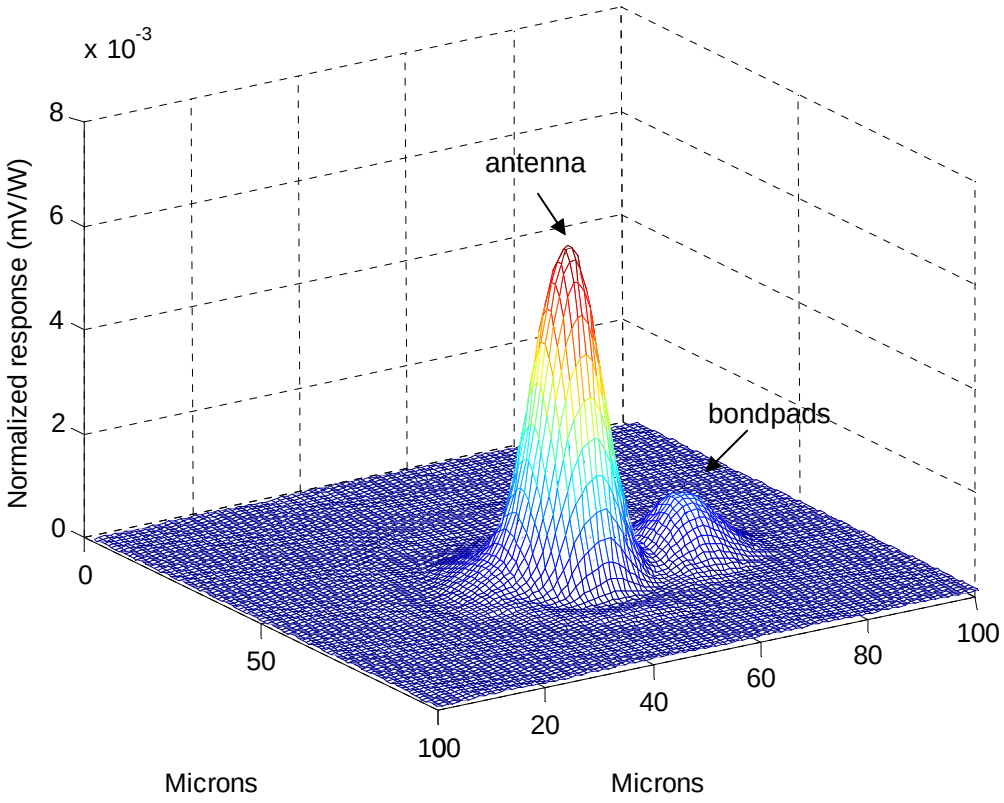

Figure 3.14 Convolution between laser beam and detector response for L = 1.5 μm

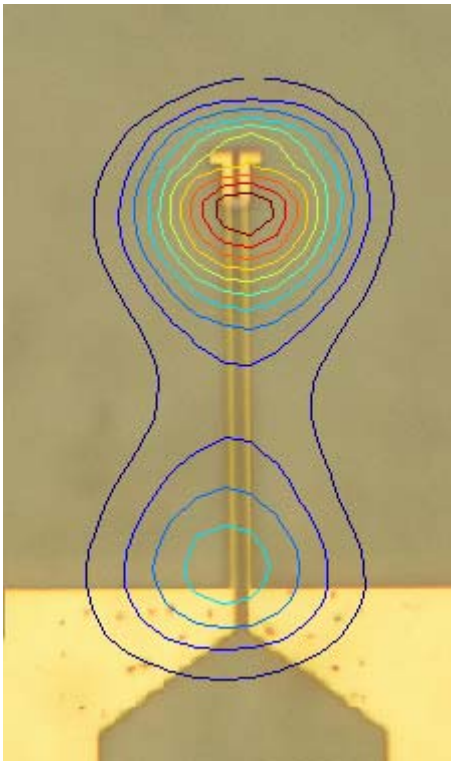

Figure 3.15 Deconvolution of 2D map and laser beam for CPS L = 3 μm

The antenna response at maximum polarization plotted as a function of CPS length, along with the computed port current squared is shown in Figure 3.16. They show excellent agreement, hence, further validating our extracted transmission-line parameters.

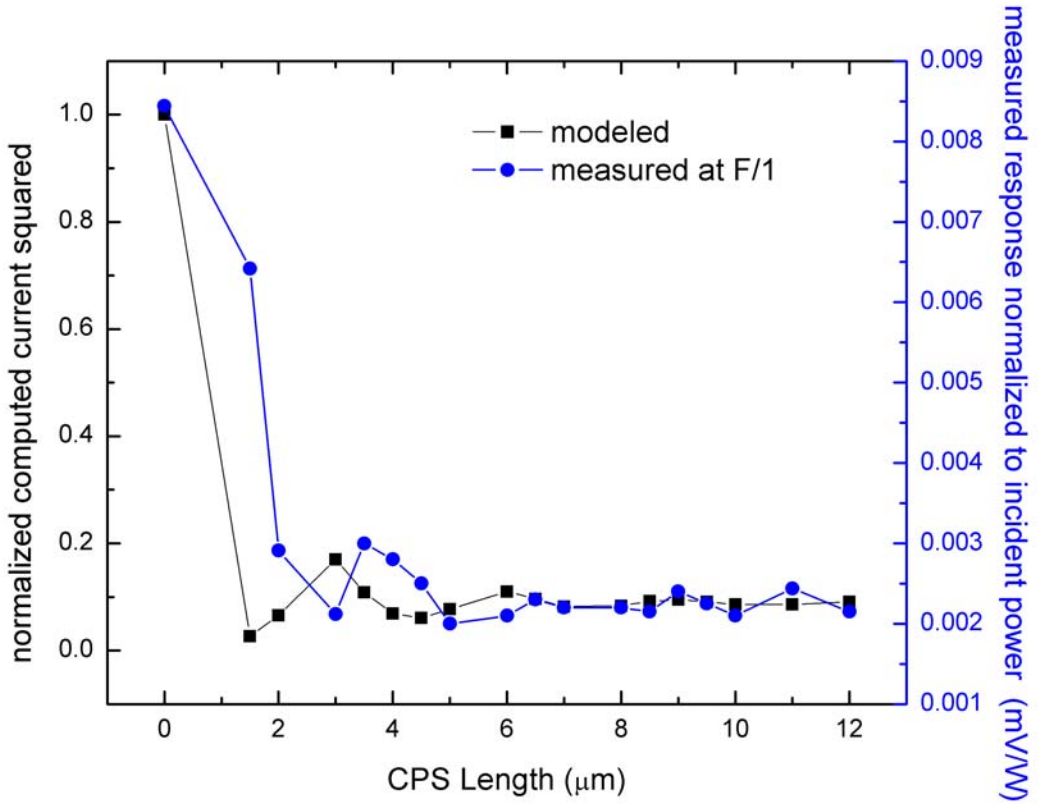

Figure .3.16 Comparison of modeled and measured response at F/1

To summarize, we characterized the CPS lines through modeling, fabrication and response measurement. We modeled CPS on two different substrates to extract transmission-line parameters for different designs and studied the trends for the Z_o, α and n_{eff}. Since these transmission-line parameters cannot be measured directly, we used antenna response as a means to validate the extracted transmission-line parameters. Our measured response was in good agreement with modeled response validating the extracted transmission-line parameters and hence validating our characterization procedure.

CHAPTER 4 MICROSTRIP LINES

The microstrip line (MS) configuration consists of a signal strip and a ground plane separated by a substrate of height *h* (Fig. 2.6). When a signal propagates along the MS the modes are confined in the substrate between the signal strip and the ground plane. As a result of this field confinement the MS is expected to have lower attenuation compared to CPS configuration. However, since the signal propagates through the substrate, the substrate losses are important in determining the attenuation for the MS system.

4.1 Numerical characterization of MS

We extract the transmission-line parameters and compute the current response for the microstrip line with HFSS, using the same approach as applied for the CPS lines (Section 3.1.1). Transmission-line parameters, Z_o, α, n_{eff}, are extracted as a function of MS width and as a function of substrate height *h* above the ground plane for different substrate types: PECVD deposited SiO_2, zirconium dioxide (ZrO_2) and benzocyclobutene (BCB, also called cyclotene).

The HFSS model shown in Figure 4.1, which consists of a 150 nm thick Au MS on a SiO_2 layer of thickness *h* backed by Au finite ground plane. We used thermal and PECVD deposited SiO_2 substrates in our models. Models are constructed using the material parameters of Au and SiO_2 obtained from IR-VASE (Table 2.1).

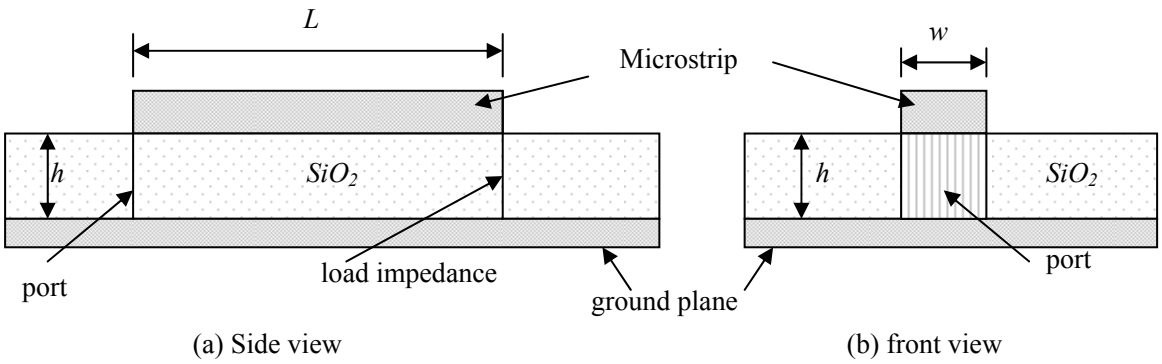

Figure 4.1 HFSS model for MS characterization

In the model used for parameter extraction, a load resistance is connected between one end of MS and the ground plane and an excitation port is connected between the other end of MS and the ground plane.

4.1.1 Validation of computational approach at 10 GHz

The MS design at 10 GHz consists of w = 182 μm on a 254 μm-thick Si substrate with conductivity of 0.1 S/m with analytical transmission-line parameters: Z_o = 50 Ohm, n_{eff} = 2.775, and α = 0.051 Np/cm [59]. These parameters were used in the usual transmission-line equation and the impedance versus MS length data was obtained. This MS design was parametrically analyzed in HFSS and the impedance at the port was computed as a function of MS length. The impedance computed using both methods are overlaid in Figure 4.2 and show excellent agreement. This agreement validates our computational approach for the MS lines.

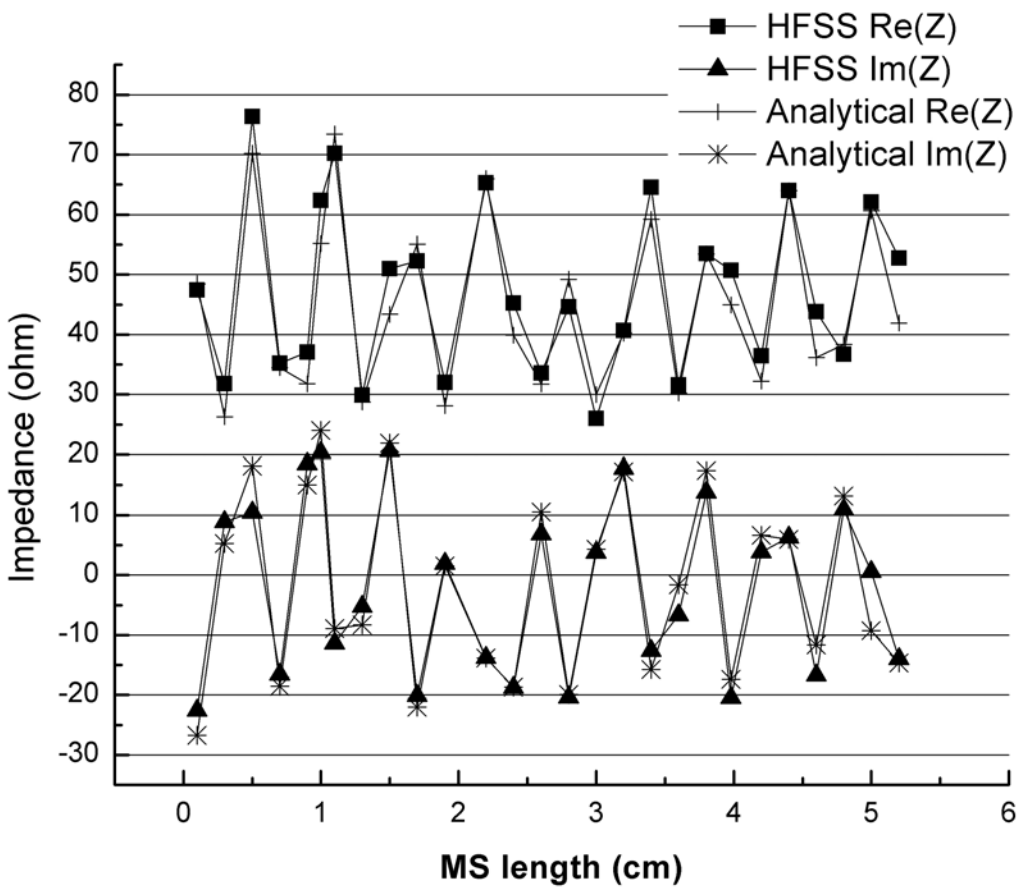

Figure 4.2 Analytical and computed impedance as a function of MS length at 10 GHz

4.1.1.2 MS transmission-line parameters on different substrates

We studied MS on three different types of substrates: PECVD deposited SiO_2, ZrO_2 and cyclotene (BCB). The fabrication of MS requires etching of the standoff layers to form bolometers (modeled as ports between ground plane and MS). Hence two criteria were important in considering the standoff layers: losses in the standoff and feasibility of etching. PECVD deposited SiO_2 has higher losses than ZrO_2 and cyclotene but is easy to etch in an RIE system, while ZrO_2 has lower loss but requires inductively coupled plasma

etching system which was not accessible. A wafer coated with sputter deposited 60 nm thick ZrO_2 having Ti-Ni (20 nm-200 nm) etch mask with windows for etching ZrO_2 was prepared by wet etching Ni and Ti and sent to Penn State University for dry etching ZrO_2 in an inductively coupled plasma etching system. The etch was performed for a minute. We found that the process did not etch ZrO_2 all the way down as was needed for these devices. So, we used BCB as the standoff layer which satisfies both criteria, it has low loss and also can be etched in an RIE system.

Transmission-line parameters were extracted for different designs of all these substrates. Microstrip lines have essentially two design variables: the metal strip width *w* and substrate thickness *h*. For all the substrates we ran the models with *w* varying between 0.2 μm – 1 μm in steps of 0.2 μm. The substrate thickness *h* was varied according to Table 4.1.

Table 4.1 standoff layer height variation for T-line parameter extraction

Substrate material	Substrate height variation (*h*) nm
PECVD deposited SiO_2	150, 200, 300
ZrO_2	60, 80, 470
Cyclotene (BCB)	200, 260, 330

The transmission-line parameters extracted for different standoff layers are shown in Fig. (4.3) – (4.5). We find that as the width *w* increases, the characteristic impedance decreases for all values of *h*, giving lowest values for the smallest *h*. The effective index of refraction is lower for thicker substrates and increases as a function of *w*. The

attenuation constant is higher for thicker substrates and also increase with *w*. It is also seen the computed attenuation is highest for PECVD deposited SiO_2 and lowest for BCB.

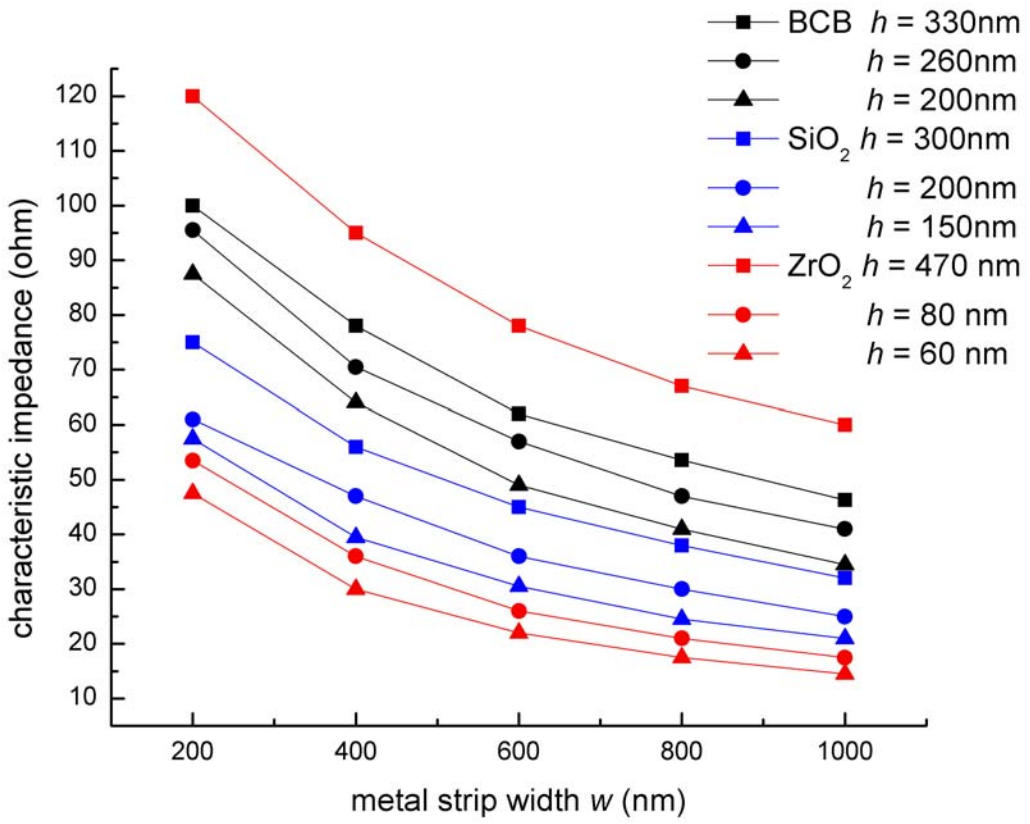

Figure 4.3 Computed characteristic impedance of MS as a function of *w* and *h*

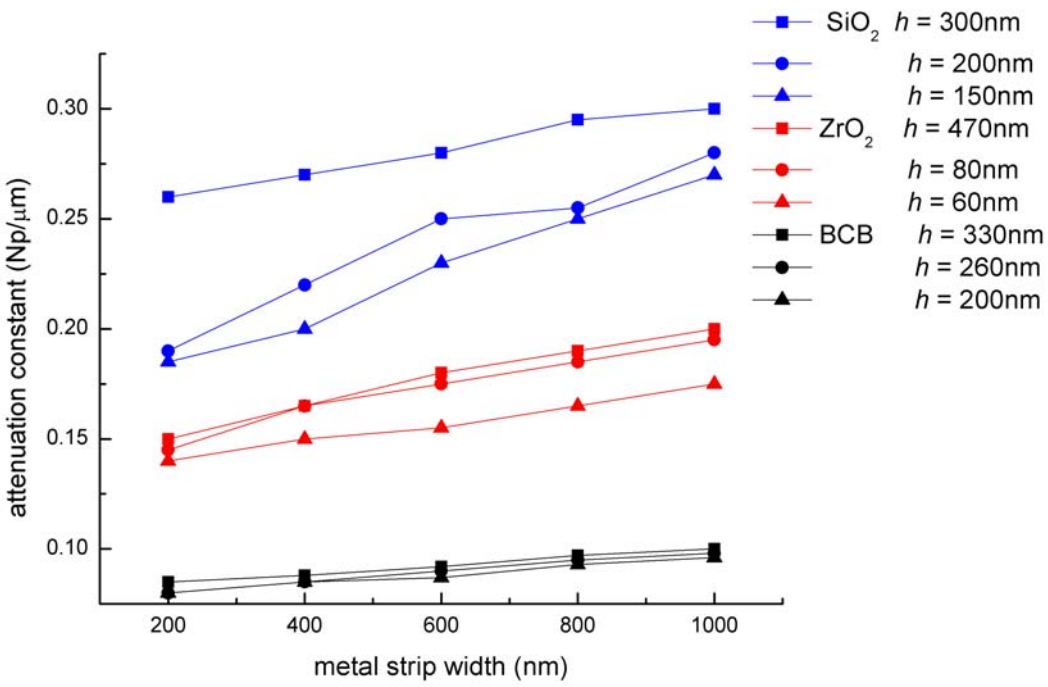

Figure 4.4. Computed attenuation constant of MS as a function of *w* and *h*

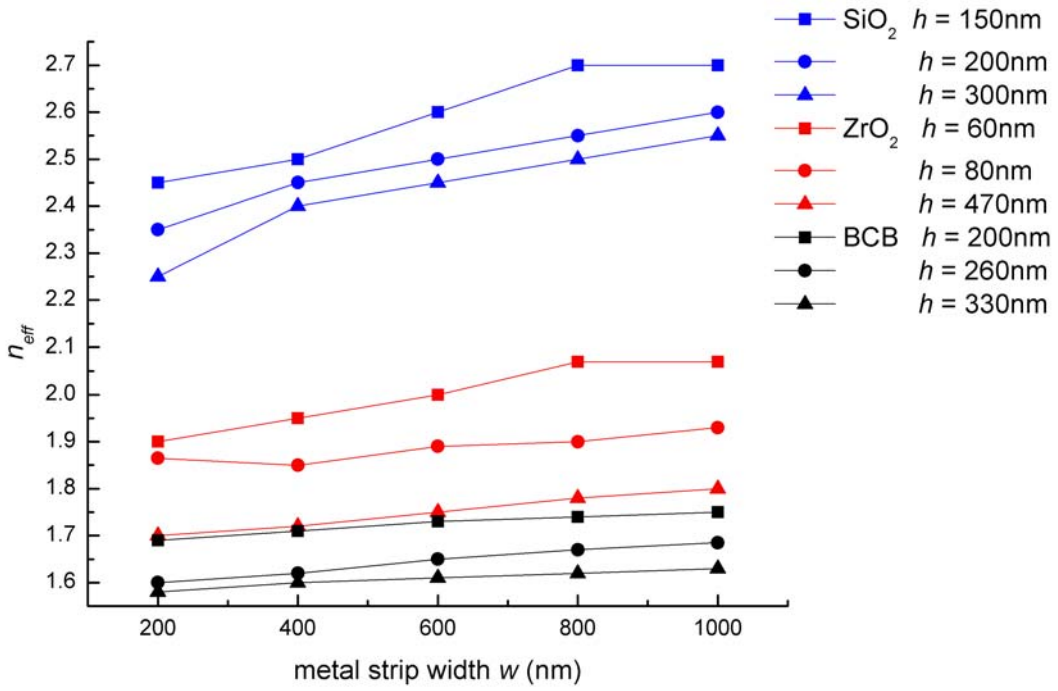

Figure 4.5. Computed effective index of refraction of MS as a function of *w* and *h*

4.1.2. Response calculation

Figure 4.6 shows the HFSS model used to calculate the current response of a dipole antenna connected to MS. The port is vertically connected between the MS and ground plane. The dipole half arm length is 1.1 μm with a separation of 0.4 μm. Response is calculated by computing the current-squared at the port as a function of MS length. Figures 4.7 presents the normalized current squared response for the MS on BCB and SiO2 standoff layers for $w = 0.4$ μm.

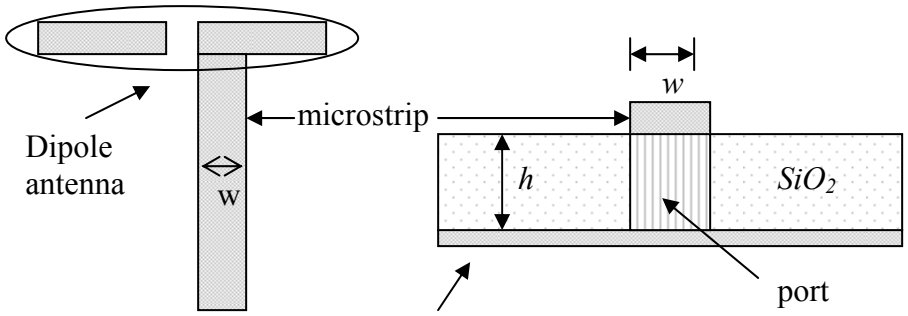

(a) top view (b) front view

Figure 4.6 Model for response calculation

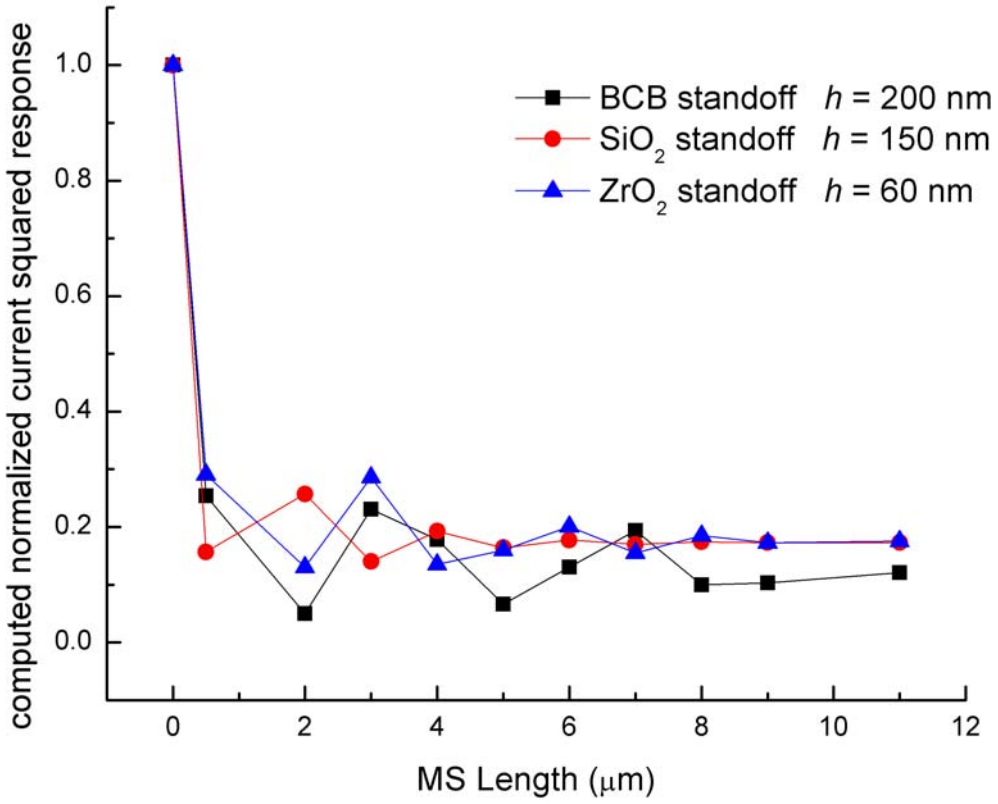

Figure 4.7 Normalized current-squared response, computed for w = 0.4 μm

4.2 Fabrication and response measurements

We studied microstrip lines at 10.6 μm wavelength by fabricating dipole antenna connected to MS on two standoff layers: SiO_2 and BCB. We first fabricated the devices

on SiO_2 and the response measurement showed excessive losses, which rendered the results inconclusive. So, we tried to use ZrO_2 as standoff layer but the etching of ZrO_2 for forming the bolometer (via) was not successful. Finally, we used BCB as standoff to fabricate another set of devices and performed the response measurements. The fabrication process and measurement results for both are discussed in following sections.

4.2.1 Fabrication of MS on PECVD deposited SiO_2 standoff

We fabricated dipole antennas connected to microstrip line of length *L*, where *L* ranges from 1.5 μm to 11 μm in steps of 0.5 μm. As shown in Figure 4.8, the dipole antenna had two arms, each, 1.1 μm in length and 0.6 μm in width, separated by a gap of 0.4 μm, hence making the total antenna length to be 2.6 μm. The substrate consisted of 150-nm thick silicon dioxide (SiO_2) backed by finite ground plane on top of Si wafer. The SiO_2 was deposited using plasma enhanced chemical vapor deposition (PECVD). The dipole antenna is located in the center of a 90 μm × 90 μm finite ground plane. The MS was located on one of the arms, toward the center of the dipole, and was connected to the bolometer which actually was a via, of size 300 nm × 300 nm, etched into SiO_2, using reactive ion etching (RIE), and then metallized, so that it electrically connects the dipole arm and MS to the ground plane. The bolometer was connected to a dc lead line which in turn was connected to a bondpad for signal extraction. The second bondpad was revealed by etching a 350 μm × 300 μm area of SiO_2 and then metallizing it, such that it is connected to the ground plane.

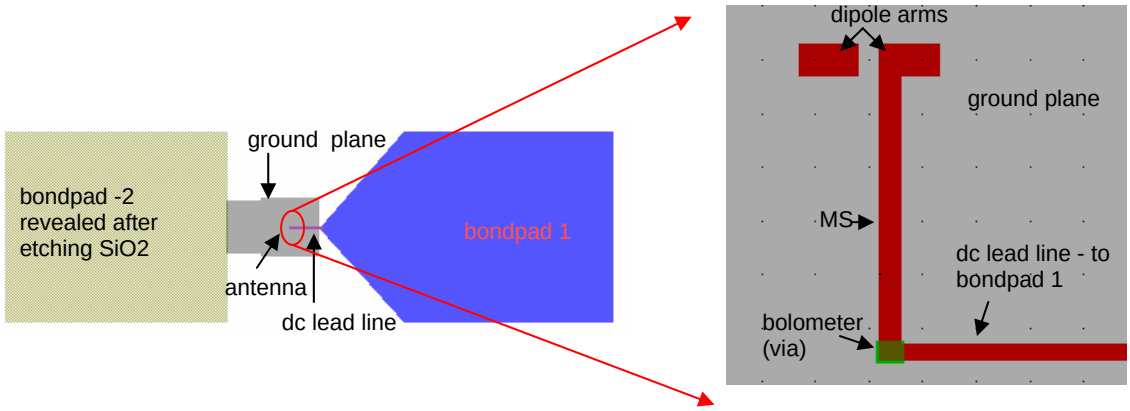

Figure 4.8 Top view of the device to be fabricated

The devices were fabricated on 3 inch low resistivity Si wafer coated with SiO_2 (1.19 μm thick) on both sides. Fabrication was done using the Leica EBPG5000+ system, operating at 50 kV. Before coating the resist the wafer was spin rinsed at 4000 rpm for 60 s with acetone, methanol and isopropanol. Dehydration baking was done for 3 min at 180 C. The bilayer e-beam sensitive resist used for all steps except for the one which required etching (for bolometer and one of the bondpads) consisted of a ZEP520A-7 layer spun at 300 rpm-700 rpm-3000 rpm, for 15 s-5 s-80 s (~ 250 nm total thickness) and baked for 3 min at 180 C, on top of PMGI SF7 spun at 300 rpm-700 rpm-3000 rpm for 15 s-5 s-80 s (~ 450 nm total thickness) and baked for 4 min at 180 C. During the etching process, some of the resist layer is etched as well. Metallization is done after etching without any lithography and to ensure successful liftoff there should be thick enough resist (at least two times the thickness of metal to be deposited, 300 nm in this case) left after etching. For this reason, thicker layers of ZEP520A (spin speed 300 rpm-1800 rpm for 15s-60s, ~500 nm total thickness) on top of PMGI SF7 (spin speed 300 rpm-2000 rpm for 15 s-60 s, ~500 nm total thickness) were used.

The antennas, microstrips, bolometers, finite ground planes as well as bondpads were made of e-beam evaporated 150 nm Au with a 10 nm Ti adhesion layer. This Ti adhesion layer was used on top as well as on the bottom of the finite ground plane to ensure adhesion of SiO_2 layer deposited over it. The excess metal was removed by rolling a scotch tape over the wafer and gently pulling it off. ZEP was removed by ultrasonic assisted methylene chloride bath and we used an EBR-PG ultrasonic bath to remove PMGI SF7.

The finite ground plane (90 μm × 90 μm) and alignment marks were patterned simultaneously in the first step of lithography, with the doses of 185 $\mu C/cm^2$ and 300 $\mu C/cm^2$ and beam currents of 25 nA and 8 nA respectively. A two step development process consisted of first developing the exposed ZEP for 55 s in xylene (ZEP RD) and rinsing with IPA and then developing the exposed PMGI for 20 s in TMAH (MF701) and rinsing with DI water.

In the next step, a 150 nm thick SiO_2 layer was deposited using PECVD, with the following process parameters giving a deposition rate of 50 nm/min: 1050 mTorr pressure, 400 sccm SiH_4, 827 sccm NO_2, and 25 W RF power. The next step in fabrication was to write and etch the via (300 nm × 300 nm) through the SiO_2 layer all the way to the ground plane and metallize it so as to form a bolometer. At the same time, one window was patterned, etched and metallized to form one of the bondpads (350 μm × 300 μm) connected to the ground plane. The via and bondpad were written at the doses of 250 $\mu C/cm^2$ and 185 $\mu C/cm^2$ and beam currents of 8 nA and 25 nA. They were etched and then metallized without requiring a separate lithography step for metallization. Etching

was performed in an RIE system with the following process parameters giving a removal rate of 50 nm/min: 75 mTorr pressure, 45 sccm CF_4, 5 sccm O_2, and 175 W RF power.

Finally, the antenna (arm 1.1 μm × 0.6 μm), microstrip (0.4 μm × L), and dc lead line (90 μm × 0.3 μm) were patterned using a dose of 300 μC/cm^2 and a beam current of 8 nA; the second bondpad (300 μm × 300 μm) is patterned using a dose of 185 μC/cm^2 and a beam current of 25 nA, and then metallized. The scanning electron micrograph of fabricated device is shown in Figure 4.9.

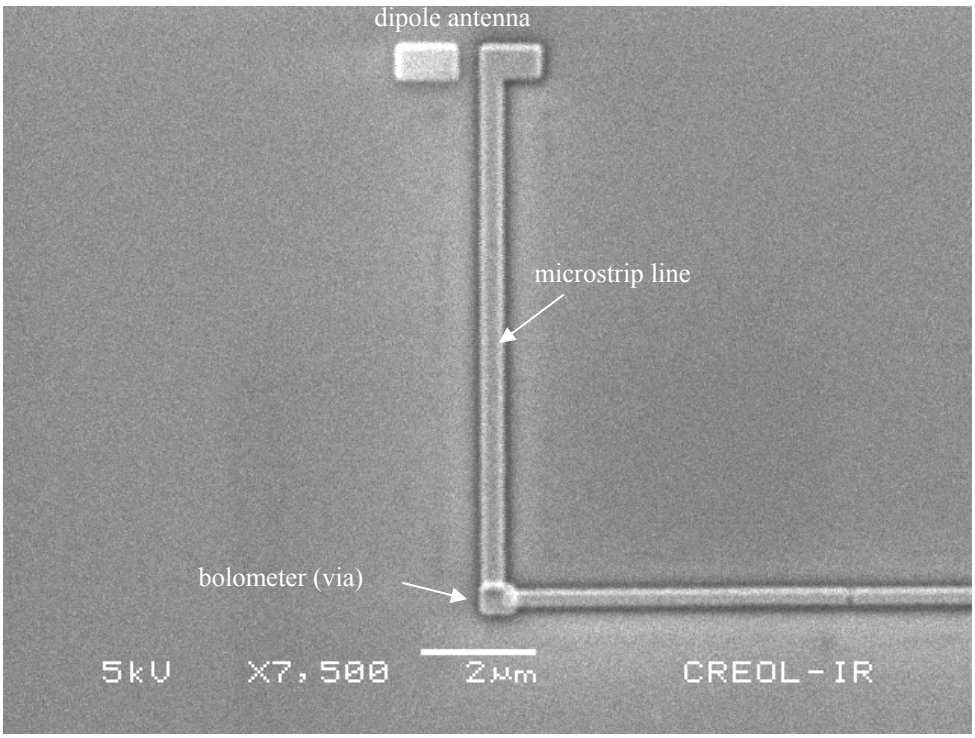

Figure 4.9 Fabricated dipole antenna connected to MS

4.2.2 Experimental results for MS on PECVD SiO_2 standoff layer

We measured the voltage response of the dipole antenna connected to MS lines the of lengths ranging from 1.5 μm to 11 μm in steps of 0.5 μm. The setup for measurement is shown in Figure 3.12; the devices were tested with the CO_2-laser beam at

10.6 μm at both F/8 and F/1. For both the cases the devices were biased with 100 mV. The laser beam was modulated with a chopper at a frequency of 2.5 kHz and the modulated signal produced by the bolometer was read with a lock-in amplifier after a 1000 × preamplification.

In the measurements with F/8 optics the laser was polarized parallel to the dipole antenna and the voltage signal produced by the bolometer was recorded for each length. This data is compared with the modeled current squared computed at the bolometer location and is shown in Figure 4.10. We find that with the increase in length the measured voltage response increases, and this we suspect is due to the response from the dc lead line and bondpads, since the laser diameter at F/8 focus is around 300 μm diameter.

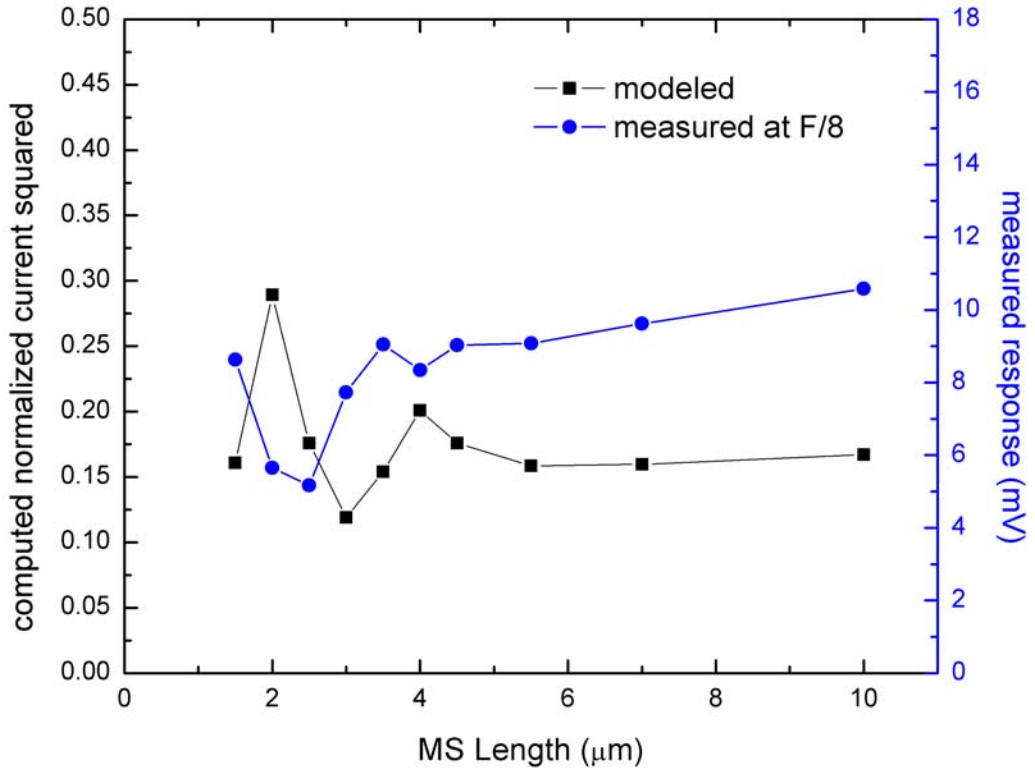

Figure 4.10 Measured versus modeled response at F/8

We then performed another set of measurements using F/1 optics with the laser beam focused to 30 μm spot diameter. A two-dimensional scan was performed on each of these devices in maximum polarization and the convolution between the detector spatial response and the laser beam was obtained (Figure 4.11). Figure 4.12 shows the measured maximum response of detector normalized to incident power as a function of MS length.

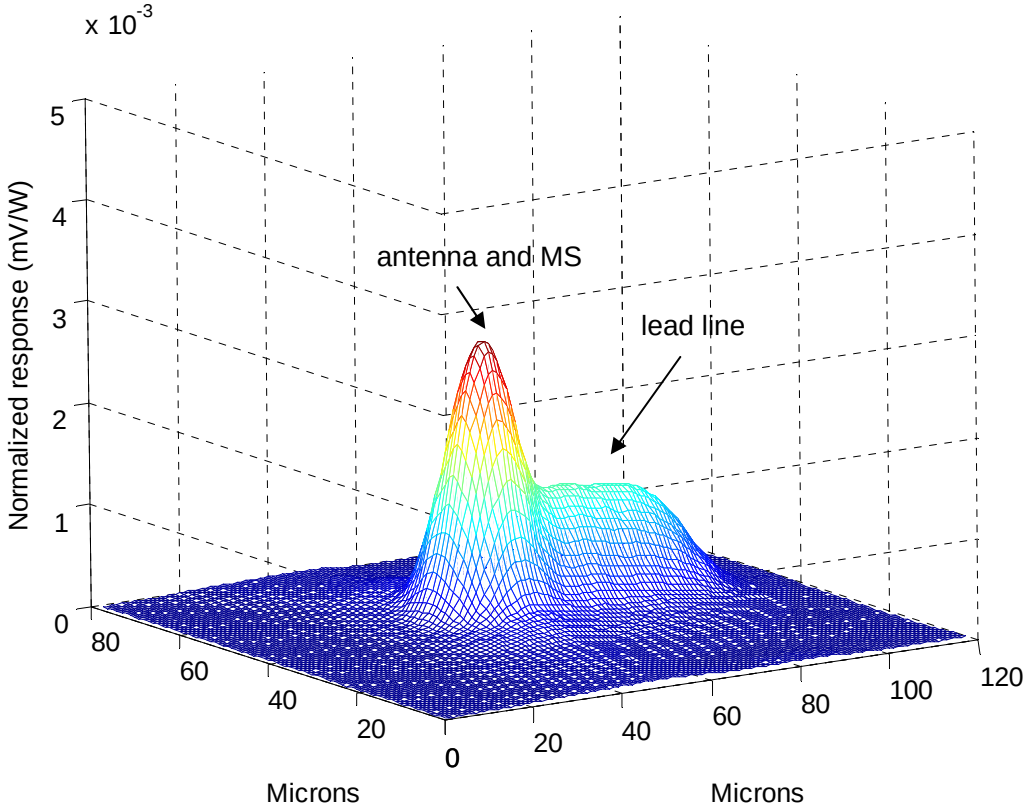

Figure 4.11 2D map for L = 6 μm

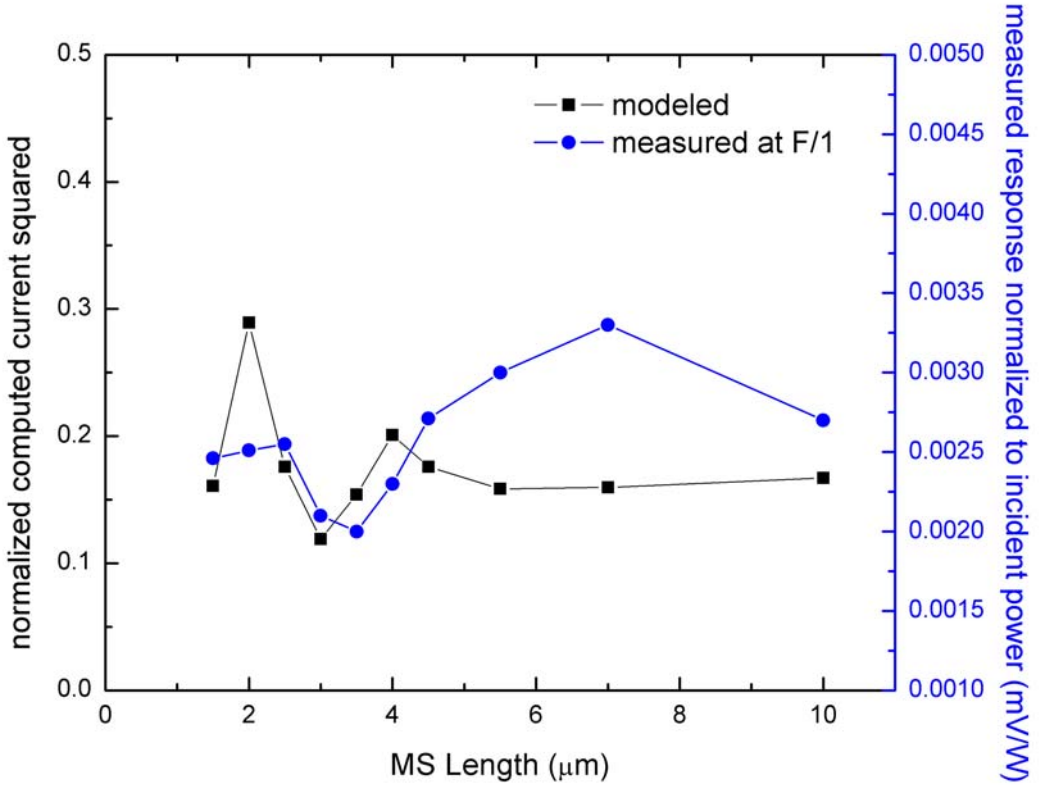

Figure 4.12 Measured versus modeled response at F/1

Both these measurement results were inconclusive since neither F/8 nor F/1 response had consistent behavior in terms of peaks and dips of modeled response. We attribute this "flat" behavior to high losses in the substrate due to which the signal probably died down by the time it reached the bolometer. And so for all the MS lengths that were fabricated, the measured signal was almost constant as if it is fully attenuated.

To solve this problem, we used a ZrO_2 standoff layer, which, from our ellipsometry measurements, had much lower losses compared to PECVD deposited SiO_2 (data shown in Table 2.1).

4.2.3 Fabrication of MS on ZrO_2 standoff layer

We used ZrO_2 as a standoff layer backed by Ni ground plane for fabrication of MS lines. As mentioned earlier in section 4.1.1.2, the etching of ZrO_2 for formation of bolometer (via) was not successful and for this reason the fabrication of MS could not be completed. In this section, we outline our approach implemented for fabrication of MS on ZrO_2 standoff. The design of the device is similar to the one shown in Figure 4.8.

The high resistivity Si wafers (resistivity: 4000-5000 Ω.cm) were coated with 60 nm thick ZrO_2 on top of 200 nm thick Ni. The Ni ground plane and the ZrO_2 were sputter deposited in one single run. Ni was dc sputter deposited using following process parameters: 200 W dc power, 20 sccm Ar, 6.5 mT chamber pressure, 0 platform rotation, giving the deposition rate of 25 nm/rev. ZrO_2 was RF sputtered with following process parameters: 700 W power, 20 sccm Ar, 0.5 sccm O_2 , 6.5 mT chamber pressure, giving the deposition rate of 6 nm/min.

The resist processing for e-beam lithography was done in the same manner as for PECVD SiO_2 as mentioned in Section 4.2.1. The first layer patterned on the above mentioned substrate consisted of alignment marks and one of the two bondpads (bondpad 1 of Figure 4.8). The e-beam exposure parameters are: 120 $\mu C/cm^2$ dose and 25 nA beam current with the e-beam operating at 50 kV. Two step development processes consisted of first developing the exposed ZEP for 30 s in xylene (ZEP RD) and rinsing with IPA and then developing the PMGI for 20 s in TMAH (MF701) and rinsing with DI water. They were metallized with e-beam evaporated Cr-Au (10 nm-150 nm) and the excess metal was lifted-off and the resist was striped off using methylene chloride and EBR PG.

Next step was to etch the ZrO_2 to open a window in ZrO_2 to access the Ni ground plane for signal extraction (bondpad 2, of Figure 4.8) and to form a via which after metallization acts as a bolometer. We used Ti-Ni (20 nm-200 nm) etch mask layer for dry etching ZrO_2. The wafer was coated with e-beam evaporated Ti-Ni (20 nm-200 nm) and e-beam lithography was performed to pattern the bolometer and the bondpad 2. The bolometer and bondpad were exposed using 8 nA and 25 nA beam current respectively and 130 $\mu C/cm^2$ and 120 $\mu C/cm^2$ dose respectively and were developed for 40 s and 15 s in xylene and TMAH solutions respectively. Then the sample was thrown in Ni etchant TFT at 45 C on hot plate with moderate magnetic agitation for 5 min to etch off Ni. It was then immersed in Ti etchant TFG at room temperature for 10 s. This substrate was sent to the Nanofabrication facility at Penn State University for dry etching ZrO_2.

We could not do the fabrication further since the etch process was not successful. If it would have been, the next step was to remove the Ti-Ni etch mask by lifting-off Ti using Ti etch TFG and then to pattern the bolometer for metallization. Finally, the dipole antennas, the microstrip lines and the dc lead lines had to be patterned and metallized.

Since BCB satisfied the criteria of low loss as well as feasibility to etch, we used it next as a standoff layer for MS lines. The type of cyclotene used in this work is the 3000 series advanced electronic resin derived from B-staged benzocyclobutene (BCB) monomers which are dry-etch grades of the cyclotene family of products from Dow Chemical Company. They were developed for use as spin-on dielectric materials in microelectronic fabrication.

4.2.4 Fabrication of MS on BCB standoff layer

We fabricated dipole antenna connected to MS lines of lengths ranging from 0 μm – 11 μm in steps of 1 μm, on 200 nm thick BCB backed by finite ground plane. The device design was similar to one shown in Figure 4.8. These devices were fabricated on high resistivity Si wafers (resistivity: 4000-5000 Ω.-cm). The first layer in fabrication was the finite ground plane, a bondpad connecting the ground plane and alignment marks. These were all made of 200 nm thick Au. The next step was to spin on the cyclotene onto the wafer having the ground plane and markers. Coating the substrate with adhesion promoter is recommended prior to BCB coating. The procedure for applying adhesion promoter on a substrate comprises dispensing, spreading (300 rpm for 5 seconds), and spin-drying (3000 rpm for 15-20 seconds). The BCB was then spin coated and hard baked for 5 min. on hotplate at 250 C in a nitrogen environment. The commercially available cyclotene with lowest viscosity (6022-38 series) gives about 1.2 μm thick film at 5000 rpm. In order to have a thinner film we diluted it using BCB solvent mesitylene (also called 1,3,5-trimethylbenzene). Table 4.1 shows the dilution proportion for corresponding thicknesses for 3000 rpm spin speed.

Table 4.2 BCB thickness for 3000 rpm spin speed

BCB layer thickness	BCB : mesitylene proportion
200 nm	10 gm:20 gm
260 nm	10 gm:15 gm
330 nm	10 gm:11.9 gm

The next step is to etch BCB to form bolometers and to etch open the bondpad connected to ground plane. After spin coating the wafers with BCB and performing the

hard bake, they were coated with bi-layer e-beam sensitive resists: PMGI SF7 and ZEP520A-7 as mentioned in section 4.2.1. The bolometer and the bondpad connecting the ground plane were patterned using e-beam lithography. The bolometer was exposed using 15 nA beam current and the bondpad was exposed using 25 nA beam current with 120 $\mu C/cm^2$ dose for both. The two step development processes consisted of first developing the exposed ZEP for 90 s in xylene (ZEP RD) and rinsing with IPA and then developing the PMGI for 20 s in TMAH (MF701) and rinsing with DI water. The samples were then put in the Plasma Therm RIE system to etch open the windows in the BCB [57], [58]. The following process parameters were used: 50 mT chamber pressure, 10 sccm O_2, 5 sccm CF_4, 100W RF power and 280 V dc bias, giving an etch rate of 150 nm/min. The samples were etched for 2 min to ensure that the BCB is fully etched, all the way down. The resist was striped off using methylene chloride and EBR PG.

Next, the bolometer was patterned once again, for metallization, using the e-beam and development parameters mentioned above. It was metallized using e-beam evaporated 10 nm-200 nm thick Ti-Au.

In the next step, the dipole antenna, microstrip line, lead line and the second bondpad (bondpad 1) were fabricated on top of BCB. The dipole antenna was located above and in the centre of the finite ground plane. The MS was located on the side of one of the dipole arms, towards the center of the dipole. The antenna, MS and lead lines were patterned with 15 nA beam current and a 120 $\mu C/cm^2$ dose, and the bondpad was patterned with 25 nA beam and 120 $\mu C/cm^2$ dose. They were developed in xylene and TMAH for 90 s and 20 s respectively and then metallized with e-beam evaporated Ti-Au (10 nm-150 nm).

4.2.5 Response measurement of MS on BCB standoff layer

The response measurement was performed using the test setup of Fig. 3.12, using the CO_2 laser beam at 10.6 μm focused by an F/1 optical train. The 2D maps were recorded for each device to accurately obtain the response due to antenna and to distinguish between antenna response and the response due to dc lead line (Figure 4.13). The maximum antenna response normalized to power incident on the detector was plotted as a function of MS length Figure 4.14 shows excellent agreement between the measured and computed response, further validating our extracted transmission-line parameters for the BCB standoff layer.

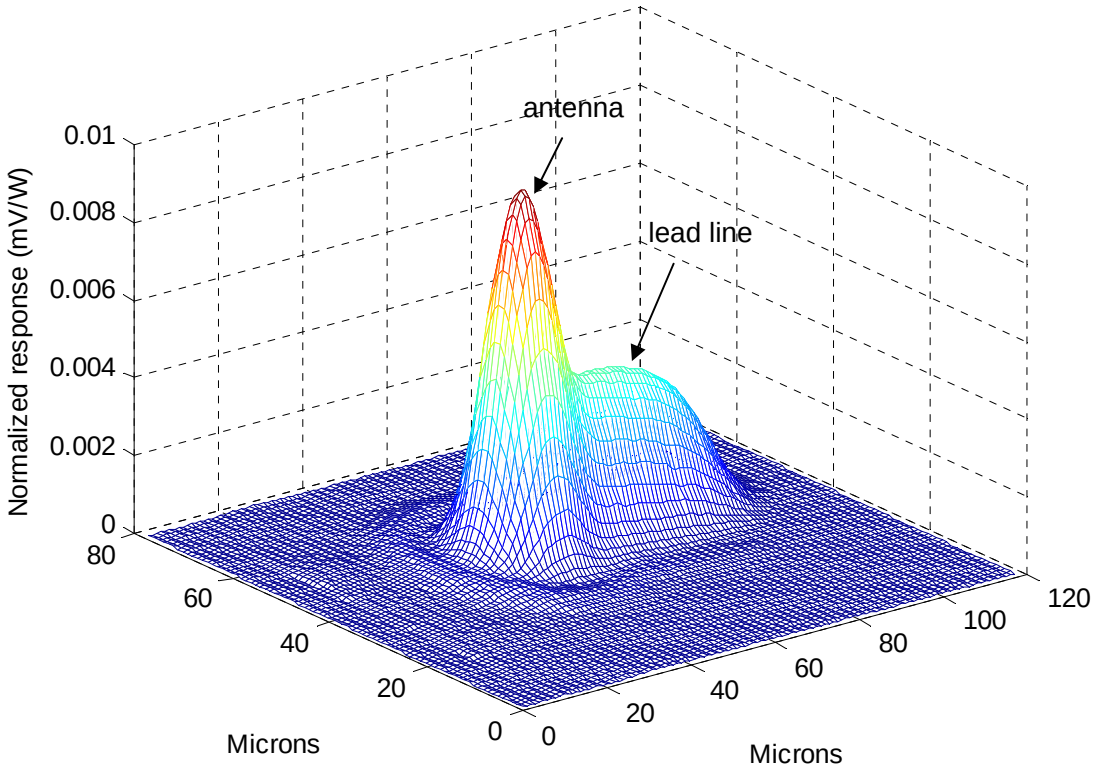

Figure 4.13 Response map for the dipole antenna (MS L = 0 μm)

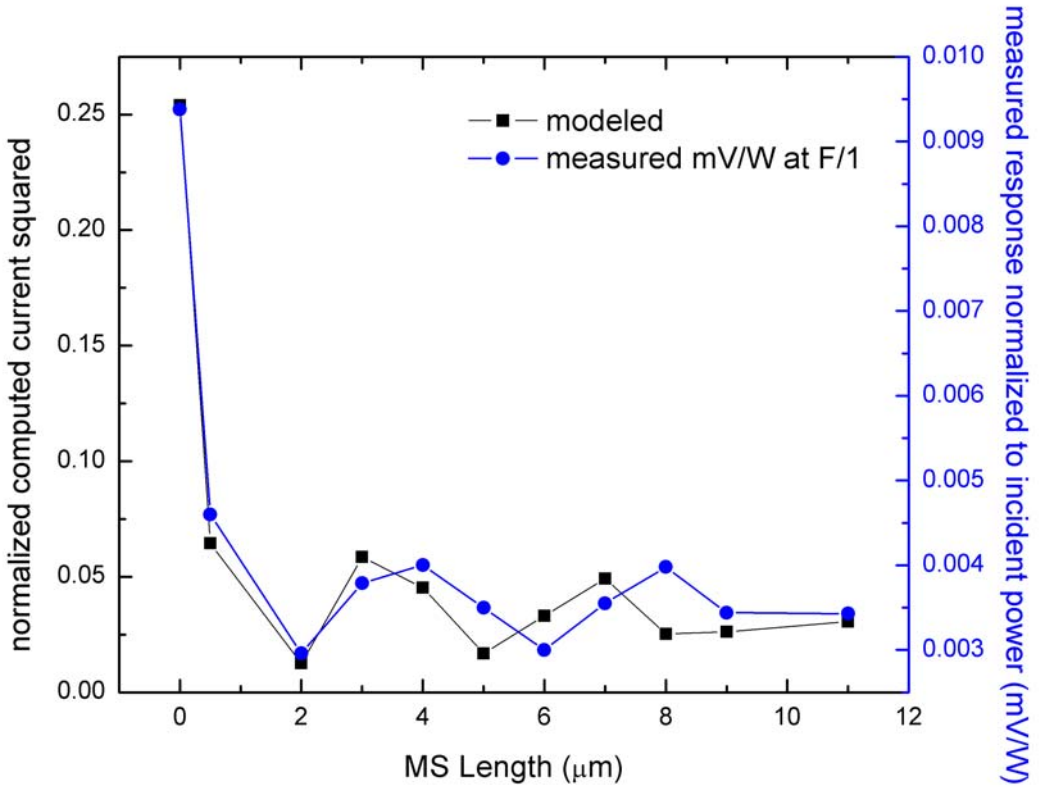

Figure 4.14 Normalized computed versus measured response

To summarize, we modeled the MS lines on three different standoff layers: PECVD SiO_2, ZrO_2 and BCB. From the parameter extraction models, we found that MS lines on BCB produce lowest attenuation. The response measurement of the fabricated dipole antennas connected to MS lines on PECVD SiO_2 rendered the results inconclusive because of higher losses in PECVD SiO_2. We could not fabricate the devices on ZrO_2 because of problems associated with etching it. Finally, we fabricated the dipole antennas connected to MS lines on BCB standoff and the measured response was in excellent agreement with computed response which validated the extracted T-line parameters from our models.

CHAPTER 5 VIA INTERCONNECTION

In this chapter, we present a novel configuration for improving the performance of IR antennas. In this configuration, the antenna is connected to the bondpads through via interconnect which runs vertically down through two isolation layers of SiO_2 and through a ground plane. This configuration not only separates the bondpad plane away from the antenna such that the bondpads are electrically isolated from the antenna at IR frequencies, but also reduces the pixel size in a focal plane array configuration. Our simulation results show that this configuration improves the performance of antenna as compared to the case where bondpads are on the antenna plane. A detailed fabrication process is described.

Figure 5.1 shows the configuration of a dipole antenna connected to the bondpads through vias which run vertically down through two isolation layers of SiO_2 and through a ground plane. Through modeling, we show that device performance can be improved using this configuration. Vias also provide access to feed-point geometries in designs such as spirals where the design geometry prohibits coplanar interconnects. The fabricated dipole antenna is designed to be illuminated from the substrate side and works as a receiving antenna.

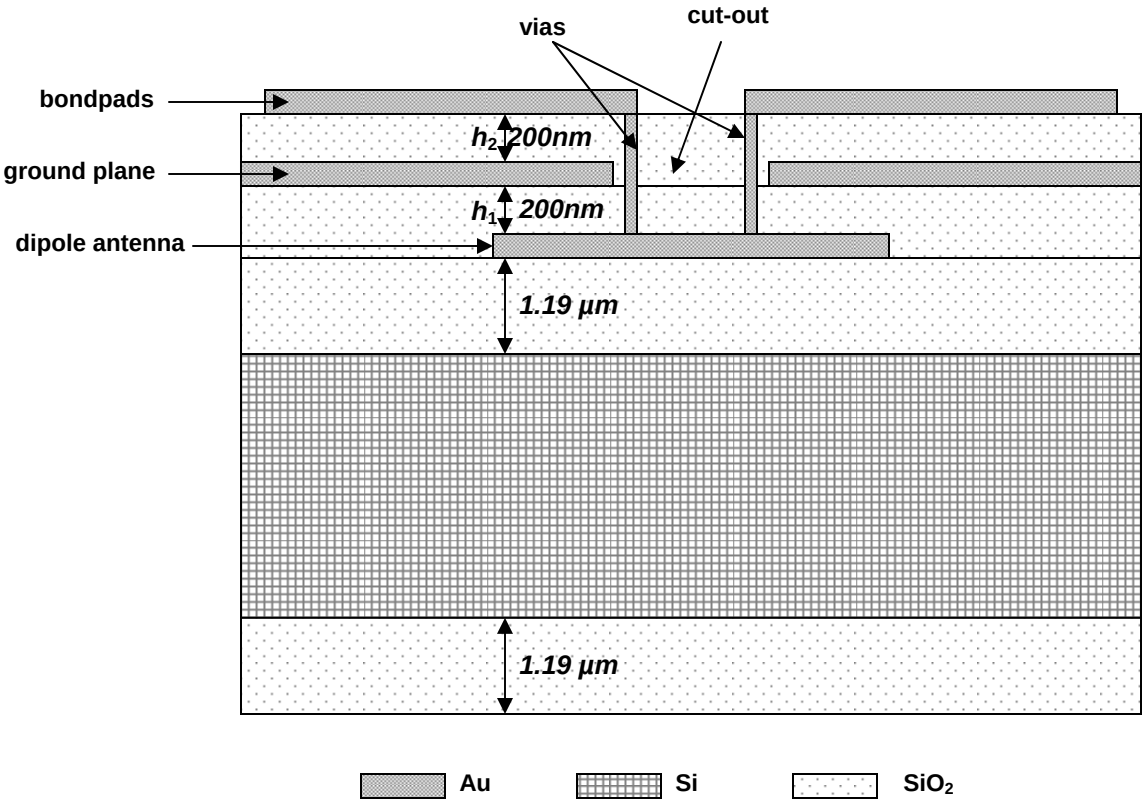

Figure 5.1 Device configuration (cross-sectional view)

5.1 Effect of bondpads on antenna response

We have modeled three antenna designs with different bondpad configurations in order to understand the effect of bondpad on antenna response. The three cases considered are: 1) a dipole antenna on 200 nm thick SiO_2 substrate backed by ground plane, 2) a dipole antenna directly connected to bondpads [16], on 500 nm thick SiO_2 substrate backed by ground plane, with the bondpads on the same plane as shown in Figure 5.2 (a) and (b), and 3) a dipole antenna connected to bondpads through vias as shown in Figure 5.1. For case 1), we compute the input impedance at the antenna feed point to find the first and second resonances based on zero crossings of imaginary part of impedance Im(Z). Figure 5.3 shows that the first dipole resonance corresponds

approximately to a minimum of the real part of impedance Re(Z) which occurs when the dipole length is 2 μm. The second resonance, also referred to as an anti-resonance, corresponds to very high Re(Z) and occurs at a 4 μm dipole length. The antenna response is strongest for dipole length corresponding to first resonance and weakest corresponding to the second resonance.

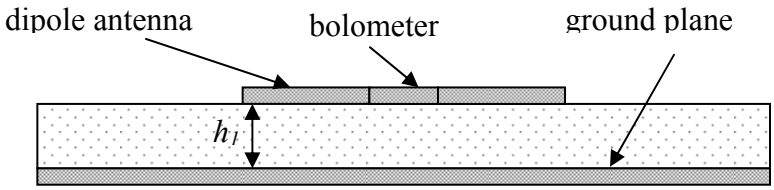

(a)

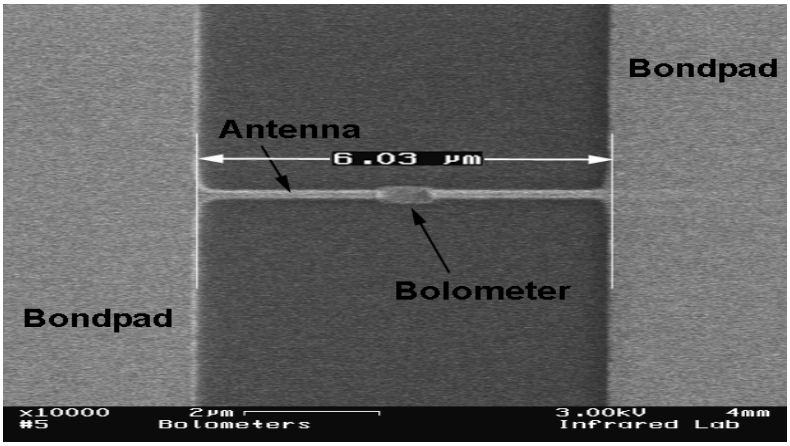

(b)

Figure 5.2 Antenna designs used to study the effects of bondpads: (a) dipole antenna on grounded SiO_2, (b) dipole antenna from [16]

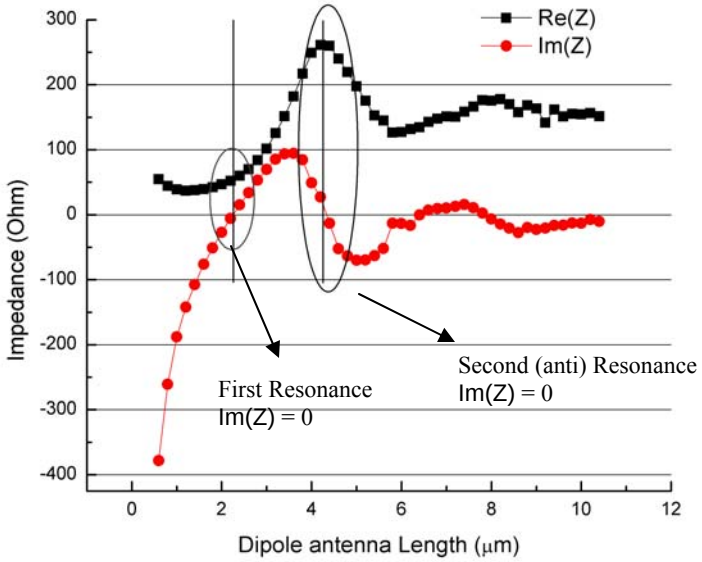

Figure 5.3 Dipole feed point impedance as a function of antenna length

For the three cases considered, we compute and compare the antenna response (square of current at the feed point). Figure 5.4 shows the normalized response for these three cases. We find that the antenna directly connected to bondpad has a weakest response corresponding to first resonance length and strong response corresponding to second resonance – opposite to the ideal case. But with the design of Figure 5.1 the bondpads are electrically isolated due to the presence of ground plane between the antenna and bondpads and hence the response is similar to the ideal case of antenna without the bondpads.

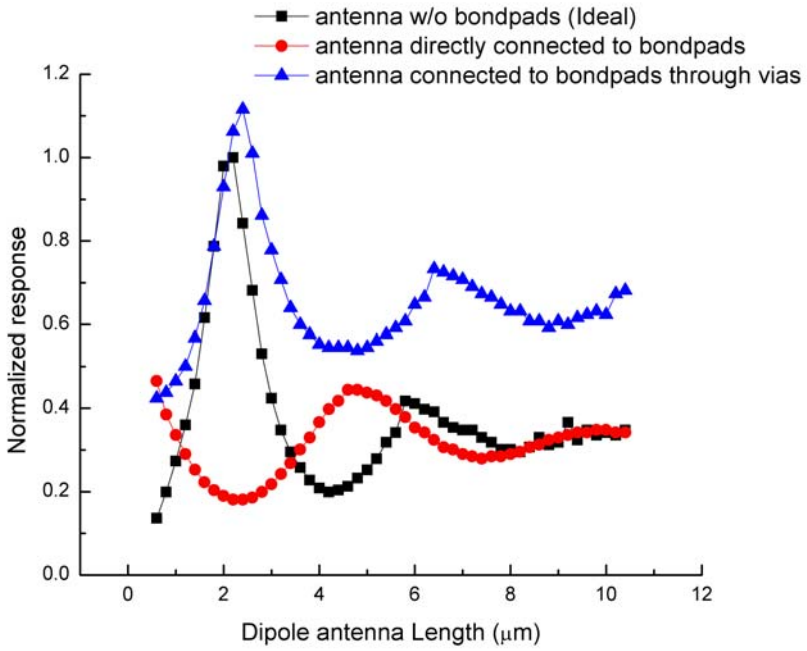

Figure 5.4 Computed normalized response for the three cases

This result has motivated the study of vias for improved device performance by eliminating the undesirable effects of bondpads.

5.2 Modeling for via optimization

We calculated the power dissipated in the bolometer for device design and optimization. Dissipated power is the parameter of interest since it is an indication of device response. As the bolometer is located at the center of the device, maximum power is supposed to be dissipated in it. We calculated the dissipated power in the bolometer using following expression:

$$P_{dissipated} = \sigma \int |E|^2 \, dV \qquad \textbf{5.1}$$

where σ is the metal conductivity, E is the electric field in the region of integration and V is the volume of integration.

We modeled a gold dipole antenna (3.4 μm long and 0.6 μm wide) on SiO_2 layer backed by Au ground plane as shown in Figure 5.5. A gold bolometer 0.4 μm × 0.6 μm was used. The material parameters for all materials were measured from IR-VASE and are listed in Table 2.1. The dipole was excited using a plane wave excitation with E-field polarized along the length of dipole and having the magnitude of 1 V/m. We studied the effects of two parameters: the size of the cut-out in ground plane and the location of bolometer along the via height, as discussed in the following sections.

5.2.1 Cut-out size in the ground plane

The cut-outs are made in the ground plane in order to avoid the shorting of vias to the ground plane. The cut-out size is a μm × b μm as shown in Figures 5.5 and 5.6.

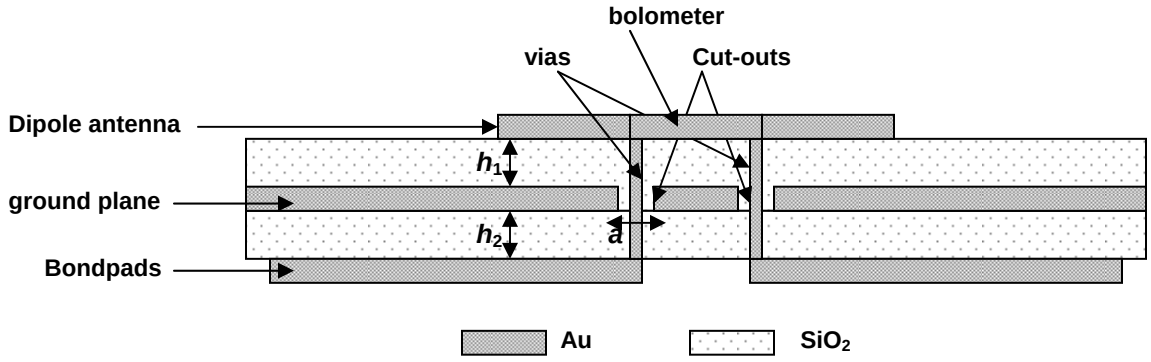

Figure 5.5 Cross-sectional view of model to study the effect of size of cut-out in ground plane

We studied the effect of the size of cut-out, a, (keeping b constant = 0.2 μm) on device response by computing the power dissipated in bolometer and antenna arm as a

function of '*a*' (varying from 0 μm to 0.55 μm) for the via cross-section of 100 nm × 100 nm, and for bigger cut-outs (a = 1.2 μm and 1.6 μm, b = 0.6 μm) for via cross-section of 300 nm × 300 nm. The calculated powers were almost constant as shown in Figure 5.7. We find that the size of cut-outs under consideration does not considerably affect the power dissipated in bolometer and antenna arm, and hence the response. Hence for the fabricated device, we use a single cut-out of size 1.5 μm × 0.6 μm for the two vias.

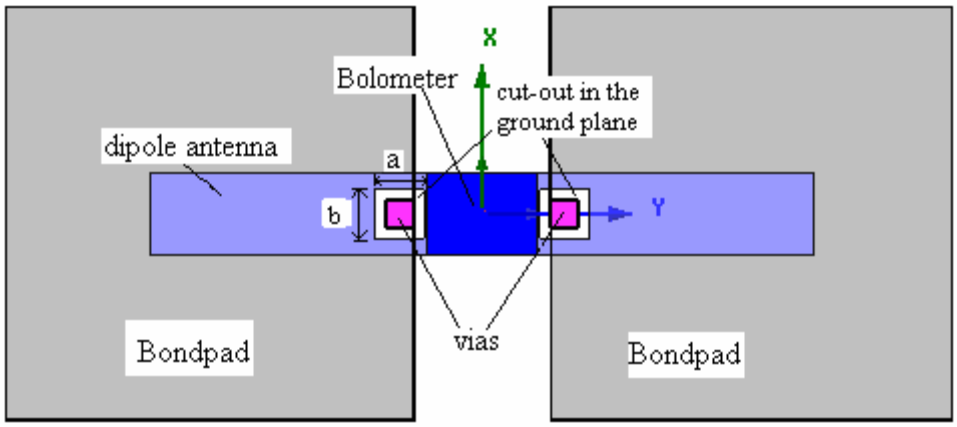

Figure 5.6 Top view of model for optimizing cut-out size

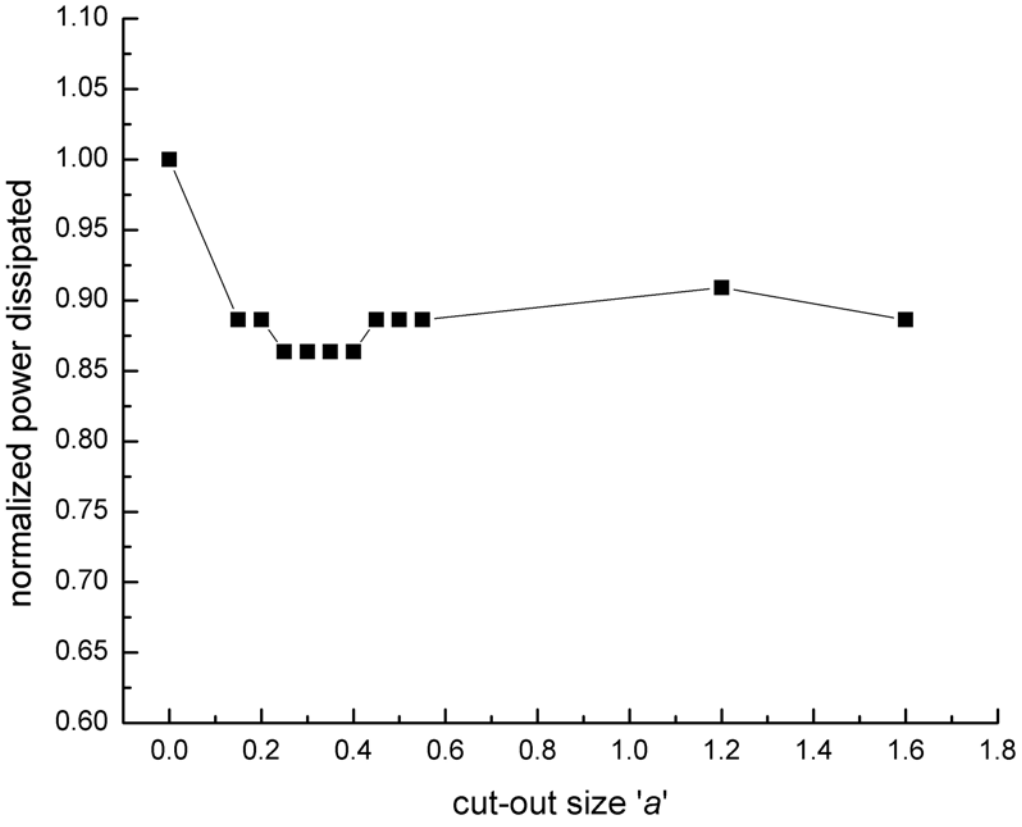

Figure 5.7 Computed power dissipated as a function of size of the cut-out in ground plane

5.2.2 Characterization of vias at infrared frequencies

The model of Figure 5.5 is such that dc current propagates along the vias down to the bondpads. We modified this model so that IR frequency current waves propagate along some portion of the vias. This is done by varying the location of bolometer along the via height as shown in Figure 5.8. The distance *D* is the location of bolometer with respect to the antenna plane, and that is the height of via through which IR current

propagates. In this model, h_1 and h_2 are fixed at 500 nm. We compute the power dissipated in the bolometer as a function of distance D, as shown in Figure 5.9.

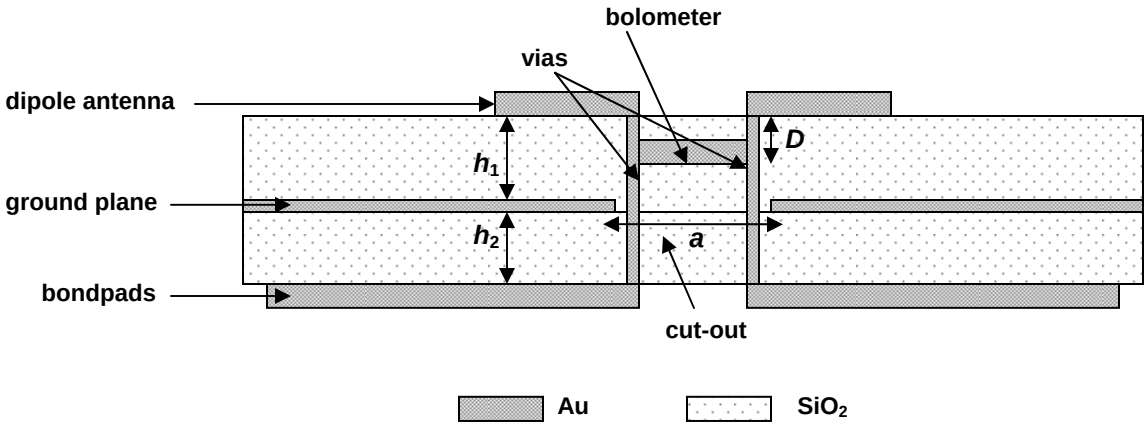

Figure 5.8 Cross-sectional view of model for optimizing bolometer location

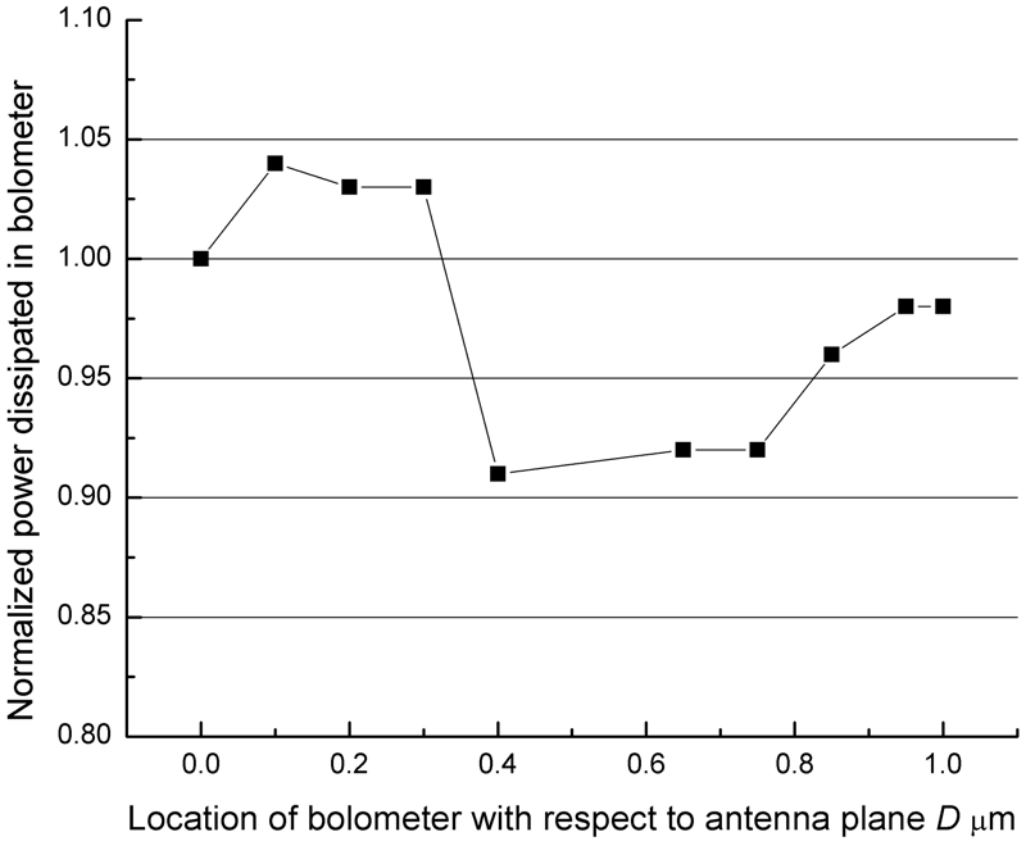

Figure 5.9 Computed power dissipated in bolometer as a function of bolometer location D μm

Figure 5.9 shows that higher response is obtained if the location of bolometer is closer to antenna plane such that only a small portion of vias carry IR current waves. Also when the bolometer is closest to the ground plane, the response drops. Hence, we choose to fabricate the bolometer at the antenna plane (D = 0 μm) as in Figure 5.1 such that no IR frequency currents propagate along the vias.

5.4 Fabrication

We fabricated the dipole antenna connected to bondpads with vias through two isolation layers and through a ground plane, as shown in Figure 5.1, in two steps. The first step was to fabricate vias through one isolation layer of SiO_2 to demonstrate the feasibility of via fabrication. We achieved this by fabricating a dipole antenna connected to bondpads through vias etched in the SiO_2 layer which separated the antenna and bondpads, as shown in Figure 5.10. The next step was to actually fabricate the device shown in Figure 5.1.

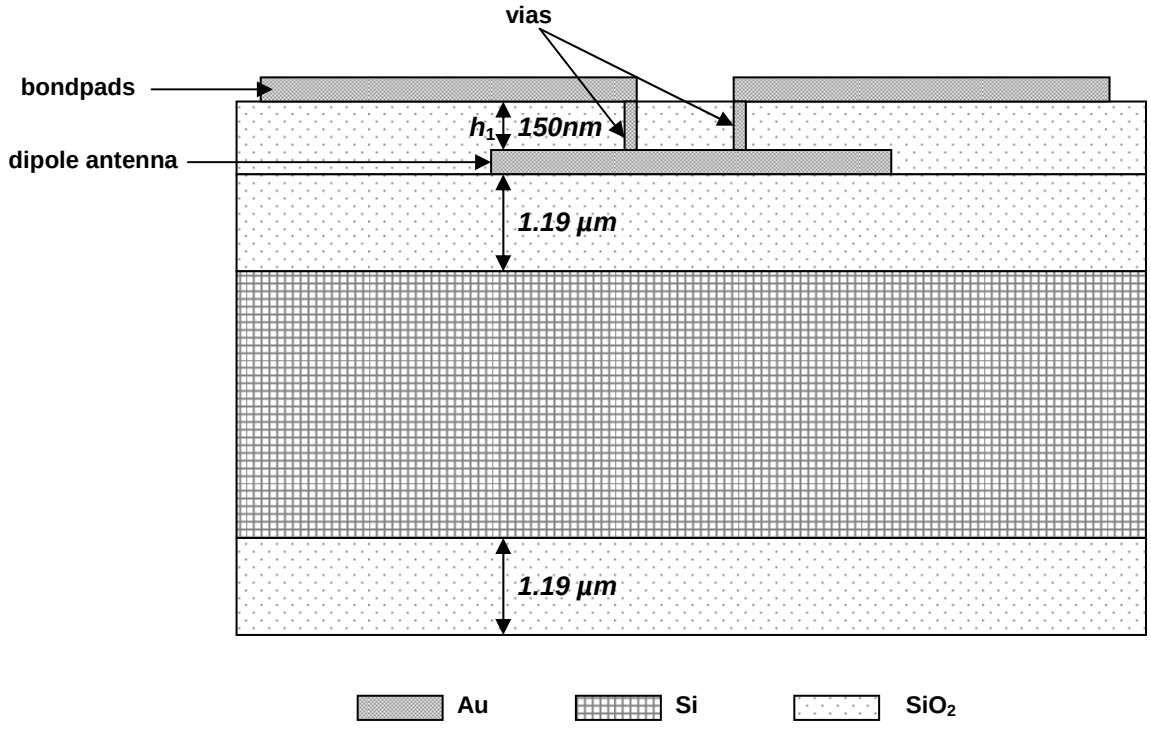

Figure 5.10 Cross-sectional view of device with vias through one isolation layer

The substrate used for these devices was low resistivity Si wafer with thermally grown 1.19 µm thick SiO_2 on either side. Prior to coating the wafer with e-beam sensitive

resist, the wafer was spin rinsed at 4000 rpm, for 60 s , with acetone, methanol and isopropanol and then dehydration baked for 3 min at 180 C on a hot plate. The resist used was a bilayer consisting of PMGI SF7 and ZEP520A-7. First, PMGI SF7 was spun at 300 rpm-700 rpm-3000 rpm for 15 s-5 s-80 s followed by 3 min softbake at 180 C, resulting into 250 nm thick film. ZEP520A-7 was spun next at 300 rpm-700 rpm-3000 rpm for 15 s-5 s-80 s also and softbaked for 4 min at 180C, giving 250 nm thick film. This resist coating recipe was used for patterning all device features except for vias and finite ground plane. A thicker resist layer was used for the vias since the resist was used as etch mask for etching SiO_2 first and then the resist left over after the etch process had to undergo metal liftoff right after that. Thus the etching and metallization of vias required one lithography step only. For this case PMGI SF5 (5% dilution compared to 7% in SF7 used earlier) was spun at 300 rpm-700 rpm-3000 rpm for 15 s-5 s-80 s followed by a 3 min softbake at 180 C giving 330 nm thick layer and ZEP520A was spun at 300 rpm-1800 rpm for 15 s-60 s followed by 4 min softbake at 180 C resulting into 555 nm thick film. For patterning the ground plane, a single layer of ZEP520A-7 was spun using the above recipe.

The patterning was done with Leica EBPG5000+ system operating at 50kV. A dipole antenna, of dimensions 3.4 μm × 0.6 μm, was designed to resonate on the substrate of Figure 5.10 for resonance at 10.6 μm wavelength. The device was patterned and metallized first along with 4 sets of 20 μm × 20 μm alignment marks. They were written with a dose of 125 $\mu C/cm^2$ and 8 nA beam and developed in xylene (ZEP RD) for 90 s and rinsed with IPA, followed by 20 s development in TMAH (MF701) and rinsing with DI water. It was then metallized with Au using e-beam evaporation technique.

The SiO_2 layer (150 nm thick) was then deposited over the substrate using PECVD with the following process parameters giving a deposition rate of 50 nm/min: 1050 mTorr pressure, 400 sccm SiH_4, 827 sccm NO_2, and 25 W RF power. Two 300 nm × 300 nm size square features were patterned (to form the via interconnect), with a dose of 145 $\mu C/cm^2$ and 8 nA beam current and developed in ZEP RD for 40 s followed by 10 s MF701 development. Next, silicon dioxide in the patterned features was etched using RIE with the following process parameters giving an etch rate of 50nm/min: 75 mTorr pressure, 5 sccm O_2, 45 sccm CF_4, and 175W RF power. The etched holes were then metallized with Au using e-beam evaporation.

For the device of Figure 5.10, the next step was to pattern and metallize the bondpads (250 μm × 250 μm). The bondpads were written with a dose of 135 $\mu C/cm^2$ and a beam current of 25 nA and were developed for 30 s ZEP RD followed by 20 s MF701 and then metallized. Figure 5.11 shows the SEM photo of the fabricated device. The dc resistance was measured between the two bondpads to confirm that the vias went all the way through SiO_2 and were electrically connected to the dipole antenna. The measured dc resistance across the two bondpads was between 8-10 Ω and this confirmed continuity of the vias.

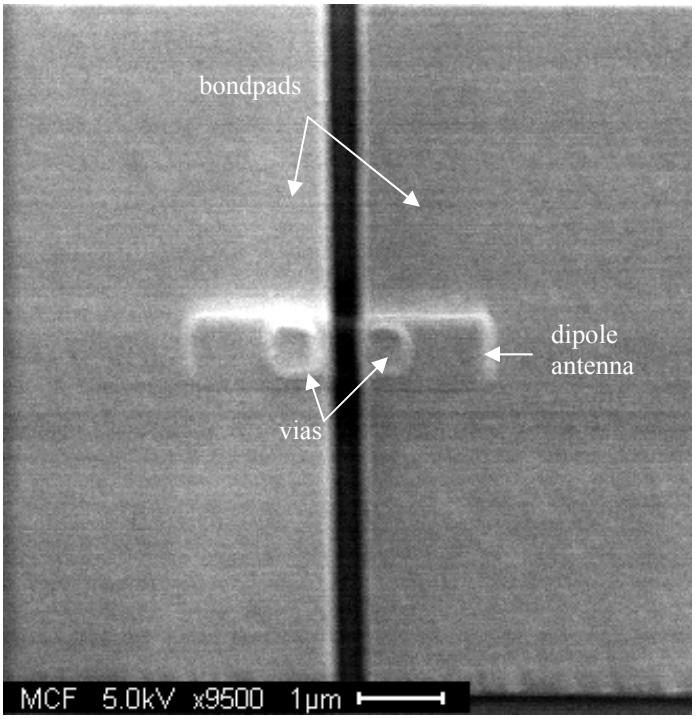

Figure 5.11 Fabricated dipole antenna with via through one isolation layer (top view)

For the device of Figure 5.1, the next step after fabricating the vias through the SiO_2 layer was to pattern the ground plane (250 μm × 250 μm) with cut-out (1.5 μm × 0.6 μm). The ground plane consisted of two parts, a small 10 μm × 10 μm inner square containing the cut-out and a big outer annular square. Both structures were patterned at the same time but with different doses and currents. The small, 10 μm x 10 μm, inner piece of finite ground plane, including cut-out was written using the dose of 75 $\mu C/cm^2$, 8 nA beam current and larger outer piece was written using 140 $\mu C/cm^2$ and 25 nA beam current. They were developed for 30 s in ZEP RD. The finite ground plane was metallized so that it had Ti adhesion layer both on the top as well as on the bottom of 150 nm Au film to ensure adhesion to the SiO_2 to be deposited on top of ground plane. The device at this stage is shown in Figure 5.12.

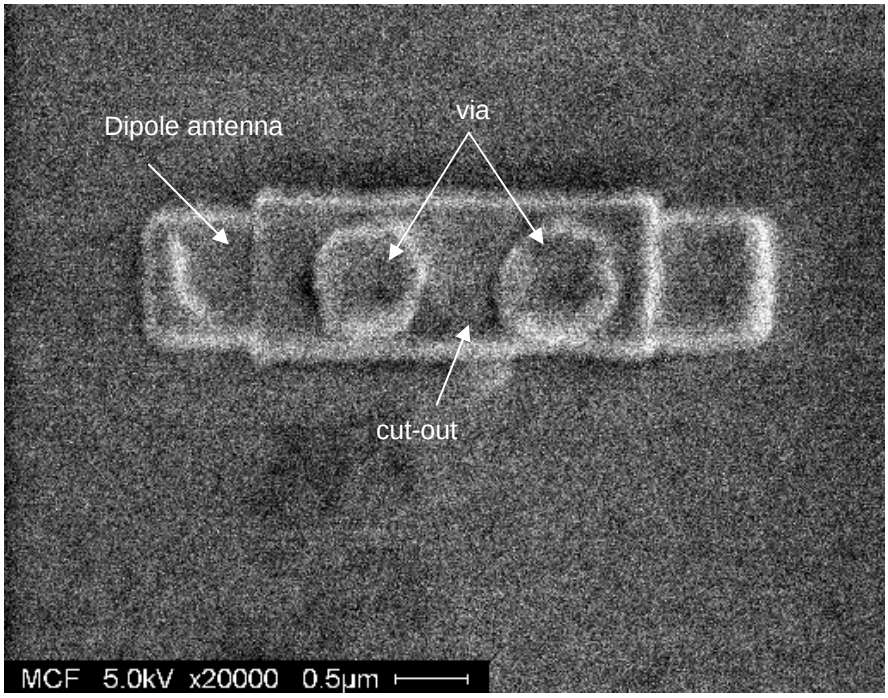

Figure 5.12 Fabricated ground plane and cutout aligned to vias (1st layer)

Next, another 150 nm thick layer of SiO_2 was deposited using the same process mentioned above and then the vias (300 nm × 300 nm) were patterned, etched and metallized. Figure 5.13 presents the top view of the fabricated device at this point. Finally bondpads (250 µm × 250 µm) were patterned and metallized. The detailed step by step fabrication procedure is shown in Fig. 5.14. To see the cross-section of the device, a portion of substrate near the device was cut using focused ion beam (FIB) FEI 200TEM having 30 kV Ga ion source and the cross-sectional view of the fabricated device is shown in Figure 5.15.

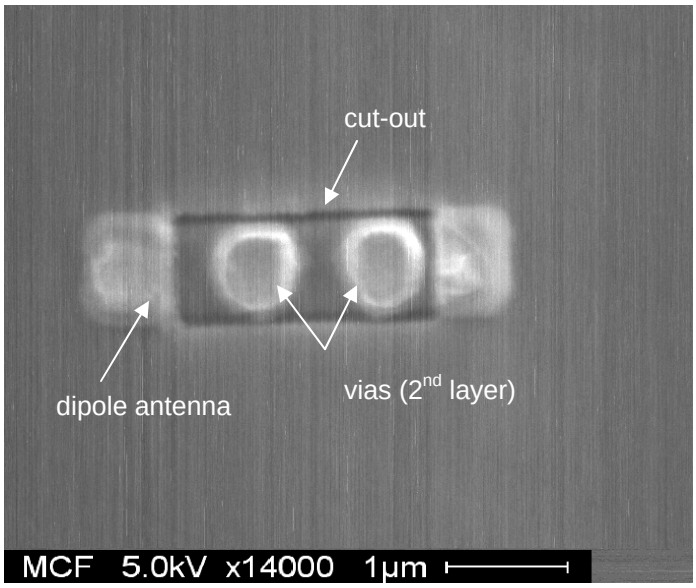

Figure.5.13 Fabricated 2nd layer vias aligned to cutout and ground plane

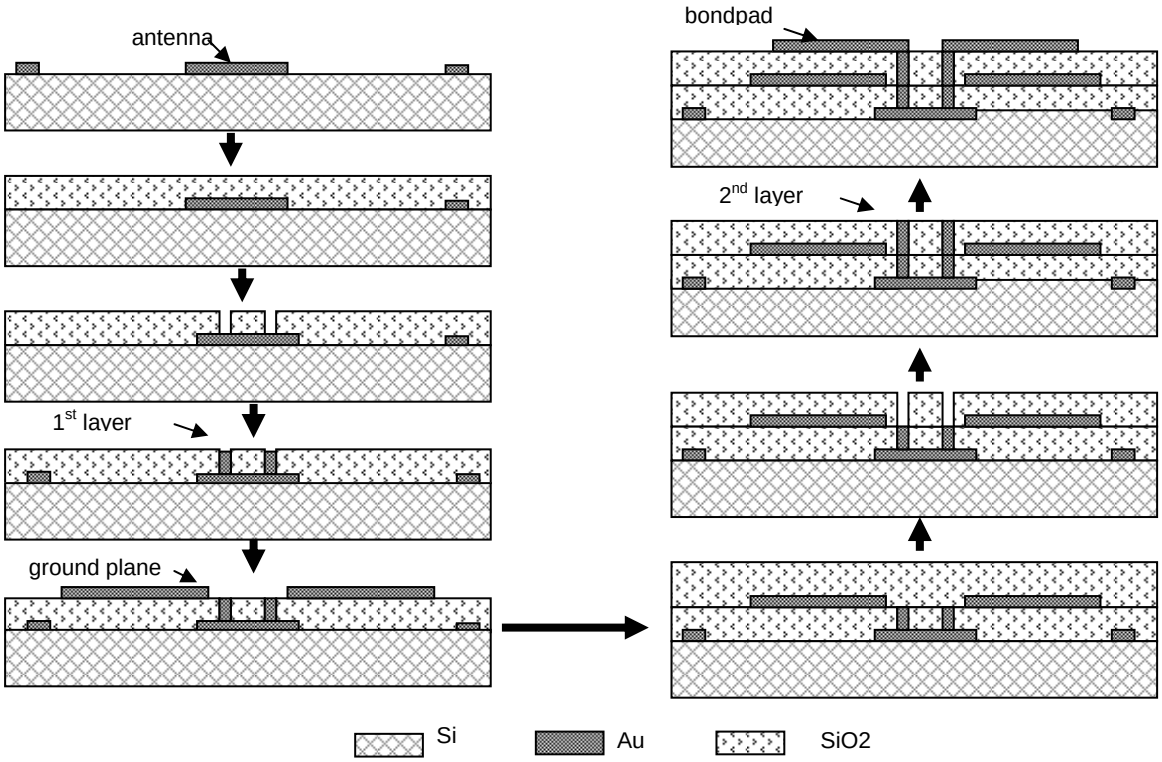

Figure 5.14 Details of fabrication process

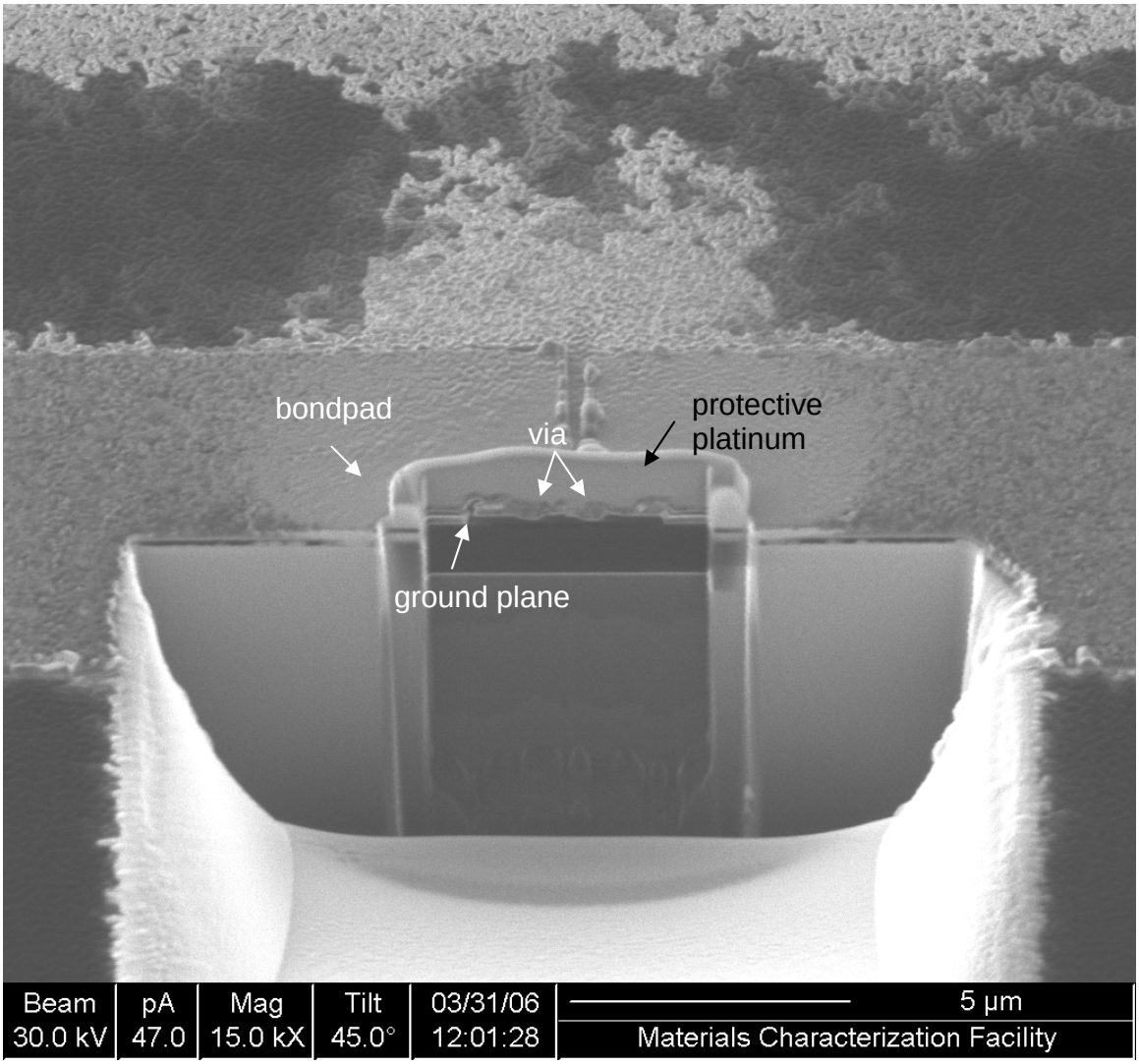

Figure 5.15 FIB cross-section of the device

We measured the response of this device with substrate side illumination using F/1 optics. A 2D map of the response was obtained with a scan step size of 1 µm. The 2D map shows only one peak which indicates that the bondpads were electrically isolated. The measured 2D map is shown in Figure 5.16.

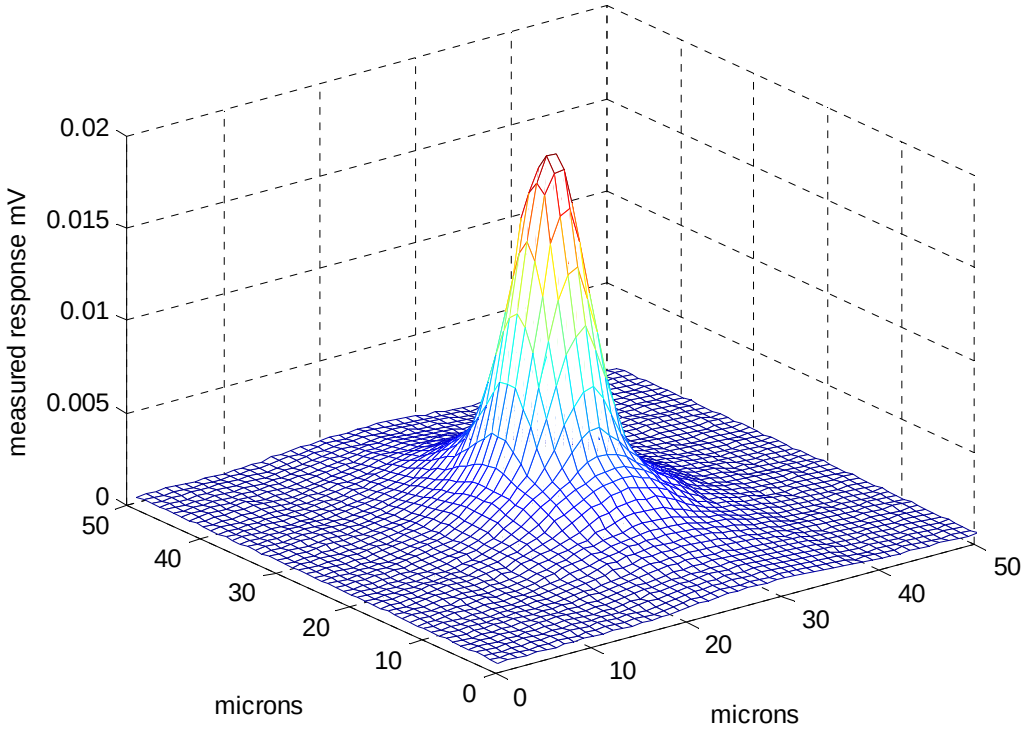

Figure 5.16 Measured 2D map of fabricated device

Hence, we show the feasibility of fabricating vias through two isolation layers and through a ground plane and the measured response verifies the electromagnetic isolation of the antenna from bondpad.

CHAPTER 6 CONCLUSION

In this dissertation, we have demonstrated the first LWIR wire transmission-line design and fabrication in conjunction with infrared detectors. We extracted the transmission-line parameters for CPS and MS types of transmission-lines by parametrically analyzing our models. We used Ansoft HFSS, which is based on finite element method, for modeling these transmission-lines. Actual materials are used in the model, the material properties of which are measured from IR-VASE. Our procedure is based on parametric analysis of the transmission-line as a function of its length. From full wave field solutions, we compute the impedance at a defined port which is based on the reflected and transmitted fields at the port. This approach does not involve the use of analytical equations for computing transmission-line parameters, and hence, is a valid approach at LWIR. The transmission-line parameters cannot be measured directly, so in order to verify the extracted transmission-line parameters, we model, measure and compare the response of a dipole antenna, resonating at 10.6 μm, connected to the transmission-line, as a function of transmission-line length, for both types of transmission lines. The measured voltage response is proportional to the I^2R power dissipated in the bolometer (where I is the current and R is the resistance of bolometer) and we compare this quantity with the current squared at the bolometer (port) computed from our model. This current depends on the impedance at bolometer (port) location which, in turn, is the impedance of the dipole antenna transformed along the transmission-line length based on transmission-line parameters and hence directly related to the extracted Z_o, n_{eff} and α of that particular design. Hence, the agreement between measured and modeled responses validate the extracted transmission-line parameters for both types of transmission lines.

The devices were fabricated using e-beam lithography. The measurements were performed with the CO_2-laser beam at 10.6-μm emission focused by an F/1 optical train. The bolometer under test was biased at 100 mV. A 2D map of the response of the antenna was obtained and the maximum antenna response normalized to incident power was plotted as a function of CPS and MS length. For both the transmission-lines our modeled response was in good agreement with measured response validating the extracted transmission-line parameters for both the cases.

We have also studied the vertical via as another type of interconnection for IR antennas. With vias, we present a novel configuration for improving the performance of IR antennas. In this configuration, the antenna is connected to the bondpads through vias which run vertically down through two isolation layers of SiO_2 and through a ground plane. This configuration not only separates the bondpad plane away from antenna such that the bondpads are electrically isolated from antenna at IR frequency, but also reduces the pixel size if applied in FPA configuration. Our simulation results show that this configuration improves the performance of antenna as compared to the case where bondpads are on the antenna plane.

APPENDIX:

2D MAPS – RESPONSE DUE TO BONDPADS AND LEAD LINES

The antenna response map was obtained using the test setup of Figure 3.12 with linear polarization state that produced the strongest signal for both CPS and MS structures. We find that as the length of transmission line increases, the antenna response decreases because of the increasing attenuation along the transmission line. At the same time the response from the lead line (for MS devices)/bondpad (for CPS devices) is higher than the antenna response for longer transmission line lengths. One possible reason for this could be the thermal response of the detector. Also, the magnitude of response due to lead lines and bondpads varied from device to device. The 2D maps of some MS and CPS devices are shown in Figures A1 – A4.

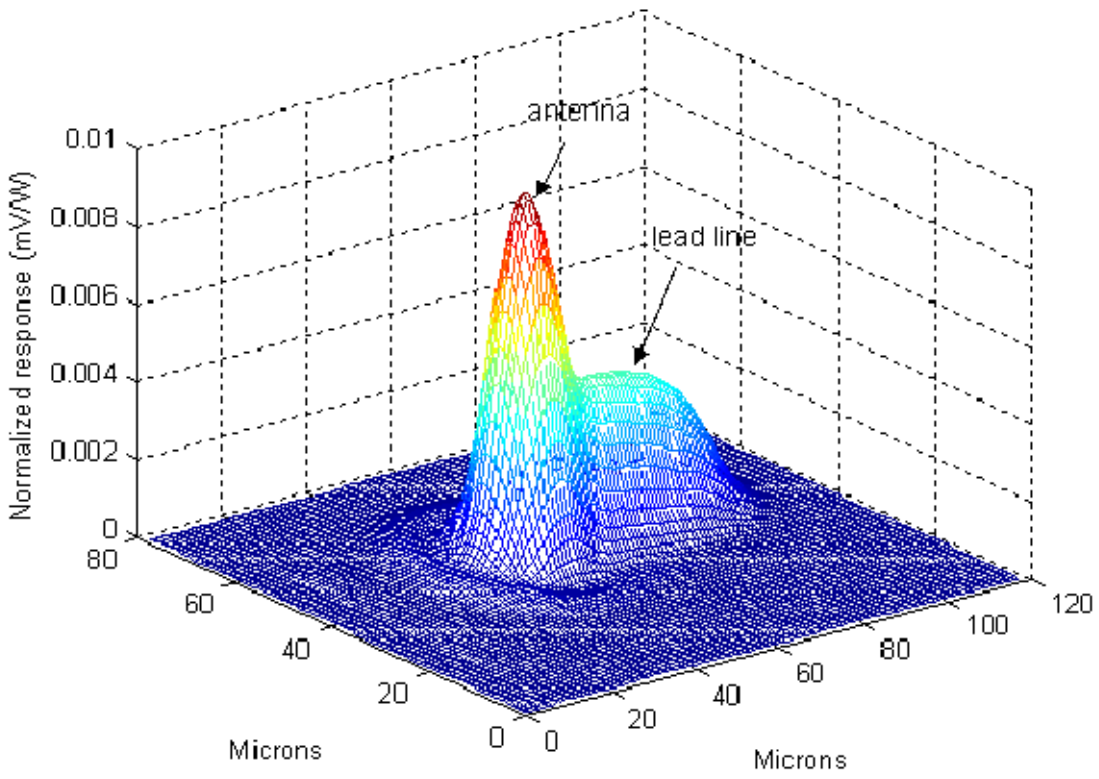

Figure A1 2D map of antenna response for (a) MS L = 0 μm (dipole only)

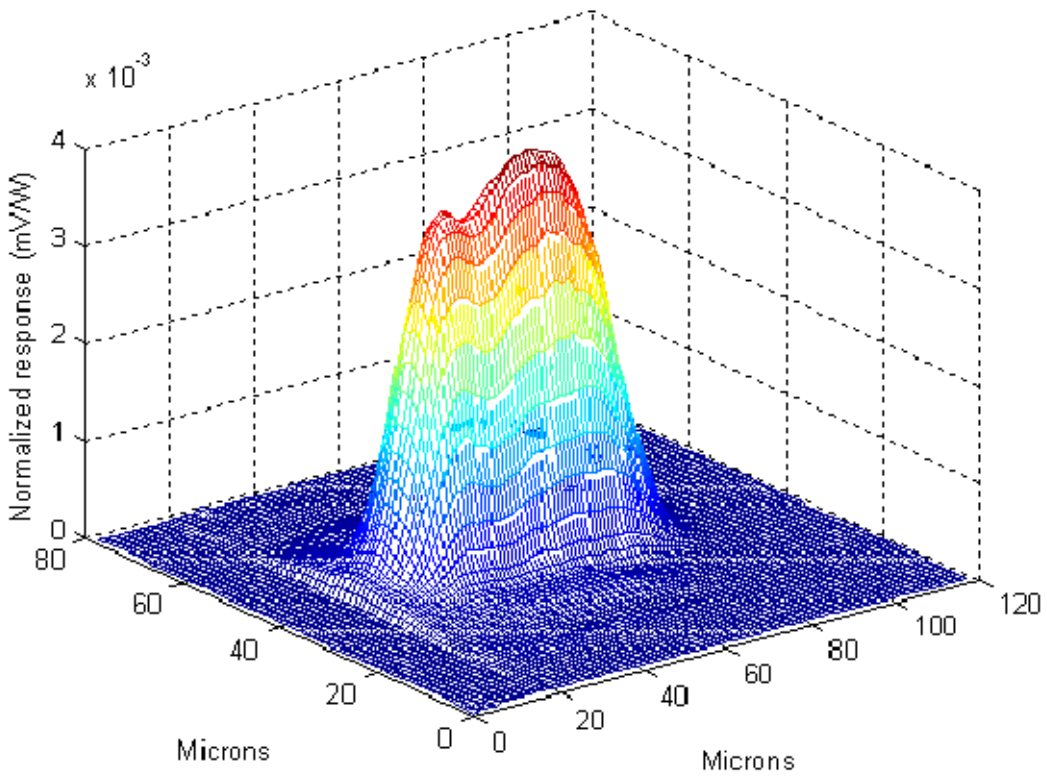

Figure A2 2D map of antenna response for (a) MS L = 5 μm

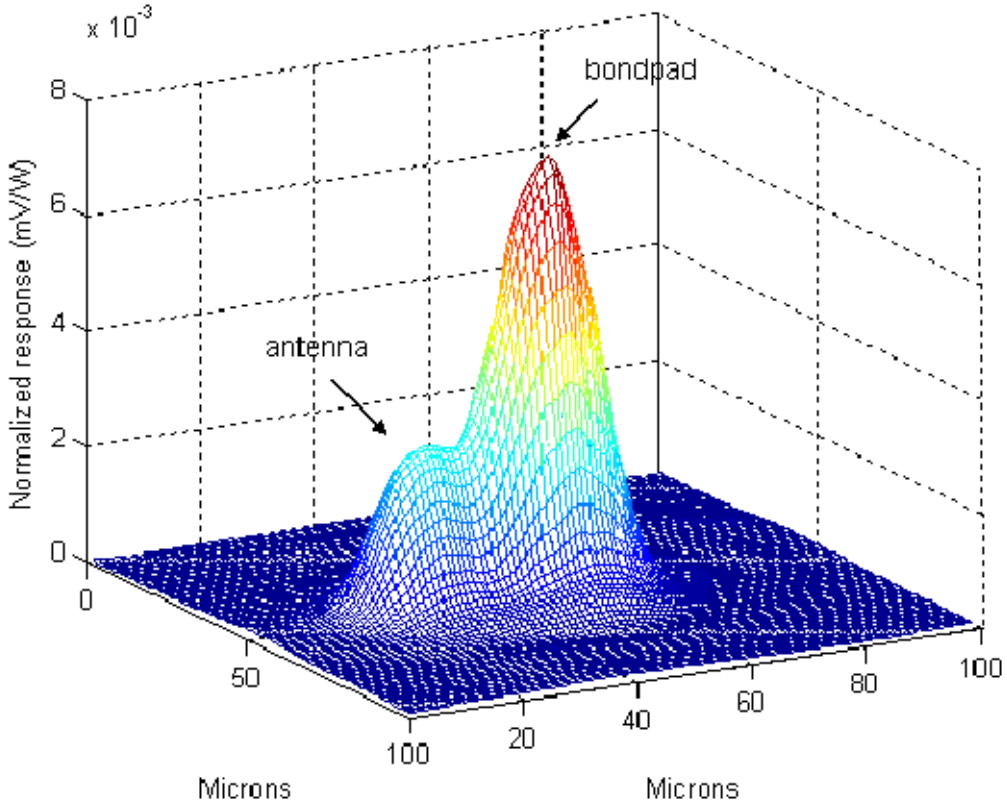

Figure A3. 2D map of antenna response for (a) CPS L = 8 µm

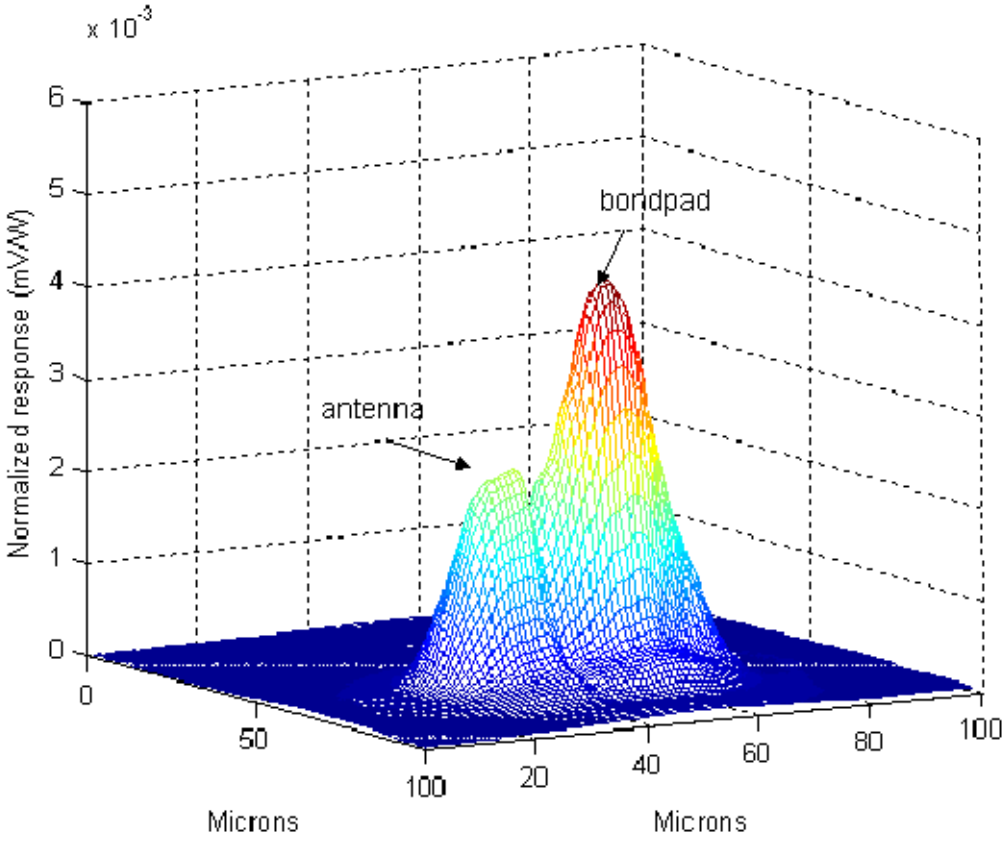

Figure A4. 2D map of antenna response for (a) CPS L = 11 μm

LIST OF REFERENCES

[1] F.J. González, M. Abdel-Rahman, G. D. Boreman, Antenna-coupled VOx thin-film microbolometer array,*Microwave and Optical Technology Letters* 38(3): 235-237, 2003.

[2] E.L. Dereniak and G.D. Boreman, *Infrared Detectors and Systems*. John Wiley & Sons, Inc, 1996.

[3] L.O. Hocker, D.R. Sokoloff, V. Daneu, A. Szoke, A. Javan. Frequency mixing in the infrared and far-infrared using a metal-oxide-metal point contact diode. *Applied Physics Letters,* 12(12): 401-402, 1968.

[4] J.G. Small, G.M. Elchinger, A. Javan, A. Sanchez, F.J. Bachner, D.L. Smythe. Ac electron tunneling at infrared frequencies: Thin-film M-O-M diode structure with broadband characteristics. *Applied Physics Letters* 24: 275-279, 1974.

[5] S.Y. Wang, T. Izawa, T.K. Gustafson. Coupling characteristics of thin film metal-oxide-metal diodes at 10.6-μm. *Applied Physics Letters* 21(9):275-279, 1975.

[6] E. Wiesendanger and F. K. Kneubuhl. Thin-Film MOM-Diodes for Infrared detection. *Applied Physics* 13: 343-349, 1977.

[7] E.N. Grossman, J.E. Sauvegeau, D.G. McDonald. Lithographic spiral antennas at short wavelengths. *Applied Physics Letters* 59(25): 3225-3227, 1991.

[8] I. Wilke, W. Herrmann, F. K. Kneubuhl. Integrated nanostrip dipole antennas for coherent 30 THz infrared radiation. *Applied Physics* B58:87-95, 1994.

[9] N. Chong and H. Ahmed, Antenna-coupled polycrystalline silicon air-bridge thermal detector for mid-infrared radiation *Applied Physics Letters,* 71(12): 1607-1609, 1997.

[10] C. Fumeaux, W. Herrmann, H. Rothuizen, P. De Natale, F.K. Kneubuhl. Mixing of 30THz laser radiation with nanometer thin-film Ni-NiO-Ni diodes and integrated bow-tie antennas. *Applied Physics,* B62:135-140,1996.

[11] C. Fumeaux, G.D. Boreman, W. Herrmann, H. Rothuizen, P. De Natale, F.K. Kneubuhl. Polarization Response of Asymmetric Spiral Infrared Antennas. *Applied Optics,* 36(25): 6485-6490, 1997.

[12] F. J. González, C. S. Ashley, P. G. Clem and G. D. Boreman. Antenna-coupled microbolometer arrays with aerogel thermal isolation. *Infrared Physics & Technology*, 45 (1): 47-51, 2004.

[13] F.J. González, B. Ilic, J. Alda, G.D. Boreman. Antenna-coupled infrared detectors for imaging applications. *IEEE Journal of Selected Topics in Quantum Electronics,* 11 (1) :117-120, 2005.

[14] M. Abdel Rahman, B.Lail, and G. Boreman. Dual-band millimeter-wave/infrared focal-plane arrays. *Microwave and Optical Technology Letters*, 46 (1), 2005.

[15] M.Y. Frankel, S. Gupta, J.A. Valdmanis, G.A. Mourou. Terahertz, Attenuation and Dispersion Characteristics of Coplanar Transmission Lines. *IEEE Transactions on Microwave Theory and Techniques,* 39(6): 910-916, 1991.

[16] C. Fumeaux, M. Gritz, I. Codreanu, W. Schaich, F. J. González, G. Boreman, Measurement of the resonant lengths of infrared dipole antennas *Infrared Physics and Technology*, vol. 41, pp. 271-281, 2000

[17] T. Mandviwala, Modeling infrared antennas with complex conductivity, Master's Thesis, University of Central Florida, 2002.

[18] D. Grischkowsky, I. N. Duling III, J.C. Chen, C.C. Chi. Electromagnetic shock waves from transmission lines. *Physics Rev. Letters* 59(15):1663-1666, 1987.

[19] D. B. Rutledge, D. P. Neikirk, D. P. Kasilingham, Infrared and Millimeter waves, K. J. Button Ed. New York: Academic vol. 10, pt. 2, 1983.

[20] D.R. Dykaar, et al. High-frequency characterization of thin-film Y-Ba-Cu oxide superconducting transmission lines *Applied Physics Letters,* 52(17):1444-1446, 1988.

[21] G. Hasnain, A. Dienes, J.R. Winnery. Dispersion of picosecond pulses in coplanar transmission lines. *IEEE Transactions on Microwave Theory and Techniques,* 34:738-741,1989.

[22] J.H. Son, H.H. Wang, J.F. Whitaker, G.A. Mourou. Picosecond Pulse Propagation on Coplanar Striplines Fabricated on Lossy Semiconductor Substrates: Modeling and Experiments. *IEEE Transactions on Microwave Theory and Techniques,* 41(9): 1574-1580,1993.

[23] H.J. Cheng, J.F. Whitaker, T.M. Weller, L.P.B. Katehi. Terahertz-Bandwidth Characteristics of Coplanar Transmission Lines on Low Permittivity Substrates. *IEEE Transactions on Microwave Theory and Techniques,* 42(12): 2399-2406,1994.

[24] U.D. Keil, D. R. Dykaar, A. F. J. Levi, R. F. Kopf, L. N. Pfeiffer, S. B. Darack, K. W. West, High-Speed coplanar transmission lines, IEEE Journal of Quantum Electronics, vol 28, no. 10, 1992.

[25] R.L. Veghte, C.A. Balanis. Dispersion of Transient Signals in Microstrip Transmission Lines. *IEEE Transactions on Microwave Theory and Techniques,* 34(12):1427-1436,1986.

[26] K.C. Gupta, R. Garg, I.J. Bahl. *Microstrip Lines and Slotlines.* Artech House. Inc. 1979.

[27] O.P Jain *et al.* Coupled Mode Model of Dispersion in Microstrip. *Electron. Letters* 7:405-4071971.

[28] M.V. Schneider. Microstrip Dispersion. *IEEE Proceedings,* 60: 144-146,1972.

[29] W.J. Getsinger. Microstrip Dispersion Model. *IEEE Transactions on Microwave Theory and Techniques,* 21:34-39, 1973.

[30] H.J. Carlin. A Simplified circuit model for microstrip. *IEEE Transactions on Microwave Theory and Techniques,* 21:589-591, 1973.

[31] G. Kopma, R. Mehran. Planar waveguide model for calculating microstrip components. *Electron Letters,* 11: 459-460, 1975.

[32] T.C. Edwards, R.R. Owens. 2-18 GHz dispersion measurements on 10-100 ohm microstrip lines on sapphire. *IEEE Transactions on Microwave Theory and Techniques,* 24:506-513, 1976.

[33] R. Mittra, T. Itoh. A New Technique for the Analysis of the Dispersion Characteristics of Microstrip Lines. *IEEE Transactions on Microwave Theory and Techniques,*19(1): 47-56,1971.

[34] E.J. Denlinger. A Frequency Dependent Solution for Microstrip Transmission Lines. *IEEE Transactions on Microwave Theory and Techniques,* 19:30-39, 1971.

[35] T. Itoh, R. Mittra. Spectral-Domain approach for Calculating dispersion Characteristics of Microstrip Lines. *IEEE Transactions on Microwave Theory and Techniques,* 21(7): 496-499, 1973.

[36] D. Homentocovschi. An Analytical Approach to the Analysis of Dispersion Characteristics of Microstrip Lines. *IEEE Transactions on Microwave Theory and Techniques,* 39(4):740-743, 1991.

[37] E. Yamashita, A. Atsuki, T. Ueda. An Approximate Dispersion Formula of Microstrip Lines for computer-aided design of microwave integrated circuits. *IEEE Transaction on Microwave Theory and Techniques,* 27:1036-1038, 1979.

[38] H. Roskos, M.C. Nuss, K.W. Goossen, D.W. Kisker. Propagation of picosecond electrical pulses on a silicon-based microstrip line with buried cobalt silicide ground plane. *Applied Physics Letters,* 58(23):2604-2606, 1991.

[39] H.-M. Heiliger, M. Nagel, H.G. Roskos, H. Kurz. Low-dispersion thin-film microstrip lines with cyclotene (benzocyclobutene) as dielectric medium. *Applied Physics Letters,* 70(17):2233-2235 1997.

[40] L.T. Romankiw. A path: from electroplating through lithographic masks in electronics to LIGA in MEMS. *Electrochimica Acta,* 42(20-22):2985-3005, 1996.

[41] L.T. Romankiw, S. Krongelb, E.E. Castellani, A.T. Pfeiffer, B. Stoeber, J.D. Olsen, *IEEE Mag.,* 10, 828 (1974).

[42] M.C. Blakeslee, R.E. Acosta, S. Krongelb, L.T. Romankiw, B.J. Steober, *Journal of Electrochemical Society,* 125, 152 (1978).

[43] E. Spiller, R. Fader, J. Topalian, E.E. Castellani, L.T. Romankiw, M. Heritage, *Solid State Technology*, 62 (1976).

[44] LIGA News, Editor Wolfgang Ehrfeld. First issue January (1995).

[45] H. Guckel, T.R. Christenson, K.J. Skrobis, D.D. Denton, B. Choi, F.G. Lovell, J.W. Lee, S.S. Bajkar, T.W. Chapman, *1990 IEEE Solid State Sensor and Actuator Wisconsin Workshop,* Hilton Head, South Carolina, June (1990).

[46] D.L. Goldfarb, J.J de Pablo, P.F. Nealey, J.P. Simons, W.M. Moreau, M. Angelopoulos. Aqueous-based photoresist drying using supercritical carbon dioxide to prevent pattern collapse. *Journal of Vacuum Science & Technology,* 18(6):3313-3317 2000.

[47] Y. Xia and G.M. Whitesides. *Annu. Rev. Mater. Sci.* 28, pp. 153–184 (1998)

[48] S.Y. Chou, P.R. Krauss and P.J. Renstrom. *Appl. Phys. Lett.* 76, 3114 (1995).

[49] K. Kuwabara, Masahiko Ogino, Shigehisa Motowaki, Akihiro Miyauchi. Fluorescence measurements of nanopillars fabricated by high-aspect-ratio nanoprint technology. *Microelectronic Engineering*, 752-756, 2004.

[50] A. Miyauchi, K. Kuwabara, M. Hasegawa, *1st International Conference on Nanoimprint and Nanoprint Technology*, P-16, 2002

[51] Miyauchi, M. Ogino, S. Motowaki, K. Kuwabara, T. Sakazume, *International Symposium on Fusion of Nano and Bio Technologies,* P12, 2003

[52] C.M. Cheng, R.H. Chen, Key issues in fabricating microstructures with high aspect ratios by using deep X-ray lithography. *Microelectronic Engineering*, 71(3/4):335-343, 2004.

[53] Finkbeiner, F.M., Adams, C.; Apodaca, E.; Chervenak, J.A.; Fischer, J.; Doan, N.; Li, M.J.; Stahle, C.K.; Brekosky, R.P.; Bandler, S.R.; Figueroa-Feliciano, E.; Lindeman, M.A.; Kelley, R.L.; Saab, T., Talley, D.J.Development of ultra-low

impedance Through-wafer Micro-vias. *Nuclear Instruments & Methods in Physics Research (A)*, 520 (1-3):463 - 466, 2004.

[54] S. Vitale, H. Chae, H. Sawin. Etch Chemistry of BCB Low-K Dielectric Films in F2 + O2 and Cl2 + O2 High Density Plasmas, *Journal of Vacuum Science and Technology, A*, vol. 18, p. 2770, 2000.

[55] Michelle. J. Berry, P. Garrou, Boyd Rogers, Iwona Turlik. Soft Mask for Via Patterning in BCB Dielectric, International. *Journal of Microcircuits & Electronic Packaging*, Vol. 17, p. 210, 1994

[56] T. Mandviwala, B. Lail, G. Boreman. Infrared Frequency Coplanar Striplines: Design, Fabrication and measurements, *Microwave and Optical Technology Letters* Vol. 47(1): 7-20, 2005.

[57] T. Mandviwala, B. Lail, G. Boreman. Erratum: Infrared Frequency Coplanar Striplines: Design, Fabrication and measurements, *Microwave and Optical Technology Letters* Vol. 47(6): 609-610, 2005.

[58] J. Alda, C. Fumeaux, I. Codreanu, J. Schaefer, G. Boreman. A deconvolution method for two-dimensional spatial-response mapping of lithographic infrared antennas. *Applied Optics*, vol. 38, pp. 3993-4000, 1999.

[59] I. J. Bahl and D. K. Trivedi. A Designer's Guide to Microstrip line, Microwaves, May:174-182, 1977.